University of California, Merced

# Investigating Tribochemical Reactions Using Reactive Molecular Dynamics Simulations

A dissertation submitted in partial satisfaction of the requirements for the degree Doctor of Philosophy

In

Mechanical Engineering

By

Arash Khajeh

Committee in charge:
Professor Ashlie Martini, Advisor
Professor Min Hwan Lee
Professor Venkattraman Ayyaswamy
Professor Hrant Hratchian

2021

The Thesis of Arash Khajeh is approved, and it is acceptable in quality and form for publication on microfilm and electronically:

_____

Professor Ashlie Martini

_____

Professor Venkattraman Ayyaswamy

_____

Professor Hrant Hratchian

_____

Professor Min Hwan Lee Chair

University of California, Merced
2021

*To my wife, Dorna*
*and my son, Ryan*

## TABLE OF CONTENTS

## LIST OF FIGURES

## LIST OF TABLES

## Acknowledgements

We Thank Dr. Seong H. Kim, Dr. Xin He (Penn State University), and Dr. Jejoon Yeon (University of Delaware) for directions and supervisions in *Shear-Induced Polymerization of Alpha-Pinene Molecules at Sliding Interfaces* project (Chapter 2). This work was carried out with the support from the National Science Foundation (Grant No. CMMI-1435766, 1727571, 1727356).

We thank Dr. Stephen Berkebile for discussion and helpful feedback on Thermally Activated Film Formation from TCP on Iron Oxide Substrate project (chapter 3). We also acknowledge support from the Army Research Laboratory under Cooperative Agreement Number W911NF-16-2-0121 for this project.

We Thank Dr. Seong H. Kim, and Dr. Zhe Chen (Penn State University) for directions and supervisions in Chemical and Physical Contributions to the Friction at the Sliding Interfaces project (Chapter 2). This work was supported by the National Science Foundation (Grant No. CMMI-1727356 and 1727571).

Also, part of this work was funded by the Austrian COMET-Program (Project K2 InTribology1, no. 872176) and carried out in collaboration with the Austrian Excellence Center for Tribology (AC2T research GmbH).

The text of this dissertation includes reprints of the following previously published material:

Khajeh, A., He, X., Yeon, J., Kim, S. H., Martini, A. (2018). Mechanochemical Association Reaction of Interfacial Molecules Driven by Shear. Langmuir, 34(21), 5971-5977. DOI: 10.1021/acs.langmuir.8b00315

Khajeh, A., Hu, X., Mohammadtabar, K., Shin, Y. K., van Duin, A. C., Berkebile, S., & Martini, A. (2019). Statistical analysis of tri-cresyl phosphate conversion on an iron oxide surface using reactive molecular dynamics simulations. The Journal of Physical Chemistry C, 123(20), 12886-12893. DOI: 10.1021/acs.jpcc.9b02394

Khajeh, A., Krim, J., & Martini, A. (2019). Synergistic effect of nanodiamonds on the adsorption of tricresyl phosphate on iron oxide surfaces. Applied Physics Letters, 114(17), 171602. DOI: 10.1063/1.5093425

Chen, Z., Khajeh, A., Martini, A., & Kim, S. H. (2019). Chemical and physical origins of friction on surfaces with atomic steps. Science advances, 5(8), eaaw0513. DOI: 10.1126/sciadv.aaw0513

Chen, Z., Khajeh, A., Martini, A., & Kim, S. H. (2020). Identifying physical and chemical contributions to friction: a comparative study of chemically inert and active graphene step edges. ACS Applied Materials & Interfaces, 12(26), 30007-30015. https://doi.org/10.1021/acsami.0c08121

Khajeh, A., Chen, Z., Kim, S. H., & Martini, A. (2019). Effect of Ambient Chemistry on Friction at the Basal Plane of Graphite. ACS Applied Materials & Interfaces, 11(43), 40800-40807. DOI:10.1021/acsami.9b13261

The co-author listed in this publication directed and supervised the research which

# Curriculum Vita

## Arash Khajeh

**Current Position**

Graduate Research Assistant and Ph.D. Candidate in Mechanical Engineering (Aug. 2016 – Now)
*University of California, Merced- GPA 4.0/4.0*
Dissertation title: Investigating Tribochemical Reactions Using Reactive Molecular Dynamics Simulations

**Awarded Degrees**

M.Sc. in Materials Science and Engineering (Sep. 2008)
*Shiraz University- GPA 17.3/20.0 (3.6/4.0)*
Thesis title: Numerical Analysis of Backward Extrusion, Ironing, and Radial Forging Processes using Finite Element Method to Investigate the Possibility of Manufacturing Long Seamless Tubes with Varying Cross-section

B.Sc. in Industrial Metallurgy (Sep. 2005)
*Shiraz University, GPA 15.4/20.0 (3.1/4.0)*
Final Project: Investigation on Mechanical Properties of Dual Phase Steels

**Research Interests**

- Computational materials science (molecular dynamics, finite element simulations, machine learning and deep learning)
- Tribology, Lubrication, and Surface Science
- Li ion batteries
- Powder Metallurgy
- Metal Forming

**Publications**

***Journal Papers***

20- Khajeh, A., Rahman, Md., Panwar, P., Patel, M., Misra, M., Menezes, P. L., Martini, A. Thermal decomposition of phosphonium salicylate and phosphonium benzoate ionic liquids (Submitted to Journal of Molecular Liquids).

19- Liu, T., Panwar, P., Khajeh, A., Rahman, M. H., Menezes, P. L., and Martini, A. Review of Molecular Dynamics Simulations of Phosphonium Ionic Liquid Lubricants (Submitted to Tribology Letters).

18- Rahman, Md. H, Khajeh, A., Panwar, P., Patel, M., Misra, Martini, A., M., Menezes, P. L., Recent Progress on Phosphonium-based Room Temperature Ionic Liquid Lubricants: Synthesis, Properties, Performance, and Applications. (Submitted to Tribology International).

17- Chen, Z., Khajeh, A., Martini, A., & Kim, S. H. (2020). Origin of High Friction at Graphene Step Edges on Graphite. ACS Applied Materials & Interfaces. DOI:10.1021/acsami.0c18098

16- Khajeh, A., Bhuiyan, F. H., Mogonye, J. E., Pesce-Rodriguez, R. A., Berkebile, S., & Martini, A. (2021). Thermal Decomposition of Tricresyl Phosphate on Ferrous Surfaces. The Journal of Physical Chemistry C. DOI: 10.1021/acs.jpcc.0c10789

15- Chen, Z., Khajeh, A., Kim, S. H., Martini, A., Identifying physical and chemical contributions to friction: A comparative study of chemically inert and active graphene step edges, *ACS Applied Materials & Interfaces*, DOI:10.1021/acsami.0c08121

14- Ewen, J. P., Latorre, C. A., Gattinoni, C., Khajeh, A., Moore, J. D., Remias, J., Martini, A., Dini, D., Substituent and Surface Effects on the Thermal Decomposition of Phosphate Esters, *The Journal of Physical Chemistry C*, *124*(18), 9852-9865. DOI:10.1021/acs.jpcc.9b11787

13- Khajeh, A., Chen, Z., Kim, S. H., & Martini, A. (2019). Effect of Ambient Chemistry on Friction at the Basal Plane of Graphite. *ACS Applied Materials & Interfaces*, 11(43), 40800-40807. DOI:10.1021/acsami.9b13261

12- Chen, Z., Vazirisereshk, M. R., Khajeh, A., Martini, A., & Kim, S. H. (2019). Effect of atomic corrugation on adhesion and friction: A model study with graphene step edges. *The Journal of Physical Chemistry Letters*, 10(21), 6455-6461. DOI: 10.1021/acs.jpclett.9b02501

11- Chen, Z., Khajeh, A., Martini, A., & Kim, S. H. (2019). Chemical and physical origins of friction on surfaces with atomic steps. *Science advances*, 5(8), eaaw0513. DOI: 10.1126/sciadv.aaw0513

10- Khajeh, A., Krim, J., & Martini, A. (2019). Synergistic effect of nanodiamonds on the adsorption of tricresyl phosphate on iron oxide surfaces. *Applied Physics Letters*, 114(17), 171602. DOI: 10.1063/1.5093425

9- Khajeh, A., Hu, X., Mohammadtabar, K., Shin, Y. K., van Duin, A. C., Berkebile, S., & Martini, A. (2019). Statistical analysis of tri-cresyl phosphate conversion on an iron oxide surface using reactive molecular dynamics simulations. *The Journal of Physical Chemistry C*, 123(20), 12886-12893. DOI: 10.1021/acs.jpcc.9b02394

8- Jenei, I. Z., Dassenoy, F., Epicier, T., Khajeh, A., Martini, A., Uy, D., ... & Gangopadhyay, A. (2019). Mechanical response of gasoline soot nanoparticles under compression: An in situ TEM study. *Tribology International*, 131, 446-453. Doi: 10.1016/j.triboint.2018.11.001

7- Khajeh, A., He, X., Yeon, J., Kim, S. H., Martini, A. (2018). Mechanochemical Association Reaction of Interfacial Molecules Driven by Shear. *Langmuir*, 34(21), 5971-5977. DOI: 10.1021/acs.langmuir.8b00315

6- Jenei, I. Z., Dassenoy, F., Epicier, T., Khajeh, A., Martini, A., Uy, D., ... & Gangopadhyay, A. (2018). Mechanical Characterization of Diesel Soot Nanoparticles: In Situ Compression in a Transmission Electron Microscope and Simulations. *Nanotechnology*, 29(8). DOI: 10.1088/1361-6528/aaa2aa

5- Khajeh, A., & Jahromi, S. A. J. (2014). The Finite Element Analysis of the Surface Transformation Hardening Process Using the Power Control Strategy in Order to Reduce Edge Effect Problems. *Computational Materials Science*, 88, 151-155. DOI: 10.1016/j.matdes.2011.08.020

4- Mahmoudi, B., Khajeh, A., Torkamany, M. J., & Bazargan-Lari, R. (2012). The Effect of Pre Heat Treatment before Laser Surface Treatment on AISI410: Martensitic Stainless Steel. *Science of Advanced Materials*, 4(3-4), 518-521. DOI:10.1166/sam.2012.1312

3- Jahromi, S. J., Khajeh, A., & Mahmoudi, B. (2012). Effect of Different Pre-Heat Treatment Processes on the Hardness of AISI 410 Martensitic Stainless Steels Surface-Treated Using Pulsed Neodymium-Doped Yttrium Aluminum Garnet Laser. *Materials & Design*, 34, 857-862. DOI: 10.1016/j.matdes.2011.08.020

2- Shirdel, A., Khajeh, A., & Moshksar, M. M. (2010). Experimental and Finite Element Investigation of Semi-Constrained Groove Pressing Process. *Materials & Design*, 31(2), 946-950. DOI: 10.1016/j.matdes.2009.07.035

1- Danesh, H. D., Mashreghi, A., Haghighi, S. E., & Khajeh, A. (2009). Investigation of Cold Pressure Welding of Aluminum Powder to Internal Surface of Aluminum Tube. *Materials & Design*, 30(3), 723-726. DOI: 10.1016/j.matdes.2008.05.014

***Publications in Farsi***

2- Khajeh, A., Jenabali Jahromi, S., A., Danesh Manesh, H., The Finite Element Analysis of the Surface Transformation Hardening Process Using the Velocity Control Strategy in Order to Reduce Edge Effect Problems, *Iranian Journal of Advanced Process in Materials Engineering*, Vol. 3, pp. 12-23, 2015.

1- Khajeh, A., Jenabali Jahromi, S., A., Danesh Manesh, H., The Finite Element Analysis of Standard Hardenability Test (Jominy Test) on S355 Steel using Machnienko Kinetic Model, *Journal of New Materials*, Vol. 5, pp. 57-68, 2015.

**Presentations**

- Tribology Frontiers Conference, Chicago, October 20-23, 2019
  Effect of Ambient Chemistry on Friction at the Basal Plane of Graphite (Oral Presentation)

- NorCal STLE, Oakland, CA, September 25th 2019
  Investigating Tribochemical Reactions Using Reactive Molecular Dynamics Simulations (Oral Presentation)

- Tribology Frontiers Conference, Chicago, October 28-31, 2018
  Friction at a Single Layer Graphene Edge on Graphite: Part 2 - Simulation Study with Molecular Dynamics (Oral Presentation)

- Tribology (GRS) Gordon Research Seminar and Tribology (GRC) Gordon Research Conference, Lewiston, ME, 23-29, 2018
  Mechanochemical Association Reaction of Interfacial Molecules Driven by Shear (Poster)

- Society of Tribologists and Lubrication Engineers (STLE) 73rd Annual Meeting and Exhibition, Minneapolis, May 20-24, 2018 (Oral Presentation)
  Effect of Surface Reactivity on Tribopolymerization of Alpha-Pinene Molecules, Society of

- Society of Tribologists and Lubrication Engineers (STLE) 72nd Annual Meeting and Exhibition, Atlanta, May 21-25, 2017
  Analysis of Mechanical Behavior in Soot Nanoparticles Under Consecutive Compression Tests Using Molecular Dynamics Simulation (Poster)

- ASME International Mechanical Engineering Congress and Exposition, Lake Buena Vista, Florida, November 13-19, 2009
  Investigation of Corner Cavity Formation During Backward Cup Extrusion Process Using Finite Element Method DOI: 10.1115/IMECE2009-12321

- 11th Annual Symposium of Steel in Iran, Shahid Chamran University, Ahvaz, 3-4 March 2009 (Oral Presentation)
  Finite Element Analysis of Radial Forging Process to Investigate the Possibility of Producing Long Steel Tubes with Various Cross- Sections

**Research Experience**

- Developing deep neural network-based predictive models to estimate ionic transport properties in solid state polymer electrolytes (Industrial project performed in Accelerated Materials Design and Discovery Team at Toyota Research Institute. (Jun. 2021 – Sep. 2021)

- Investigating the effect of cation-anion pairing on thermal decomposition of room temperature ionic liquids (RTILs) using reactive molecular dynamics simulation - In collaboration with Dr. Pradeep Menezes at University of Nevada, Reno. (Sep. 2020 – Sep. 2021)

- Predicting the effect of bio-polymer structures on viscosity and shear thinning behavior using molecular dynamics simulations (Industrial project performed at Zymergen Inc. -Summer 2020)

- Thermal and tribofilm formation from phosphorous-based lubricant additives investigated using reactive molecular dynamics simulations
  Research performed under Dr. Ashlie Martini, and in collaboration with the US Army Research Laboratory (ARL). (Jan. 2018 – Sep. 2020)

- Investigation of chemical and physical origin of friction on graphitic surfaces using reactive molecular dynamics simulations
  Research performed under Dr. Ashlie Martini and in collaboration with Dr. Seong. H. Kim (Dept. of Chemical Engineering and Materials Research) at Penn State University. (Feb. 2018 - Now)

- Mechanically-induced polymerization reactions of hydrocarbons explored using reactive molecular dynamics simulations
  Research performed under Dr. Ashlie Martini, and in collaboration with Dr. Seong. H. Kim (Chemical Engineering and Materials Research) at Penn State University. (Jun. 2017 – Feb. 2018)

- Investigation of mechanical behavior of diesel and gasoline soot nanoparticles using molecular dynamics simulations
  Research performed under Dr. Ashlie Martini (Mechanical Engineering) and in collaboration with Dr. Fabrice Dassenoy (Materials Science) at Ecole Centrale de Lyon and the Ford Co. (Nov. 2016– Jun. 2017)

- Experimental and finite element study of heat transfer and phase transformation in steels during laser surface hardening process
  Research performed under Dr. Seyed Ahmad Jenabali Jahromi (Materials Engineering, Shiraz University) (Oct. 2011– Feb. 2015)

- Finite element analysis of severe plastic deformation in semi-constrained groove pressing
  Research performed under Dr. Mohammad Moshen Moshksar (Materials Engineering, Shiraz University) (May. 2009– Oct. 2010)

- Exploring the origins of corner cavity defect during backward cup extrusion process by using finite element simulations
  Research performed under Dr. Mohammad Moshen Moshksar (Materials Engineering, Shiraz University) (Sep. 2008– Sep. 2009)

- Experimental study on the effect of surface preparation on mechanical properties of the solid-State weld of commercially pure aluminum powder

Research performed under Dr. Habib Danesh Manesh (Materials Engineering, Shiraz University) (Sep. 2005– Jan. 2006)

**Work Experience**

Accelerated Materials Design and Discovery Researcher (via HireArt) – (Sep. 2021-Now)
*Toyota Research Institute., Los Altos, CA*

- Accelerating molecular dynamics simulations applicable in solid polymer electrolytes.

Intern (Summer 2020)
*Toyota Research Institute., Los Altos, CA*

- Developed predictive models based on dense and recurrent neural networks and estimated Li ion conductivity and diffusivity in solid polymer electrolyte-based lithium metal batteries utilizing more than 6000 trajectories obtained from molecular dynamics simulations.
- Provided insight into the diffusivity of Li ions in polymeric electrolytes through visualizing trajectories of ions obtained from molecular dynamics simulations.
- Formulated and implemented innovative ideas to create new features that correlate with Li conductivity and diffusivity.
- Delivered feedback to AMDD team about MD simulations performed by collaborators.

Computational Chemistry Intern (Summer 2020)
*Zymergen Inc., San Francisco, CA*

- Responsible for designing, performing, and validating MD simulations to study the structure-properties relationships of biopolymers.
- Predicted thermo-mechanical properties, e.g., viscosity, shear-thinning, glass transition temperature, tensile strength, tensile modulus, and relaxation time using molecular dynamics simulations of biopolymers with various structures.
- Communicated the results with the product team.
- Successfully identified the best computational resources leading to more than 3× increase in processing speed and about 20% decrease in computational costs.

Research Assistant (Fall 2016 – Now)
*UC Merced, School of Engineering*
Designed and developed molecular dynamics simulations and statistical techniques in the areas of mechanics of nanoparticles, surface chemical reactions, and friction, published papers, presented the results in conferences, and mentored students

Teaching Assistant for Strength of Materials (Aug. 2016 – May 2017)
*UC Merced, School of Engineering*
Attended lectures, instructed in the lab sessions, held office hours, and graded homework

QC Materials Engineer (Apr. 2015 – Apr. 2016)
*Aban Air Cooler Co. (Designer and Manufacturer of Heat Exchangers), Engineering and Design Department*

- Developed manufacturing and inspection procedures including Weld Procedure Specification (WPS), Procedure Qualification Records (PQR), Non-Destructive Tests (NDT), hydrostatic tests, and painting procedures for the fabrication of air-cooled and shell & tube heat exchangers for oil, gas and petrochemical industries.
- Evaluated and proposed the applicability of materials for different design temperatures and corrosive environments based on the latest standards.
- Proposed recommendations to resolve problems in welding, cladding, rolling, and painting units.

Graduate Research Assistant (Sep. 2010 - Feb. 2015)
*Shiraz University, Department of Materials Science and Engineering*
Performed finite element simulations using ABAQUS finite element software and explored heat transfer and phase transformation during laser surface hardening processes of steels

Part Time Lecturer in Materials Science (Fall 2013)
*Shiraz University, Department of Mechanical Engineering*
Instructed the course, designed the assignments, designed the exams, and graded the materials

Part Time Lecturer in Engineering Drawing (Sep. 2011 - Feb. 2013)
*Islamic Azad University (Fars Science and Research Branch)*
Instructed the course (more than 25 groups of about 20 students from different branches of engineering), designed the assignments, prepared exams, and graded the materials

# Abstract

Tribochemical reactions are reactions that happen at sliding interfaces due to applied pressure, shear, and heat. These reactions are responsible for the formation of tribofilms on surfaces in relative motion and affect several important tribological properties, including coefficient of friction and wear rate. In fact, the composition and structure of tribofilms can be a determining factor in the energy consumption and life of engineering components. Therefore, understanding the mechanisms by which the tribofilms form and how they interact with sliding surfaces is of great importance in many industries. This dissertation aims to explore the tribochemical reactions that are the root cause of tribofilm formation and their contribution to friction using reactive molecular dynamics simulations. To achieve this goal, we first investigated shear-induced polymerization reactions during vapor phase lubrication of α-pinene between sliding hydroxylated and dehydroxylated silica surfaces. The results suggested that the critical activation step is the oxidative chemisorption of the α-pinene molecules at reactive surface sites, which transfers oxygen atoms from the surface to the adsorbate molecule. Such activation takes place more readily on the dehydroxylated surface and, during this step, the most strained part of the α-pinene molecules undergoes partial distortion from its equilibrium geometry, which appears to be related to the critical activation volume for mechanical activation. Next, we studied the effect of temperature on the thermal film formation of tri-cresyl phosphate (TCP) on amorphous iron oxide. The statistical analysis of chemical reactions between a single TCP molecule and an amorphous iron oxide surface captured multiple possible reaction pathways. The frequency of TCP– surface reactions for each atom type and each unique reaction site on the TCP were analyzed at temperatures ranging from 300 to 700 K. The composition of the thermal film chemisorbed to the surface was mainly carbon, oxygen, and phosphorous, in agreement to the previously reported experiments performed in oxygen-deficient environments. Analysis of chemical bonding between TCP and iron oxide surfaces in the presence of nanodiamonds (NDs) showed a tribofilm comprised of NDs and TCP where the TCP was both directly and indirectly bonded to the surface. Notably, the amount of phosphorous in the film, which is important for surface protection, increased due to TCP molecules indirectly bonded to the surface via NDs, which suggested that indirect bonding is one mechanism by which NDs facilitate film growth. Lastly, we investigated the contributions of chemical and physical interactions to friction at sliding interfaces. To achieve this, chemically and topographically well-defined interfaces between silica and graphite with a single graphene step edge and basal plane were studied in various chemical environments. A range of different parameters, including applied pressure, sliding direction, chemical reactivity of surface, and environment, were shown to be important in the observed friction. Further, the findings suggest different contributions and sometimes opposite effects of chemical and physical contributors to the friction. Overall, in this series of studies, we used and developed new simulation and statistical analysis approaches for studying tribochemical reactions. The findings show that reactive molecular dynamics simulation is a robust approach that can provide insight into the conditions and properties of interfaces and so can be used as a valuable guide to improve tribological properties.

# Chapter 1 : Introduction

## 1.1. Tribology and Lubrication

Tribology is the science and study of friction, lubrication, and related phenomena that occur between surfaces in relative motion. Friction itself is a cause of energy waste. It has been reported that about one-third of fuel energy is consumed to overcome friction in passenger car components like engines, transmissions, tires, and brakes. [1] Sliding and relative motion also result in wear of the contacting materials. Wear is responsible for catastrophic failure and mechanical breakdown of engineering components like bearings, gears, cylinders etc. To reduce friction and wear, lubrication with engine oils is usually employed during operation. Proper lubrication is important as it can reduce the premature failures by 60%.[2] This also decreases the stresses applied on components and allows the use of smaller and less costly materials in manufacturing. Effective lubrication can enhance product quality and lifetime by decreasing surface defects such as pits and cracks that are caused by metal-to-metal contact.

Lubricants produce a gap between the sliding surfaces to avoid solid-solid material contacts and thus reduce friction. However, the formation of a full fluid film and the elimination of direct contact are not always guaranteed, especially under high pressure or low speeds. This situation is called boundary lubrication, which is the lubrication of surfaces by fluid films so thin that the friction coefficient is affected by both the type of lubricant and the nature of the surfaces and is largely independent of viscosity of lubricant fluid.[3] An effective lubricant must be able to control friction and wear even during boundary lubrication. Physical and chemical interactions between the lubricant and the sliding surfaces play critical roles during boundary lubrication regime. Also, characteristics of sliding solid surfaces such as surface roughness, shear strength, hardness, chemical composition, and surface reactivity significantly affect the frictional behavior in boundary lubrication.

## 1.2. Tribofilm Formation and the Role of Lubricant Additives

As previously mentioned, lubricants decrease friction during the sliding process by separating the sliding interfaces. However, reducing friction is not the only function of lubricants. Lubricants also act as heat transfer agents, remove wear debris, inhibit corrosion, and reduce noise during operation. To serve these purposes, lubricants are usually formulated with additive packages to improve the lubrication performance. These additives include friction modifiers, dispersants, detergents, corrosion inhibitors, viscosity index modifiers, extreme pressure additives, and antiwear additives. Among these, antiwear additives, friction modifiers and extreme pressure additives are the most important as they can significantly protect components through reducing the friction and wear under boundary lubrication.[4-6] Zinc dithiophosphates (ZDDP) and tricresyl phosphate (TCP) are the most widely used anti-wear/extreme-pressure additives in engine oils.[7] These substances can adsorb or directly react with metal surfaces and form a protective film on the surface of substrates. During boundary lubrication, chemical bonds deform, break and form again between the additive species and the sliding surfaces. At the same time, rubbing the surfaces causes breaking of the bonds on the sliding surfaces and exposes newly formed fresh surfaces with significantly higher energies compared to native surfaces. The exposed high-energy chemical groups can easily react with lubricant additives to produce a

boundary chemical film known as tribofilm. Although the increase in the reactivity accelerates the reactions between the surface and lubricant molecules, it does not always reduce the friction and wear. In fact, it has been found that depends on what type of molecules react with the surface to form tribofilm there is an optimum surface reactivity to achieve the best possible friction and wear properties.[8] However, usually tribofilms form from anti-wear additives and extreme pressure additives and they act as protective films that enable effective lubrication in boundary lubricated systems.

Researchers have been trying to understand the mechanisms involved in tribofilm formation for more than 50 years. [9] Many hypotheses have been developed around tribochemical reactions. Flash temperature rise, pressure, and surface chemistry have been suggested to be the most significant contributors to the tribofilm formation. During the sliding process, the local heat generation due to friction can cause temperature increase known as flash temperature. Some studies have suggested that the increase in the flash temperature promotes the formation of tribofilms like ZDDP.[10] However, the formation of these protective layers have been also reported at very low sliding speeds where the increase in the flash temperature is negligible.[11] Some theories suggested that the existence of high pressure on surface asperities drives these reactions. Although simulations have shown that crosslinking of phosphate networks observed in the experiments is possible at extreme high applied pressures[12], the occurrence of this necessary pressure is unlikely at the interfaces based on the yield strength for the most engineering materials.[13] Finally, it is now widely accepted that the tribofilms can form due to the shear stress present at the interfaces during rubbing.[14-17] For example, the thickness of ZDDP tribofilms is found to be controlled by applied shear stress and not normal stress. [14]

If a tribofilm is formed by shear stress driving chemical reactions between the antiwear additives and sliding interfaces, this process is called a tribochemical reaction. A tribochemical reaction is a mechanochemical reaction where the mechanical force is shear.[18] According to IUPAC, a mechanochemical reaction is a chemical reaction that can be induced by the direct absorption of mechanical energy [19]. In other words, the applied forces control the rate at which atoms and molecules can overcome the energy barriers. In the absence of shear, the probability of physical and chemical phenomena at atomic-scale like bond breaking and diffusion can be described by an Arrhenius-form equation:

$$Probability = Ae^{\frac{-E_0}{K_B T}} \qquad (1)$$

In this equation $A$ is a pre-exponential factor, $E_o$ is the activation energy for the process, $k_B$ the Boltzmann constant, and $T$ is the absolute temperature. According to the Bell model[20] developed to describe stress-assisted thermal activation reactions, applied atomic force ($f$) can reduce the effective activation energy barrier of the reaction based on the following equation:

$$Probability = Ae^{\frac{-(E_0 - f\Delta x)}{K_B T}} \qquad (2)$$

Here, $\Delta x$ is activation distance equal to the length of bond stretch or particle displacement. Therefore, $f\Delta x$ is the mechanical energy provided to the atoms to overcome the activation energy barrier $E_0$. It should be noted that the applied force can theoretically increase the activation energy barrier for the reverse reaction along the opposite direction

of applied force.[14] The above equation can then be described in terms of the shear stress $\tau$ and an activation volume $\Delta v$ instead of force and activation distance:[21, 22]

$$Probability = Ae^{\frac{-(E_0-\tau\nabla v)}{K_B T}} \quad (3)$$

There have been several attempts to define the physical meaning of activation volume ($\Delta v$) at the atomic scale. $\Delta v$ is believed to have a close relationship with the deformation of reactants due to mechanical forces that induce reactions during sliding. [23-28]

Mechanochemical reactions have many applications in different areas of tribology including sliding friction[28-31], wear[23, 29, 30, 32, 33] and rheology[34-36]. The concept of mechanochemistry helps us to describe the macroscale phenomena that contribute to the changes in friction coefficient and tribofilm formation, and provides us better insight to design surfaces and lubricants for different tribological purposes.[37, 38]

## 1.3. Experimental Methods for Characterization of Tribochemical Reactions

To explore tribofilms experimentally, usually, a combination of wear testing systems and surface characterization instruments are used. The length scale of study of tribofilms are ranging from atomic scale to the macro scale. For example, different variations of scanning probe microscopy (SPM) instruments been used as nanotribometers to measure friction[39], adhesion,[40] wear[41], and rheometery[42] at an ultra-small scale. At the same time conventional tribometers are employed to evaluate almost the same range of properties at the macro scale [43]. Today, atomic force microscopy (AFM) is the most standard tool for investigating the frictional behavior of materials at the nanoscale[24, 42, 44, 45]. Fourier-transform infrared spectroscopy (FTIR)[46], Raman[47], x-ray photoelectron spectroscopy (XPS)[48], auger electron spectroscopy (AES)[48, 49], and time of flight secondary ion mass spectrometry (TOF SIMS)[50] are used for analytical measurements of surface films. Most of these techniques are relying on surface characterization of tribo-products as a post-process step and cannot be used as an in-situ tool to investigate the dynamic behavior of the system during the sliding process. The main challenge in this area is that the formation of tribofilms is usually hidden between sliding opaque surfaces, and thus tracking its evolution is difficult.

There have been numerous experimental studies exploring the chemical reactions involved in tribofilm formation. Specifically, many researchers investigated the role of reactivity of surface and reactants on the kinetics of reactions. For example, Auger cylindrical-mirror analysis was employed to assess the tribo-products formed on steel surface due to interactions with hydrocarbons and organic hydrochlorides.[51] These experiments showed that the chemical reactions involved in tribofilm formation occurred on newly exposed metal surfaces was the result of enhanced reactivity of the freshly exposed metal surfaces. The finding suggested that under high-vacuum condition clean iron surface reacted easier than iron oxide with any hydrocarbon molecules. Also, the hydrocarbon species with higher reactivity were found in greater concentration on the surface after the sliding, a phenomenon attributed to polymer-forming tendencies of reactive molecules. In another study, the chemical reaction kinetics were analyzed to calculate the reaction temperatures required to produce the observed amount of products from the wear processes during boundary lubrication of steel 52100 with paraffinic mineral

oils.[52] It was reported that the reaction temperatures on freshly exposed steel surface were very similar to those of an oxide covered surface. It was concluded that the effect of freshly exposed surfaces on the reaction rates is negligible under atmospheric conditions, and as a result, thermal effects are the determining factor for controlling the boundary chemical reactions on steel surface. Finally, Transmission Electron Microscopy (TEM) and extended X-ray absorption fine structure (EXAFS) analysis revealed that a ZDDP tribofilm has an amorphous structure[48, 53], which is mainly composed of oxygen, phosphorus, sulfur, zinc, and sometimes iron[54]. It has been also reported that the iron oxide layer formed on ferrous surfaces disappears during tribo-chemical reactions with ZDDP.[55-57] All of above-mentioned studies and many more are suggesting the important role of tribochemistry and surface reactivity on the type and the amount of formed triboproducts on engineering surfaces. However, there are little atomic scale detailed information about how surface reactivity specific reactions leading to the formation of tribofilms.

For a long time, various types of tribometers and characterization tools have been used to drive tribochemical reactions and to evaluate the behavior of generated tribofilms films. cylinder-on-flat tribometer was used to grow ZDDP on an iron oxide surface. [58] In this study, dry friction tests in the UHV analytical tribometer were performed, and the results suggested the effect of friction solicitations on the reaction of zinc polyphosphate with iron oxide providing mixed zinc and iron phosphate glass. In another study a new gas-phase lubrication tribometer was devised to study reactions of borate ester additives on steel surfaces. [59] The XPS and AES performed inside and outside of the wear track showed a reduction in the friction coefficient down to 0.2 by the increase in the Trimethylborate gas pressure. This phenomenon was attributed to the formation of borate silica glass, which partially digested the abrasive iron oxide tribofilm. A mini-traction machine (MTM) in tribotests experiments was employed to investigate the effect of additive concentration and temperature on the wear of rolling/sliding contacts in boundary lubrication regime. [60] Comparing the white-light interferometry analysis results with a predictive numerical model [61] developed for the prediction of wear and friction coefficient during sliding showed good agreements in terms of tribofilm thickness and observed wear depth. X-ray absorption near edge structure (XANES) spectroscopy to was used to characterize thermally generated films from several ZDDP antiwear agents in basic and neutral forms.[62] The findings revealed the tribochemical nature of films formed in terms of the proportion of the presence of polyphosphates, sulfides, and unchanged ZDDP. Further the results suggested the importance of reactant structure, showing that the aryl ZDDP films provide a different polyphosphate structure compared to the alkyl ZDDP films.

Recently, AFM has been introduced as a powerful in-situ tool to study stress-driven tribochemical reactions with the sensitivity to atomic-scale interactions.[24, 28, 63, 64] In a recent study, a sliding AFM tip is used to study the bond cleavage between chemical groups attached on chemically modified graphene (CMG) sheets. [28] Also, the friction between the tip and graphene provides the opportunity to measure the bond strength between different chemical groups and surfaces as well as the kinetics of functional group removal. In another study, AFM was employed as an in-situ tool to study the surface nucleation, growth and thickness saturation of patchy tribofilms formed from ZDDP containing lubricants. [24] The results showed an exponential increase in the film growth rate with applied compressive stress and temperature, an observation consistent with a thermally activated, stress-assisted

reaction rate model (Equation 3). In another research, in-situ AFM was employed the to study the reaction kinetics of phosphorous based triboreactive films. [64] It was reported that different phosphorus-containing molecules follow different reaction kinetics orders. This phenomenon has been explained by the energy consumed by possible side and intermediate reactions leading to the formation of products other than antiwear phosphate glass at the sliding interfaces.

Although experimental tools provide valuable information about the surface structure, chemistry, friction, and wear, their applications are mostly limited to the characterization before and after the tribological tests. As a result, the experimental characterization tools, as they cannot provide us with detailed information about the dynamics of the sliding interface at the atomic-scale leading to the formation of tribofilms. This challenge partially has been addressed by using atomic-scale simulations. [18]

### 1.4. Atomistic Simulations for Tribology Purposes

Simulations can be used to complement experimental measurements to provide information about processes that occur between two sliding surfaces or during thermal film formation. Since many of these phenomena take place at the atomic scale, the most appropriate modeling techniques are those that describe the positions of atoms based on energies and forces. The most commonly used atomistic modeling methods are density functional theory (DFT)[65], molecular dynamics simulation (MD)[66], and kinetic Monte Carlo (KMC)[67]. DFT is the most popular and versatile quantum mechanical modeling method extensively used in physics, chemistry, and materials science. This method provides an approximate solution to the Schrodinger equation of a many-body system. According to this method, all information required to solve the Schrodinger equation is stored in electron density around the nuclei. Therefore, it can be used to solve a wide variety of problems and provide useful information, including the optimized geometry, bond distances, bond angles, etc.[68, 69] MD simulations solves Newton's equations of motions for the atoms in the systems. They approximate the quantum-mechanical effects using different empirical equations known as forcefields.[18] Finally, KMC[67, 70] uses reactions and transition rates among states to predict the phenomena like adsorption and the evolution of film. The input reactions and transition rates are obtained from experiments, DFT, MD simulations, and this method are not able to predict this information by itself. Among the methods mentioned, for several reasons that will be discussed, MD simulations are the most powerful tools that can provide a better understanding of the trobochemical reactions that happen at sliding interfaces. MD simulations shown to be able to link macroscale laws of friction and sliding derived from experiment to the atomic-scale phenomena including chemical reactions. [18]

Probably, the most essential step in study of tribochemical reactions is detection of bond breaking and bond formation events. The most accurate method to model the formation and breaking of covalent bonds is DFT calculations. However, due to the high computational cost of this method, the time length-scale of studied systems is so limited that the study of the full dynamic evolution of a system is not possible.[18] One more challenge for simulation-based approaches is that film growth may occur through many different reaction pathways with varying statistical likelihood, especially at high temperatures or on irregular, e.g. amorphous or disordered, surfaces. DFT can provide

detailed and highly accurate information about a given pathway, but the pathways must be known a priori and the computational cost of the method typically means that only a few possible pathways can be studied.[71-73]

As an alternative method, MD simulations consider the interactions between the atoms as a single particle as opposed to nucleus and electrons in the DFT method. Therefore, they provide computational efficiency in the cost of some level of loss of accuracy. [18] In MD, multiple reaction pathways can be identified during the simulation as atoms interact and move, but traditional MD is limited to relatively small size (nanometer) and time (nanosecond) scales, which means that only one or a few pathways will be identified.[74-76] Thus, standard atomistic approaches are not ideal tools for investigating film growth processes that involve many different reaction pathways. It should be noted that, not all MD simulation techniques are suitable for study of chemical reactions. Although classical MD can provide insight into the formation and behavior of tribo-films, connectivity between atoms is predefined in such simulations, so they cannot capture the formation of films through covalent bonding with a surface. Reactive MD simulations are relatively new powerful tools to investigate the atomic scale details of chemical reactions including bond forming and bond breaking during tribofilm formation. [18, 77-79] In these methods, bond formation and bond breaking captures by detecting the changes in bond orders that represent the changes in the strength of the bonds.[80] Several reactive forcefields including REBO[81], AREBO[82], COMBO[83, 84], and ReaxFF[80, 85] have been developed with different applications including study of tribolochemical reactions. In the following sections, first, we will review the most important reactive molecular dynamics simulation studies that used to explore thermal and tribofilm formation. Next, those molecular dynamics simulations that subjected the effect of chemical interactions on friction will be discussed.

### 1.4.1. Molecular Dynamics Simulations of Shear-Driven Tribofilm Formation

Many atomic-scale simulation studies have investigated tribochemical reactions leading to tribofilm formation at sliding interfaces. Ab initio molecular dynamics simulations was used to study the behavior of trimethyl phosphite (TMPi) as a lubricant additive used in boundary lubrication conditions. [86] This molecule has been experimentally proven to decrease friction in steel-on-steel sliding contacts due to the formation of an iron phosphide tribofilm.[87] It was reported that molecular dissociation at the sliding iron interface under pressure and discussed the mechanism of iron phosphide formation. Non-reactive MD simulations using Polymer Consistent Force Field (PCFF) were combined with DFT to study shear induced formation of methane from the decomposition of adsorbed methyl thiolate species on copper surface.[88] It was shown that a wide distribution of forces is exerted on the thiolates molecules and that only a small proportion of these adsorbed molecules experience adequately high forces to overcome the activation barrier to reproduce the rate constant measured in experiments.

Reactive MD simulation is a relatively new method to make a bridge between quantum chemistry and classical MD simulation by ensuring a smooth transition of bond formation and dissociation. [89] The friction behavior of silica/phosphoric acid system was investigated by reactive molecular dynamics simulations using ReaxFF forcefield.[76] It was found that the number of interfacial hydrogen bonds between phosphoric acid and silica

surface positively correlated with the friction coefficient and the weaker hydrogen bonds decreases the friction. The results further indicated that a large amount of water formed as a side product of polymerization of phosphoric acid acted as lubricant at the sliding interface and significantly decreased the friction coefficient. Another study has investigated the effect of shear stress on tribo-polymerization. The rate of formation of oligomers from allyl alcohol during sliding on silica glass surfaces was investigated using ReaxFF MD simulations.[90] In parallel, AFM was used to monitor the volume of polymerized product. Both experiments and MD simulations found that the reaction rate increased exponentially with pressure and shear stress. Based on reactive MD simulations, it was found that the anchoring molecules to the surface facilitated transferring of mechanical force from the solid surface to the reactants.[90]

MD simulations have been demonstrated to be extremely useful in contributing to the atomic-scale understanding of physical phenomena that happen at the sliding interfaces. They have been extended recently to analyze chemical reactions at surfaces by using reactive potentials capable of capturing bond breaking and bond formation. Most of the limitations of MD simulations, including small size and time scales compared to experiments, originate from a lack of computational resources. However, emerging MD simulation techniques[91-93] and more powerful supercomputers are decreasing this gap. While challenges still remain for using MD to study triboochemical processes, these simulation can provide insight into atomic-scale events happening at a sliding interface. [94]

### 1.4.2. MD Simulations to Describe Thermal Film Formation

In the absence of shear forces, heating can provide the required energy for the lubricant additives to chemically react with the surfaces and form a surface layer known as thermal film.[14] It is known that thermal films can form through chemical adsorption of decomposing products of lubricant additives[24], and they have very different structures and properties from tribofilms[62, 95, 96 97]. Although recent studies revealed that the tribofilm is a product of shear-induced transformation of the adsorbed thermal film,[24] thermally-activated film formation is still believed to play an important role in the sliding interfaces since they can alter the structure and composition of surfaces prior to sliding.[98, 99] Therefore, understanding the reaction pathways leading to thermal film growth is an important step towards optimization of growth parameters for these films. [9]

MD simulations have been employed to investigate thermal adsorption of different chemical species on metal surfaces leading to the formation of thermal films. For example, the adsorption behavior of three thiazole derivatives on the surface of iron (1 1 0) has been performed using COMPASS (Condensed Phase Optimized Molecular Potentials for Atomistic Simulation Studies) forcefield.[100] The results showed that the three thiazole derivatives can chemisorb on the iron (1 1 0) surface through the thiazole ring and the heteroatoms as well as p-electrons in the aromatic structure. Mohammadtabar et al.[101] studied the formation of iron sulfide film from di-tert-butyl disulfide as an important extreme pressure additive. Comparing reactive MD simulations and ab initio calculation results, they were able to detect the sequence of events including bond formations, bond breaking, and diffusion process which were related to the initial steps of protective film formation. They noted that some of the reaction steps like breaking of S−C bonds act as the rate limiting step of the thermal film formation. In another study, Chia et al. [102] used

reactive MD simulations to investigate the adsorption of organic molecules on a hematite surface, focusing on the effect of molecules polarity on the adsorption rate. They showed that the reactant molecule's polarity affects surface polarization, surface atoms displacements, and thus the structure of adsorbed layer.

### 1.4.3. Atomic-Scale Study of Chemistry-Friction Interrelationship

Tons of previous studies have used reactive MD simulations to explore different effects of tribochemical reactions (i.e., surface amorphization, adhesion, change in the direction of chemical groups, surface reorientation, interface migration, and surface corrugation) on friction. However, the scope of this sub-section will be limited to the effect of friction forces in driving chemical reactions at the sliding interfaces and vice versa. REBO was among the first reactive forcefileds that was used to study the effect of tribochemical reactions on friction. Gao et al. [103] employed REBO potential to explore the friction behavior of a hydrogen-terminated diamond (111) surface sliding on a hydrogen-free amorphous carbon film. Their results showed that the decrease in the level of surface termination with hydrogens increases the friction. Adhesive bonding of undercoordinated carbon atoms between two counterfaces could explain these observations. In another study on diamond-like carbon (DLC) from the same research group[104], it was shown that the stronger bonds increased the vibrational excitation of counterfaces. This phenomenon means energy dissipation and was reflected through spikes in local temperatures emanating from the interface. In another study, a modified REBO forcefield called screened reactive bond-order potential was used the tribological performance of hydrogenated DLC.[105] The obtained results was able to explain the fluctuation in friction coefficient which were resembling the running-in behavior in the experiments by consecutive cold welding of DLC/DLC surfaces and the formation of new low friction interfaces.

A significant number of studies have employed MD simulations to characterize friction resulting from adsorbed chemical species at sliding interfaces.[106-112] The majority of these found that the friction increased with the logarithm of sliding speed, which is consistent with empirical models developed for stress-assisted thermally activated reactions.[113] Chandross et al. used MD simulations to study adhesion and friction between two ordered self-assembled monolayers of alkylsilane chains on a silicon dioxide surface. They realized that, while at low pressures there is a weak dependence of the friction force on shear velocity, there is no such relationship at high pressures.[114] In the experimental side, Chen et al. used AFM to explore surfaces with different chemical natures including surfaces covered by -OH, -COOH, and -$NH_2$, and reported velocity dependent which were showing increasing decreasing trends as a function of sliding speed. They were able to show that the sliding behavior of surfaces depend on their chemical nature, and that the dependency of friction on sliding speed is affected by the ability of surface groups to form domains of cross-linked hydrogen bonds that can be disrupted at a critical stress.[110] The main message in most of the above-mentioned studies is that friction force or shear stress increases proportionally to log (sliding speed) during stress-assisted thermally activated reactions.[37]

## 1.5. Dissertation Outline

Although the use of antiwear additives in lubricants is commonplace, and many experimental studied have focused on the performance of these chemical species, the role of important parameters like shear deformation and surface reactivity is not well understood. Experimental approaches have been limited by the inability to direct probe reactions happening between sliding surfaces. Simulation approaches can resolve this issue, but they are only recently starting to be applied to study tribochemistry. Therefore, the mechanisms of film formation for some of widely used lubricant additives like TCP have not adequately explored using computational tools. One factor limiting simulation approaches in the past is the lack of an empirical forcefield to describe the necessary interactions between atoms in reactive MD simulations. Finally, the mechanisms by which tribofilms reduce friction and wear are not well understood, and there is still debate about how chemical and physical phenomena contribute to friction at atomic scale.

Here, we aim to investigate both the role of chemical reactions in the formation of thermal and tribofilms, as well as their contribution to the friction at sliding interfaces. To fill the gaps in the previous studies, we will use reactive molecular dynamics simulations using the ReaxFF forcefield [80], and will investigate the most critical parameters affecting the development of thermal films and tribofilms. Chapter 1 introduced the importance of lubrication and tribochemical reactions. In Chapter 2, we will discuss our work exploring the role of shear and surface reactivity on mechanochemical reactions that occur during vapor phase lubrication of silica surfaces using alpha-pinene. In Chapter 3, we will focus on the effect of temperature and interactions between additives and the surface on the reactions leading to thermal film formation from tricresyl phosphate (TCP) molecules on an iron oxide surface. Then, in Chapter 4, we will discuss the effect of chemical and physical interactions at the moving surfaces on friction at the atomic scale. Together, this research can provide a detailed picture of what is happening at sliding interfaces. Finally, in Chapter 5, we will summarize the findings, draw conclusions, and identify future research directions.

## Chapter 2 : Shear-Induced Polymerization of Alpha-Pinene Molecules at Sliding Interfaces

### 2.1. Introduction

When mechanical or interfacial shear is involved, it is hypothesized that the applied shear stress can facilitate chemical reactions by decreasing the activation energy or changing the reaction path.[115-118] These theories also posit the existence of a shear-induced activation volume (see Equation 3) which is critical to understanding how much a reaction energy barrier is decreased by shear.[113, 119] However, due to the complexity of processes during sliding, it is difficult to relate this activation volume to specific physical change.[120] In addition to mechanical shear, the surface chemistry of the sliding solids play critical roles in determining dominant reaction pathways and kinetics.[90, 121, 122] Previous studies also showed that the change in the surface reactivity could significantly affect the yield of mechanochemical reactions happens to the interfacial molecules.[31] Intuitively, the molecules chemically anchored to the sliding surface would experience more mechanical shear than the molecules slipping within the interface.[31] However, the exact roles of surface chemistry and mechanical shear need to be unraveled for a deeper understanding of mechanochemistry.

Here, to explore the effect changes in the surface reactivity on the yield of tribochemical reactions, we studied mechanochemical oligomerization reactions of α-pinene molecules confined between two sliding silica surfaces. The design was inspired by the fact that vapor phase lubrication (VPL) experiments can effectively suppress material loss for most solid surfaces.[123] The α-pinene was chosen as the model system because it has a highly strained structure due to the presence of the four-membered ring and C=C double bond in the six-membered ring. As a result, more restructuring and reactions were expected to be detectable in our simulations and experiments. Figure 2.1 illustrates the structure of an α-pinene molecule.

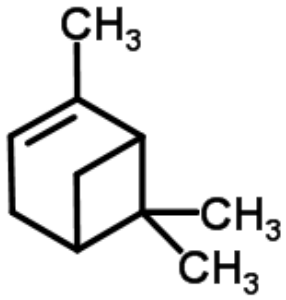


Figure 2.1 The structure of α-pinene includes a highly strained four-membered ring and a double bond

The hypothesis studied in this work is that chemical reactions between the α-pinene and the silica will facilitate oligomerization during sliding. We used reactive MD simulations with a ReaxFF reactive force field. The simulation results were partially validated by comparison to experimental results performed by our collaborators at Penn State. The combination of simulation and experimental results then revealed mechanistic

insights into the shear-induced polymerization of α-pinene on silicon oxide surfaces. The roles of chemisorption and shear-induced deformation of molecules observed in this study can be generalized to other mechanochemical reactions at sliding interfaces.

## 2.2. Methods

Shear-induced mechanochemical polymerization of α-pinene molecules between two amorphous silica slabs was investigated using ReaxFF-MD simulations. A slab-on-slab geometry was chosen for the simulation to represent the elastic flattening of the solid surface in the ball-on-flat contact zone. This also resulted in confinement of reacting molecules within the sliding interface. To capture the effect of surface reactivity on the yield, simulations were performed both on non-hydroxylated and hydroxylated surfaces. The non-hydroxylated surface was modeled as silicon oxide produced in the absence of water molecules (see Figure 2.2). The hydroxylated surface was created by modeling reactions with water at 500 K (see Figure 2.3). Two amorphous $SiO_2$ slabs were created as described as follow to have two surfaces with different surface reactivities.

The amorphous silica slabs were derived from a cristobalite $SiO_2$ structure. This crystalline material is a high-temperature form of silica glass that is metastable below 1740 K.[124] The standard method of heating and cooling was used to create the amorphous structure of the two slabs in the sliding model.[125] Figure 2.2 illustrates the initial and final structures along with the temperature and potential energy during the heating and cooling cycles. The NVT (constant number of atoms, volume and temperature) ensemble was used during heating from room temperature to 4000 K and then cooling down again to 300 K. To minimize strain in the resultant amorphous structure, the heating and cooling rate was fixed at 0.02 K/fs which was the lowest rate possible within the timescale constraints of the simulation.

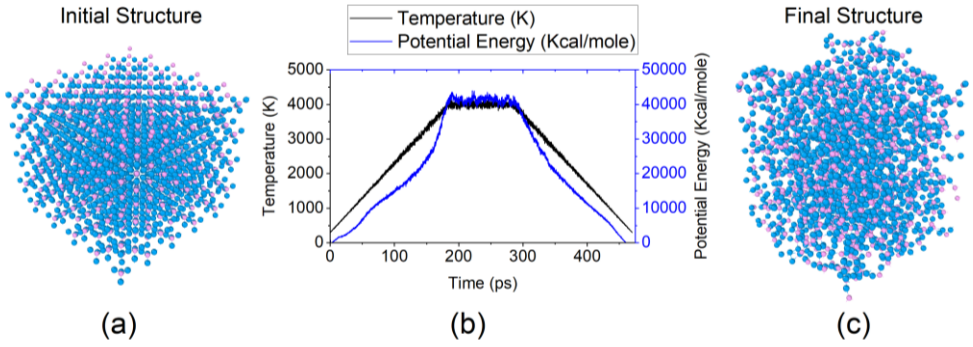


Figure 2.2 (a) Cristobalite SiO2, (b) changes in temperature and potential energy during the heating and cooling cycle used to create the amorphous structure, and (c) final structure of the amorphous silica.

The physical data extracted from characterization of the amorphous silica model were compared with those reported in previous studies, as shown in Table 2.1. All properties calculated for the amorphous structure agreed with the previously reported data within 6% error.

Table 2.1 Properties of the amorphous silica glass created in this work compared to the results reported in previous MD simulations and experiments.

| | **This study (from MD simulation)** | **Previous MD simulations [126]** | **Experimental values [127, 128]** |
|---|---|---|---|
| Bulk density ($g/cm^3$) | 2.1 | 2.1 | 2.2 |
| Si-O RDF first peak (Å) | 1.58 | 1.56 | 1.62 |
| Si-O-Si (degree) | 152.0 | 151.0 | 144.0 |
| O-Si-O (degree) | 110.5 | 110.0 | 109.5 |

With the aim of creating two systems with different surface reactivities, hydroxylation of the amorphous surface was carried out for one model. Figure 2.3 shows the model system in which 300 water molecules were added at the top of the amorphous silica (Figure 2.3(a); box size = 3.19×3.19×3.00 $nm^3$). Then, the temperature was increased from 300 K to 500 K and NVT simulations were performed for 800 ps. Figure 2.3(b) shows the change in the density of silanol groups formed at the surface. The density of silanol groups increased and reached a saturation value at ~300 ps, after which there was negligible change. Lastly, the excess un-reacted water molecules were removed from the system. Figure 2.3 shows the density of surface functional groups for the non-hydroxylated and hydroxylated models. Based on the obtained structure, density of defects decreased upon hydroxylation: for example, from ~1.2 oxygen radicals per $nm^2$ on the non-hydroxylated surface to ~0.5 per $nm^2$ on the hydroxylated surface (see Figure 2.4).

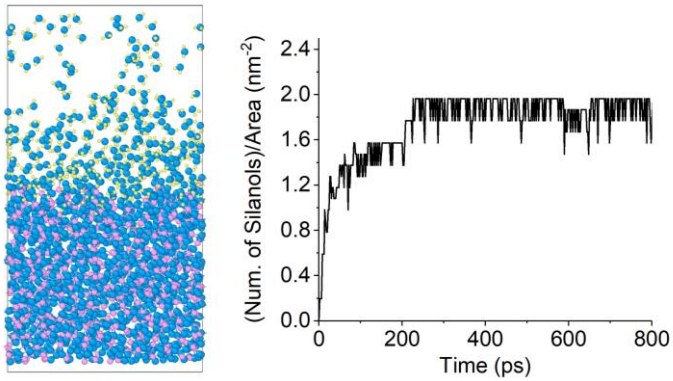


Figure 2.3 (a) Model system for simulation of hydroxylation. (b) Density of silanol groups on the silica surface during the hydroxylation process.

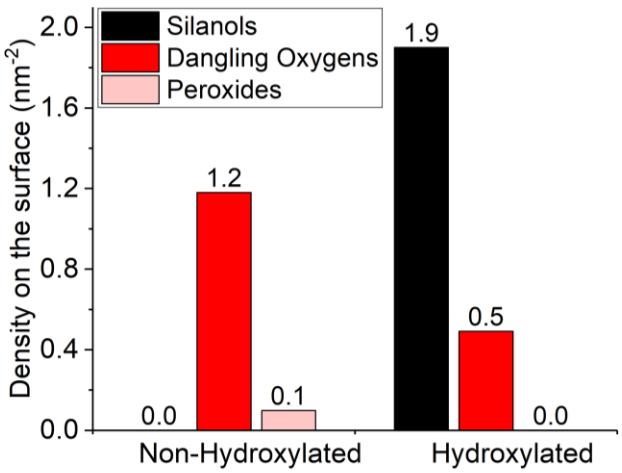


Figure 2.4 Density of different functional groups on the non-hydroxylated and hydroxylated model silica surfaces.

After creating two structures with different surface reactivity, 31 α-pinene molecules were confined between the amorphous silica slabs, to form approximately a monolayer of α-pinene on each surface. The size of the simulation box was 3.19×3.19×8.00 $nm^3$. Figure 2.5 shows different step of simulations. Each MD simulation consisted of three main steps: (i) energy minimization and equilibration at 300 K until the energy was stable, (ii) compression by moving the top slab toward the bottom slab in the z-direction at a speed of 5 m/s until the average pressure was approximately equal to the target value (either 1 or 3 GPa), and (iii) sliding the top slab at 10 m/s in the x-direction for 2 ns. In order to study the effect of shear, the simulations were performed with and without sliding at 1 GPa and 3 GPa. Since the flash temperature has been shown to be negligible during sliding in experiments, all simulations were carried out at 300 K by applying the NVT (constant number of atoms, volume and temperature) ensemble. The ReaxFF force field was employed with parameters to describe interactions between Si/O/C/H atoms.[129,80] Performing the ReaxFF simulations rather than the quantum mechanics calculations enabled us to investigate the dynamics of the system at a more extensive physical length scale and a longer timescale. MD simulations were performed using the Large Atomic/Molecular Massively Parallel Simulation (LAMMPS) software[130] and the post-processing was carried out using OVITO software.[131]

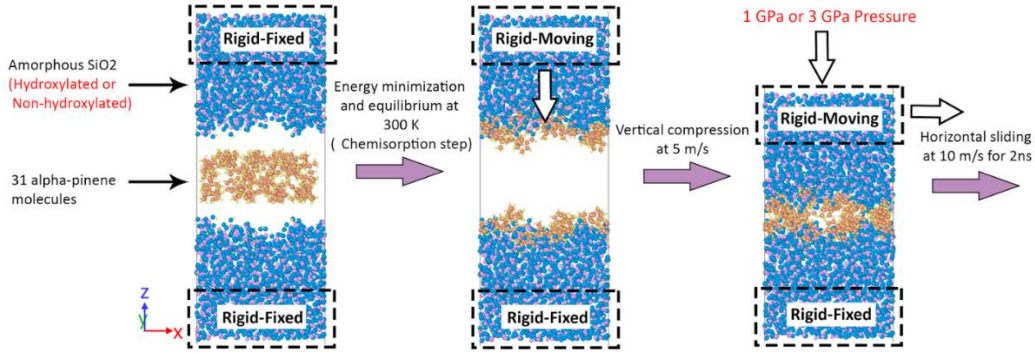


Figure 2.5 The configuration of the model system illustrating the three stages of the MD simulations. From left to right: energy minimization, compression, and sliding.

The experiments presented in the following pages performed by our collaborators (Xin He and Dr. Seong Kim group at Penn State University) and were included surface preparation, VPL experiments, X-ray photoelectron spectroscopy (XPS) analysis, and calculation of critical activation volume using pressure dependent measurements in VPL experiments.[75]

## 2.3. Results and Discussion

Figure 2.6 shows the friction coefficients measured by Xin He (Penn State University) during VPL for the fully hydroxylated and thermally dehydroxylated silica surfaces. Thermal dehydroxylation was used as a means of making the surface more reactive. Thermal dihydroxylation will occur through dehydrations reaction among adjacent hydroxyl groups forming siloxane bridges.[132] Such siloxane bonds at the surface would be subject to high strain (due to unfavorable bond angles) and thus have high reactivity.

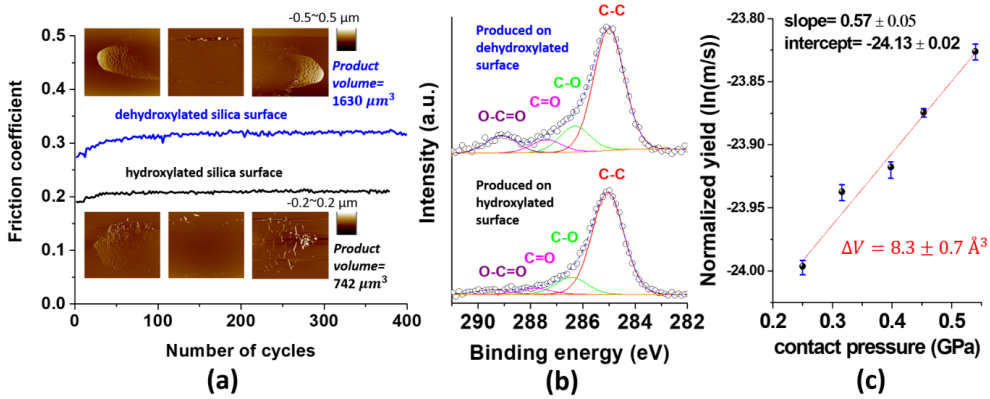


Figure 2.6 Friction coefficients of hydroxylated and dehydroxylated surfaces in α-pinene VPL conditions at a 40 % partial pressure relative to saturation. (b) C1s XPS spectra of the shear-induced polymers produced on silicon oxide surfaces with two different surface

conditions. (c) Semi-log plot of the normalized tribo-polymer yield against the contact pressure for α-pinene sheared on the dehydroxylated silicon oxide surface. These experiments were performed by Xin He at Penn State University. [133]

For chemical analysis purposes, Dr. Kim's group at Penn State used the thermally dehydroxylated surface because it allowed better control of the surface chemistry. Atomic force microscopy (AFM) imaging after the VPL tests provided accumulations of reaction products in and along the slide track (insets in Figure 2.6(a)). The dehydroxylated surface had a higher friction coefficient and significantly more products than the hydroxylated surface. The higher friction coefficient (~0.3) is within the typical range for polymer surfaces.[134] The C1s XPS analysis of the reaction products (Figure 2.6 (b))) shows the presence of oxygen groups (C-O at ~286.5 eV, C=O at ~287.5 eV, and O-C=O at ~289 eV), even though α-pinene has no oxygen. The dehydroxylated surface produced more oxygenated products than the hydroxylated surface. These results imply that the surface chemistry of the solid substrate plays a critical role in reaction yield and pathways.

For the dehydroxylated surface, the shear-induced polymerization yield was high enough to conduct contact pressure dependence measurements to determine the critical activation volume ($\Delta V^*$), as shown in Figure 2.6 (c).[38] This could not be done reliably on the hydroxylated surface because the reaction yield was too low to be measured with enough precision. Using an Arrhenius-type activated reaction model,[25, 120, 135] the $\Delta V^*$ of this reaction was found to be about 8.3±0.7 $Å^3$ on the dehydroxylated surface [see the next section for calculation details]. This value corresponds to ~3% of the molecular volume of α-pinene in the liquid state (liquid molar volume divided by the Avogadro's number). In equilibrium conditions, molecules are incompressible. This then raises a question about the physical meaning of the volume change between the reactant and transition states of the molecule.

The molecular origins of the higher yield of shear-induced polymerization on the dehydroxylated surface, the production of oxygenated products from oxygen-free precursor molecules on silicon oxide, and the critical activation volume calculated from the pressure-dependence data could not be understood from the experimental studies alone; so, ReaxFF-MD simulations were performed to address these questions. Figure 2.7 (a) and (b) show the molecular weight (MW) distribution of molecular species remaining after applying 1 GPa pressure for 2 ns without any lateral shear action. On both non-hydroxylated and hydroxylated surfaces, no association products of α-pinene molecules were observed. The slight increase in the molecular weights is due to the uptake of oxygen atoms from the silicon oxide substrates.

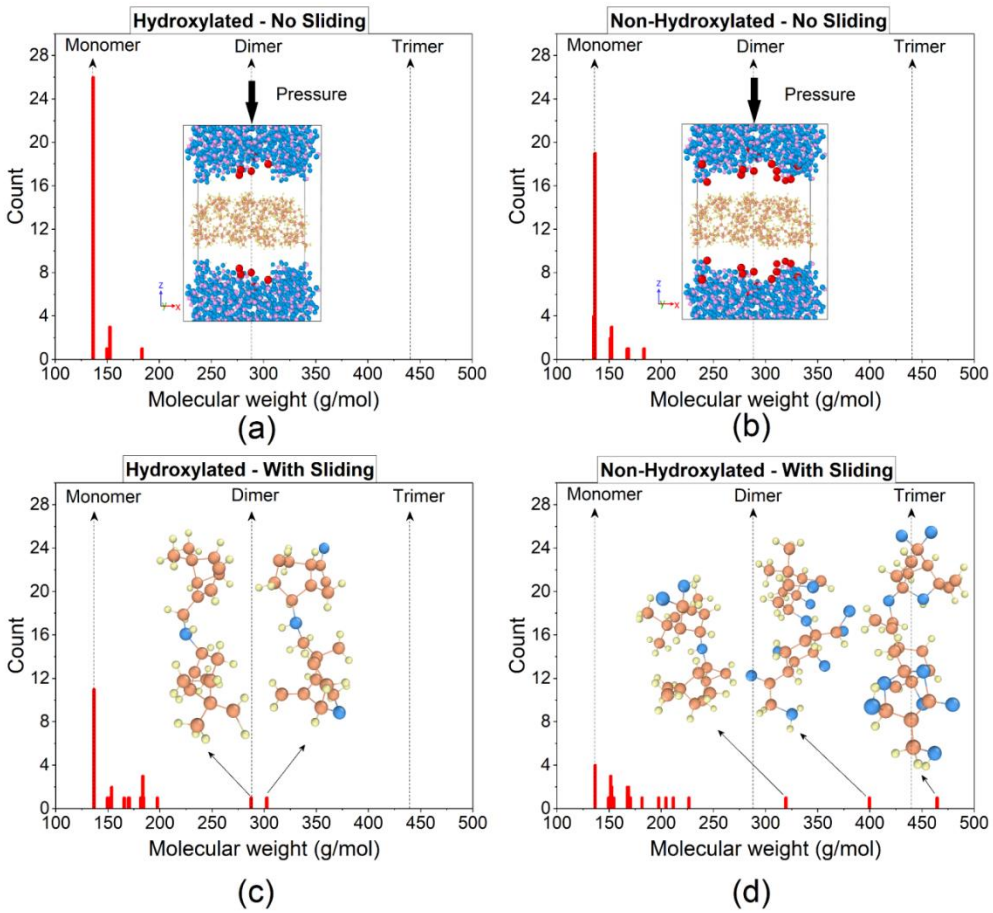


Figure 2.7 Histograms of the molecular weights of species with ten or more carbon atoms from simulations at 1 GPa for (a) hydroxylated surface without sliding, (b) non-hydroxylated surface without sliding, (c) hydroxylated surface after 2ns of sliding, and (d) non-hydroxylated surface after 2ns of sliding. Side view images of the MD simulations are shown as insets in (a) and (b), where reactive surface sites are highlighted by red spheres. Snapshots of representative shear-induced reaction products are shown as insets to (c) and (d).

Figure 2.7 (c) and (d) show the MW distribution of species with 10 or more carbon atoms after shear. Here, the formation of shear-induced reaction products is evidenced by the presence of products whose MWs are heavier than dimers. The comparison with the control case without shear (Figure 2.7 (a) and (b)) clearly shows that oligomerization does not occur without interfacial shear; in other words, chemical reactions are facilitated or initiated by interfacial shear. There is significantly more oligomerization on the non-hydroxylated surface, which is congruent with the experimental result (Figure 2.6). Note that, due to the limited sliding time and number of reactant molecules in MD simulations, high MW products could not be formed.

### 2.3.1 Pressure dependence and critical activation volume calculation

Based on the models proposed for the mechanically assisted thermal activation phenomena,[25-27, 135, 136] the rate of reaction (or yield at a constant reaction time) can be expressed as an Arrhenius-type function:

$$r_y = A \exp\left(-\frac{E_a - \sigma \Delta V^*}{k_b T}\right) \quad (2\text{-}1)$$

where $r_y$ is the reaction rate or normalized yield, A is a preexponential factor, $E_a$ is the activation energy barrier for thermal reaction, $\sigma$ is the applied shear stress, $\Delta V^*$ is the critical activation volume, $k_b$ is the Boltzmann constant, and T is the substrate temperature. The shear stress term can be expressed with the applied contact pressure (P) and friction coefficient ($\alpha$):

$$\sigma = \sigma_0 + \alpha P \quad (2\text{-}2)$$

Here, $\sigma_0$ and $\alpha$ are constants. Inserting equation (2) in equation (1) gives:

$$\ln(r_y) = \left(\ln A + \frac{\sigma_0 \Delta V^*}{k_b T} - \frac{E_a}{k_b T}\right) + \frac{\Delta V^* . \alpha}{k_b T} P \quad (2\text{-}3)$$

When the flash temperature increase due to friction is negligible, the terms in the parentheses on the right side of equation (2-3) would remain constant.[137] Therefore, on a semi-log plot of the reaction yield against the applied pressure, the slope can be used to estimate $\Delta V^*$.

MD simulations revealed that the increase in applied contact pressure from 1 GPa to 3 GPa resulted in more products at the end of sliding (Figure 2.8). When these two data points were used for the Arrhenius-type activation model analysis, $\Delta V^*$ was estimated to be ~6 Å$^3$ on the non-hydroxylated surface. Although accuracy of this value is limited due to insufficient data points, it is still intriguing to note that the simulation value is reasonably close to the experimentally determined $\Delta V^*$ =8.3±0.07 Å [75] .These observed consistencies imply that the molecular details available in the ReaxFF-MD simulations are relevant to the experimental observations, despite the differences in size and time scales between the experimental and simulation conditions[75].

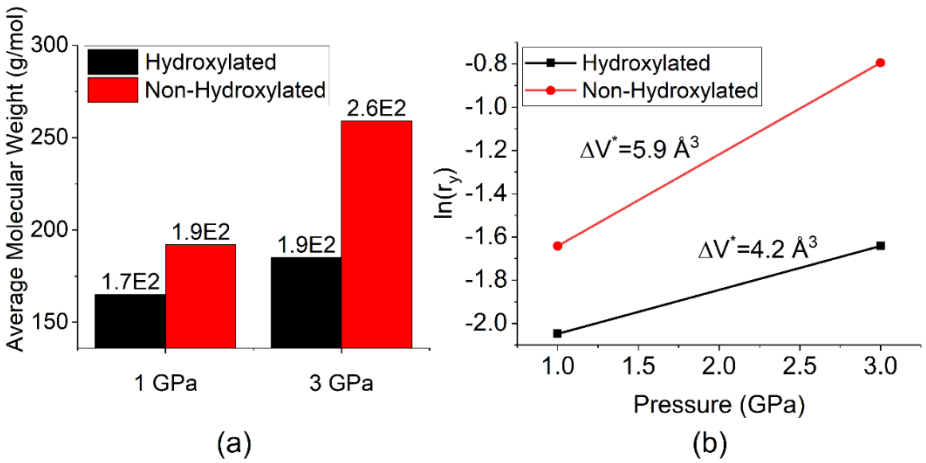


Figure 2.8 (a) Average molecular weight of reaction products containing more than 10 carbon atoms in MD simulations for the hydroxylated and non-hydroxylated surfaces at contact pressures of 1 GPa and 3 GPa. (b) Calculation of the critical activation volume

based on the number of α-pinene molecules associated in simulations at 1GPa and 3GPa conditions.

### 2.3.2 Oligomerization reaction pathway

The first chemical interactions between the α-pinene molecules and silica surfaces happen during equilibrium step before applying any vertical compression. Figure 2.9 shows the comparison between the chemisorption of α-pinene molecules on two surfaces. As illustrated here, more hydrocarbon molecules reacted with the non-hydroxylated surface due to more available high energy dangling oxygens and peroxides on this surface compared to the hydroxylated surface. However, the chemisorption events do not lead to association of the molecules.

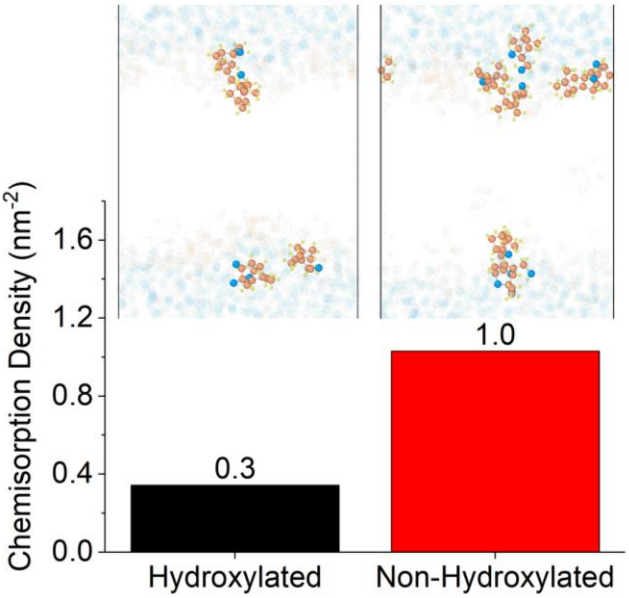


Figure 2.9 Density of chemisorbed α-pinene molecules on the hydroxylated and non-hydroxylated surfaces at the end of the energy equilibrium step in MD simulations.

In the next step, the reaction pathway during sliding process were investigated. Figure 2.10 displays snapshots from the simulation following the trajectory of one α-pinene molecule. At $t$ = 114 ps after initiation of sliding (Figure 2.10 (b)), the surface O1 atom is approaching the C6 atom of the α-pinene molecule. At $t$ = 120 ps (Figure 2.10 (c)), the O1 atom is covalently bonded to the C6 atom; at $t$ = 124 ps (Figure 2.10 (d)), the second oxygen is attached to the C1 atom and the covalent bond between C1 and C6 is broken. Following the trajectories of all molecules forming association products, it was found that α-pinene molecules are first oxidatively activated by reactions with dangling oxygen groups at the surface before the sliding and/or hydroxyl groups during the sliding before they are associated with another molecule. This result indicates that the oxidative chemisorption or activation of the interfacial molecule is necessary for shear-induced oligomerization reactions to occur.

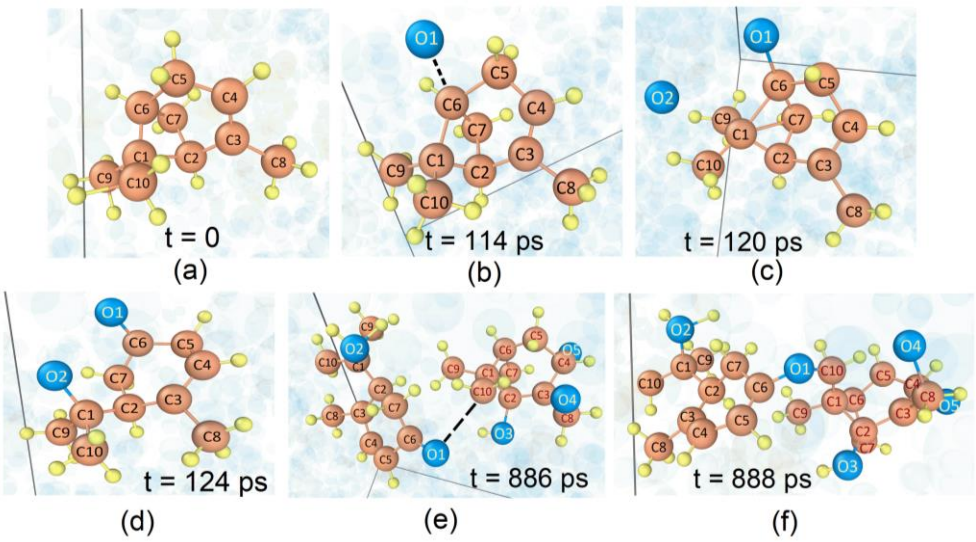


Figure 2.10 Snapshots at various times from ReaxFF-MD simulations following one α-pinene molecule. The numbers on atoms are given following the IUPAC nomenclature. The 4-membered ring consists of C1, C2, C7, and C6. The 6-membered ring is made of C2, C3, C4, C5, C6, and C7. The C=C double bond exists between C3 and C4. The C8, C9, and C10 are methyl side groups. The oxygen atoms are from the silicon oxide substrate and numbered following the order of covalent bond formation to α-pinene molecules. Atom colors correspond to: C-brown, O-blue, and H-yellow.

The oxidized intermediate species in Figure 2.10 (c) meets with another α-pinene molecule at $t$ = 886 ps (Figure 2.10 (e)). Here, it is important to note that a covalent bond is formed between the O1 atom attached to the C6 of the first molecule and the C10 atom of the second molecule. For all 10 association products formed within the 2 ns simulation duration, the covalent bonds associating two molecules are formed between oxygen atoms of the oxidized intermediate species and the carbon atoms of the neighboring molecule (see Figure 2.11). This is drastically different from typical catalytic polymerization reactions of α-pinene under thermal conditions, where cationic intermediates are formed and the polymerization proceeds through C-C covalent bond formation.[138] This difference implies that thermal reaction mechanisms cannot be applied or utilized to explain mechanochemical reactions.

### 2.3.3 Role of internal strain

When the 10 oligomers produced in MD simulations are analyzed (Figure 2.11), it is found that the C=C double bonds in the 6-membered ring are more likely to be attacked by the oxygen atom of the intermediate species and activated by oxidation reactions with the surface. The next most likely association reaction appears to be with the 4-membered ring or methyl groups attached to the 4-membered ring. These are the highly strained regions within the α-pinene molecule. Although the number of products is not large enough to give reliable statistics, this trend suggests that the internal strain of molecules plays a critical role in mechanochemical reactions.

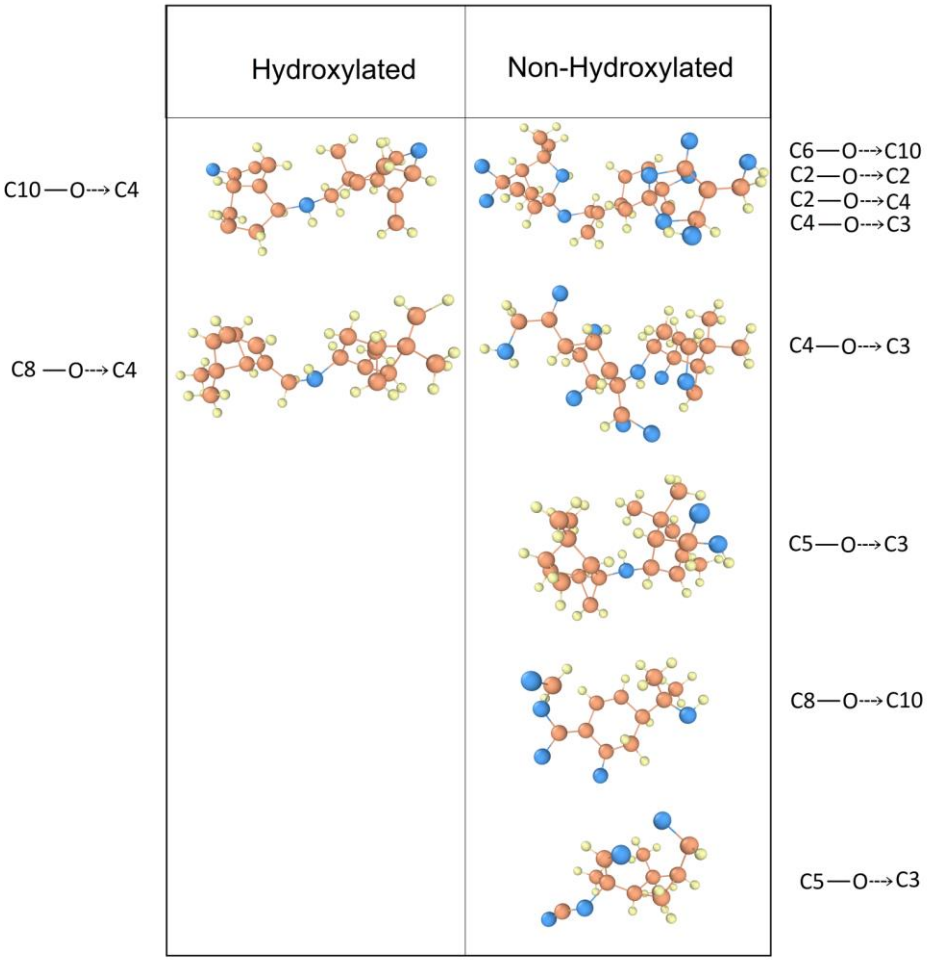


Figure 2.11 Association of two molecules via C-O-C bond formation. Snapshots of the hydrocarbon species formed in MD simulations with the hydroxylated and non-hydroxylated silica surfaces after 2 ns sliding. The atom numbers at the connection between molecules are provided adjacent to each snapshot. It is important to note that all association products are connected through the C-O-C ether bond; no products were found to be connected via direct C-C covalent bonding.

The role of internal strain in the oxidative activation of α-pinene forming intermediate species is shown in Figure 2.12. At $t$ = 98 ps, the C1-C6 bond length ($d_{C1\text{-}C6}$) is slightly elongated from 1.5 Å to 1.75 Å, which is accompanied by an increase in the C2-C7-C6 bond angle (θ7) and a decrease in θ1. This deformation appears to facilitate the association of C6 with O1 at $t$ = 106 ps, at which time $d_{O1\text{-}C6}$ decreases from 2.3 Å to 1.9 Å (still too far to covalently bond). Compared to the total energy for a small cluster of reacting species only, the physical deformation is found to substantially reduce the activation energy for the oxygen transfer from the surface to α-pinene.[75] As O1 approaches C6 (t = 106 ps), $d_{C1\text{-}C6}$ is elongated further to 1.9 Å, θ6 decreases to 84°, and θ7 increases further to 110°. This corresponds to Figure 2.10 (b). Finally, at $t$ = 124 ps (which corresponds to Figure 2.10 (d)), the covalent bond between O1 and C6 is formed

(decreasing $d_{O1\text{-}C6}$ to 1.5 Å). At the same time, O2 is covalently bonded to C1 ($d_{O2\text{-}C1}$ decreases from ~3 Å to 1.5 Å); this is accompanied with the ring opening, which is evidenced by the increase of $d_{C1\text{-}C6}$ from 1.9 Å to 3.4 Å and the increase of θ2 and θ7 to ~140°. Also, $d_{C1\text{-}C2}$, $d_{C2\text{-}C7}$, and $d_{C6\text{-}C7}$ get slightly shorter by 0.1 Å (data not shown). During this entire process of forming the oxidized intermediate species, the effective volume change is about 10 Å$^3$. In the subsequent association between the activated intermediate and α-pinene, the shear-induced deformation of the molecule is found to facilitate the C-O-C bond formation [75].

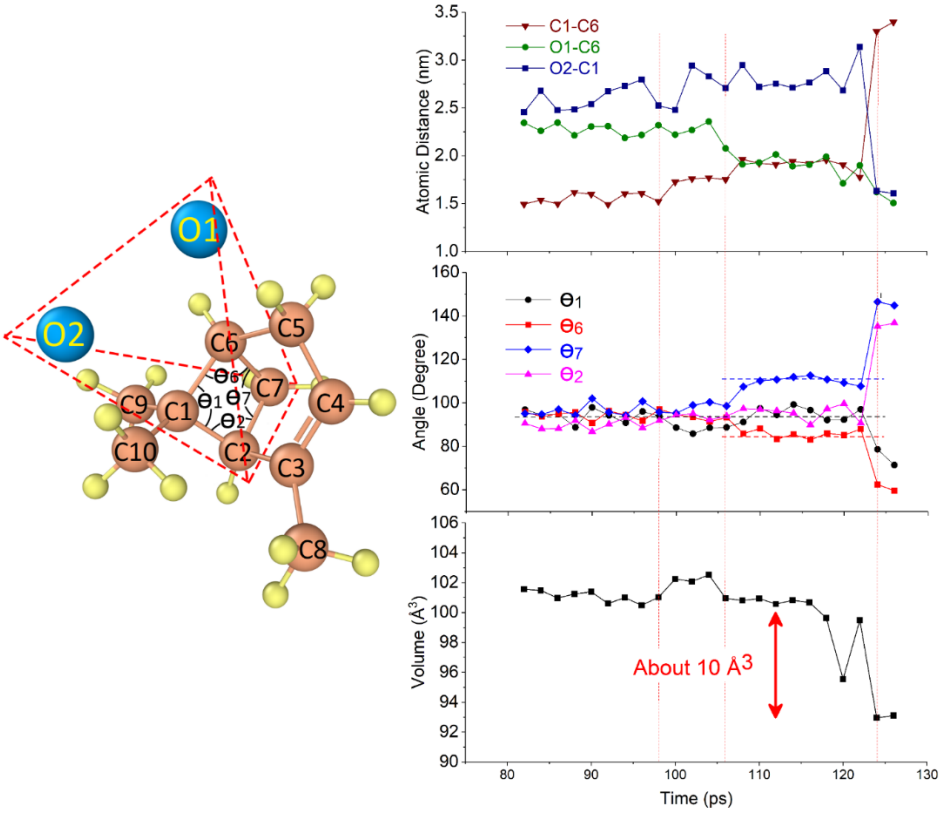


Figure 2.12 Physical deformation of the 4-membered ring during the oxidation of α-pinene by reaction with surface oxygen atoms (steps shown in Figures 2.10 (b), 2.10(c), and 2.10(d)). Here, θ1, θ2, θ7, and θ6 represent the C6-C1-C2, C1-C2-C7, C2-C7-C6, and C7-C7-C1 bond angles, respectively. The volume of a tetrahedral box (identified by dotted lines) is also shown.

MD simulation results also explain the XPS analysis data (Figure 2.6 (b)) which indicate that the shear-induced polymerization products are highly oxidized. The polymerization occurs not through the formation of direct C-C covalent bond between two molecules, but through the formation of the C-O-C ether bond (responsible for the 286.5 eV peak in Figure 2.6 (b)). Also, unreacted terminal oxygen atoms will be further oxidized, forming carbonyl or carboxyl groups (287.5 eV, and 289 eV in Figure 2.6 (b)) upon exposure to air. In simulations, the non-hydroxylated surface produces more oxidized

products than the hydroxylated surface (see Figure 2.7 and Figure 2.11), which is congruent with the XPS result showing more oxidized C1s components for the reaction products on the dehydroxylated surface (Figure 2.6 (b)).

## 2.4. Conclusion

Reactive MD simulations of hydroxylated and non-hydroxylated surfaces provided atom-scale explanations for shear induced polymerization of α-pinene. First, non-hydroxylated surfaces were shown to react more with the α-pinene and have more oligomerization during shear than the hydroxylated surfaces. These results were consistent with VPL experiments performed by Dr. Kim's group at Penn State which reported more tribo-polymerization when dehydroxylated silica surfaces were used. Also, the activation volumes calculated from the pressure-dependence of the yield in simulations and experiments for the non-hydroxylated surface were comparable to each other. This consistency with experimental observations indicated the simulations were indeed relevant to the experiments and supported the hypothesis that more reactivity of the substrate surface corresponds to higher oligmerization yield during shear. Second, the simulations showed that oligomerization between two α-pinene molecules occurs via oxygen atoms obtained from surface reactions, providing direct evidence of the connection between surface reactivity and yield. Lastly, detailed analysis of individual molecules during the simulation revealed that shear facilitates association reactions through deformation of strained parts of the molecule, which in turn enables the molecule to bond with surface oxygen as the first step towards oligomerization.

## Chapter 3 : Thermally Activated Film Formation from TCP on Iron Oxide Substrate

### 3.1. Statistical analysis of temperature-dependent adsorption reactions

Many solid or semi-solid films are grown using techniques that involve gas or liquid phase species chemically reacting with a solid surface. Understanding the initial chemisorption reactions leading to film growth is an important step towards optimization of these films. Such reactions can be inferred from measured rates of film growth and surface characterization, but the elementary steps cannot readily be observed experimentally. An alternative to experimental approaches is atomistic modeling methods, i.e., density functional theory (DFT), kinetic Monte Carlo (KMC) or molecular dynamics simulation (MD), that provide atomic scale information about the elementary reaction steps. However, the challenge for simulation-based approaches is that film growth may occur through many different reactions with varying statistical likelihood, especially at high temperatures or on irregular, amorphous or disordered, surfaces. DFT can provide detailed and highly accurate information about a given reaction, but the reactions must be identified *a priori* and the computational cost of the method typically means that only a few possible reactions can be studied (e.g. [73, 139, 140]). KMC enables much larger systems to be modeled, but the kinetics are typically based on DFT calculations so the approach is again limited to known reactions (e.g.[141-143]). In MD, multiple reactions can be identified during the simulation as atoms interact and move, but traditional MD is limited to relatively small size (nanometer) and time (nanosecond) scales, which means that only one or a few reactions will be identified (e.g. [75, 144]). Thus, standard atomistic approaches are not ideal tools for investigating film growth processes that involve many different possible reactions.

One way to simulate a larger number of different reactions is to extend the duration of MD simulations. This can be done using a variety of techniques,[145] including parallelization in time, i.e. multiple replicas of a model system run in parallel. It has been shown that parallelization does not have an effect on the relative probabilities of possible reactions, so both the sequence of reactions and reaction times in a parallel simulation are the same as those that would be observed in one long serial simulation.[146] For surface reactions that may be the precursors to film growth, use of multiple replicas enables statistical analysis of the possible reaction sites. To model chemical reactions on surfaces, these parallel simulations have been performed either using hybrid quantum mechanical/molecular dynamics methods[147, 148] or molecular dynamics with reactive empirical potentials.[149-152] Such simulations have been applied to model $SiH_3$ on amorphous silicon,[150] oxynitridation on Si(001),[149] N adatoms on vanadium nitride (001),[147] oxidation of Si(100),[151] $C_{60}$ molecules on a diamond substrate,[152] and Ar plasma bombardment on an organosilicate glass. [148] These studies demonstrate the utility of parallel reactive simulations for statistical analysis of reactions leading to film growth, and specifically surface reactivity. Here, we study a more complex reactant molecule that contains multiple possible sites for chemisorption and so focus on the reactant as opposed to the surface.

The specific system investigated is tri-cresyl phosphate (TCP) interacting with an amorphous iron oxide surface. This system is highly relevant because TCP is a common aviation lubricant additive that functions by chemically reacting with ferrous surfaces to form protective films. Such films play a key role in enabling moving mechanical components to operate efficiently, but the elementary steps leading to film growth are still poorly understood. Experimental studies have been performed to characterize TCP film for several

decades and have suggested multiple possible film formation mechanisms, including corrosion, thermal decomposition, hydrolytic decomposition, and oxidative decomposition.[153] However, few simulation-based studies have sought to explore these mechanisms. Non-reactive MD simulations of TCP and tri-n-butyl-phosphate have been reported,[154, 155] but none included chemical reactions with iron oxide, in part due to lack of availability of an empirical potential for all of the necessary interactions. Also, the DFT calculations on the previously-proposed mechanisms for TCP on Fe(110) found that they are all energetically feasible.[73] However, as mentioned previously, the limitations of DFT precluded a statistical analysis of reactions sites.

In this study, we applied parallel reactive MD simulations to model chemical reactions between TCP and an amorphous iron oxide surface. The simulations used a new ReaxFF force field[80] for which our other members of our group have developed new parameters to describe Fe/P/O interactions.[156] The simulations described interactions between a single TCP molecule and the amorphous iron oxide surface at temperatures from 300 to 700 K. At each temperature, one hundred replica simulations were run, where the replicas differed only in the initial position of the TCP relative to the surface and the initial velocity distribution of the atoms. We analyze the frequency of TCP–surface reactions for each atom type and each unique reaction site on the TCP. Then, the composition of the chemisorbed material was analyzed and compared to previous experimental measurements. The results are relevant to TCP film growth specifically, but the approach demonstrated here can be applied more generally to study reaction sites on organic molecules using parallel reactive MD with statistical analysis.

### 3.1.1. Reactive molecular dynamics simulations

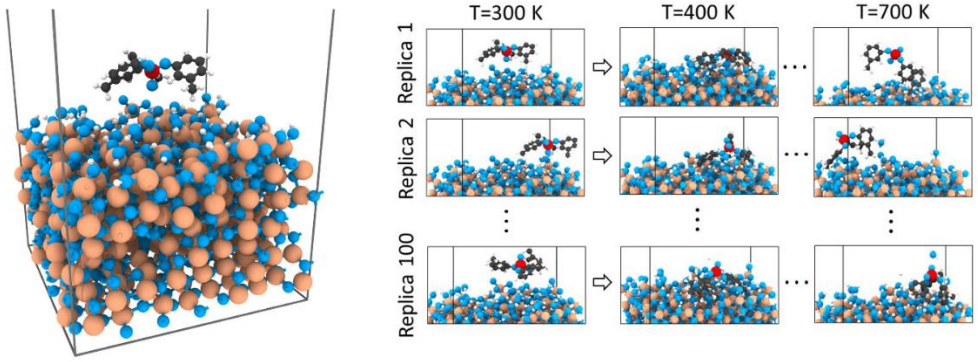


Figure 3.1 (a) Snapshot of one model system consisting of a TCP molecule on a passivated amorphous iron oxide surface. (b) This model was replicated 100 times with diff t initial positions of the TCP relative to the surface and run at temperatures from 300 to 700. Red, black, blue, orange and white spheres represent phosphorus, carbon, oxygen, iron and hydrogen atoms, respectively.

The MD model system consisted of a single TCP molecule on an amorphous iron oxide surface. The amorphous iron oxide was created by first annealing a slab of

crystalline $Fe_3O_4$ (2.5 nm ×2.5 nm in the plane of the surface and 2.0 nm thick). The bottom 0.3 nm of the substrate was held fixed, forming the boundary in the surface-normal direction, and periodic boundary conditions were applied in the directions in the plane of the surface. Next, to create the amorphous material, the temperature was first increased from 300 to 4000 K over 25 ps, held at 4000 K for 125 ps, and then decreased back to 300 K over 500 ps. Prior to amorphization, the iron coordination number was 4 (37%) or 6 (63%), as expected based on the $Fe_3O_4$ crystal structure. After the amorphization process, the coordination number for most of the iron atoms was 4 (78% in the bulk and 80% on the surface), with the remaining atoms having coordination numbers of 1 (0.2% bulk, 3% surface), 2 (3% bulk, 8% surface), 3 (17% bulk and 8% surface) and 5 (1% bulk, 0% surface). Finally, to passivate the surface, 300 water molecules were placed over the amorphous iron oxide surface and the temperature of the system was set to 700 K for 500 ps to accelerate the hydroxylation reactions. The simulation was run until the potential energy was stable, after which any atoms not covalently bonded to the surface were removed. At the end of this process, the hydroxyl group density on the surface was 8.3 $nm^{-2}$, consistent with the range of 5 to 9 $nm^{-2}$ reported in previous studies.

This substrate was used to create 100 model systems with a single TCP molecule at different and randomly chosen initial positions relative to the surface in each model. Two different initial TCP orientations were modeled, with the double-bonded oxygen atom pointing down towards the surface in 50 simulations and the oxygen pointing up in the other 50 simulations. A snapshot of one model system is shown in Figure 3.1 (a). For all 100 models, MD simulations were run with the temperature controlled using a Nosé-Hoover thermostat applied to the free atoms. Simulations were run at 300–700 K in increments of 100 K for up to 1 ns, where the duration at each temperature was determined based on when the number of bonds reached steady state. At each temperature above 300 K, the initial configuration was taken from the final configuration of the simulation at the next lower temperature. Figure 3.1 (b) shows a schematic of the parallel simulation approach. Chemical bonding information was output at 1.25 ps intervals and a bond-order cut-off value of 0.3 was used to identify covalent bonds. The number of bonds was averaged over the steady state region of the simulation (during the last 25 ps at each temperature).

All simulations were run using the large-scale atomic/molecular massively parallel simulator (LAMMPS)[130] with a timestep of 0.25 fs, and post processing of results was carried out using OVITO software.[131]

### 3.1.2. Results and Discussion

100 parallel simulations of TCP on an amorphous iron oxide surface were run using a new set of ReaxFF parameters that is developed for Fe/P/O system. The number of covalent bonds formed between TCP and the surface was analyzed and categorized based on atom–atom type, i.e. Fe–C, Fe–O or O–P, where the film element corresponds to an atom in the iron oxide and the second is in the TCP. Bonds between all other combinations of atoms had a probability of less than 3% at any temperature, so they were not included in the analysis. Also, bonds with H atoms were excluded from the analysis since they do not contribute significantly to film formation. The probability of each bond at the different temperatures is shown in Figure 3.2. Note that there was no difference between the trends

exhibited by the simulations with the two different initial TCP orientations at 300K, so they were analyzed together. On average, there was more TCP–surface bonding at the higher temperatures, although the distribution of elements involved changed with temperature. Comparing the different types of bonds, it is evident that Fe–C bonds were the most common at any temperature.

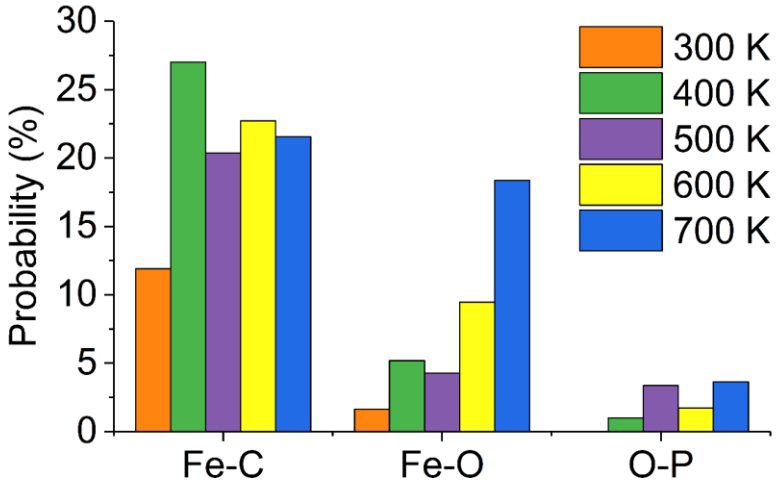


Figure 3.2 The probability of a bond forming between the TCP and amorphous iron oxide surface as a function of temperature for each atom–atom pair, where the film element corresponds to an atom in the iron oxide and the second is in the TCP.

The above analysis considers the Fe–C bonds and the Fe–O bonds collectively. However, in reality there are seven unique C atoms and two unique O atoms available for reaction on the TCP, in addition to the P atom. The unique reaction sites on the TCP are identified and labeled in the upper left panel of Figure 3.3. The probability analysis was then repeated for each unique reaction site on the TCP and the results are illustrated graphically in Figure 3.3. At temperatures between 300 and 500 K, the most reactive atoms were C5 and C6, likely because of their location at the outermost edge of the benzene ring. As the temperature increased, the O atoms became more reactive, until O1 was the most reactive site on the TCP at 700 K. At the highest temperatures, we also observed statistically significant reactions at the C1 and C7 sites.

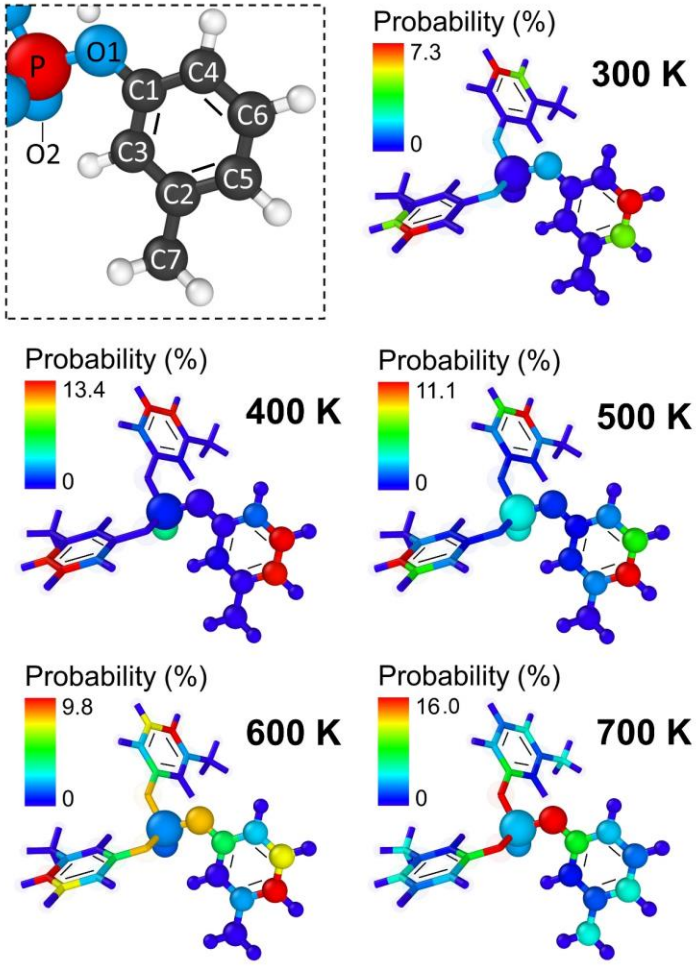


Figure 3.3 The reactivity of individual atoms in the TCP molecule at different temperatures. The unique reaction sites on the TCP are identified and labeled in the upper left panel. Note that the ranges of the color scales are diff t for each temperature, so this film does not enable comparison between temperatures but rather comparison between the different reaction sites at each temperature.

To quantify the above analysis, we calculated the probability of bonding for each possible combination of a unique reaction site on the TCP molecule and a surface atom. The result is reported in Figure 3.4, where only reactions with a probability above 3% at any temperature are shown. The statistically significant reaction pairs were Fe–C1, Fe–C4, Fe–C5, Fe–C6, Fe–C7, Fe–O1, Fe–O2 and O–P. Again, bonds with H atoms were excluded from the analysis. Snapshots of representative model systems illustrating the statistically significant reactions are shown in Figure 3.5, confirms that most probable reactions at lower temperatures involved chemical bonding between the C5 or C6 atom in the TCP and Fe on the iron oxide surface. These reactions were observed for whole TCP molecules, i.e. without decomposition. However, at the high temperatures, reactions between O1 and C1 in the TCP and Fe on the surface became dominant. At these temperatures, chemisorption reactions were accompanied by TCP decomposition. The most commonly observed reaction at high temperatures was decomposition of TCP via breaking of the O1–C1 bond followed by chemisorption of cresyl

via an O1–Fe bond. This was also sometimes followed by C1–Fe bonding, explaining the consistent trends exhibited by O1–Fe and C1–Fe observed in Figure 3.4.

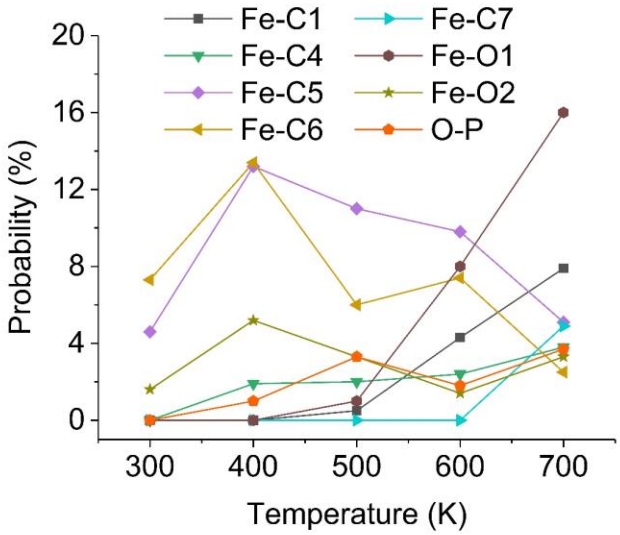


Figure 3.4 Probability of bonding between unique reaction sites on the TCP and atoms on the iron oxide surface as a function of temperature. Only atom–atom pairs for which the probability of bonding was 3% or more at any temperature are shown.

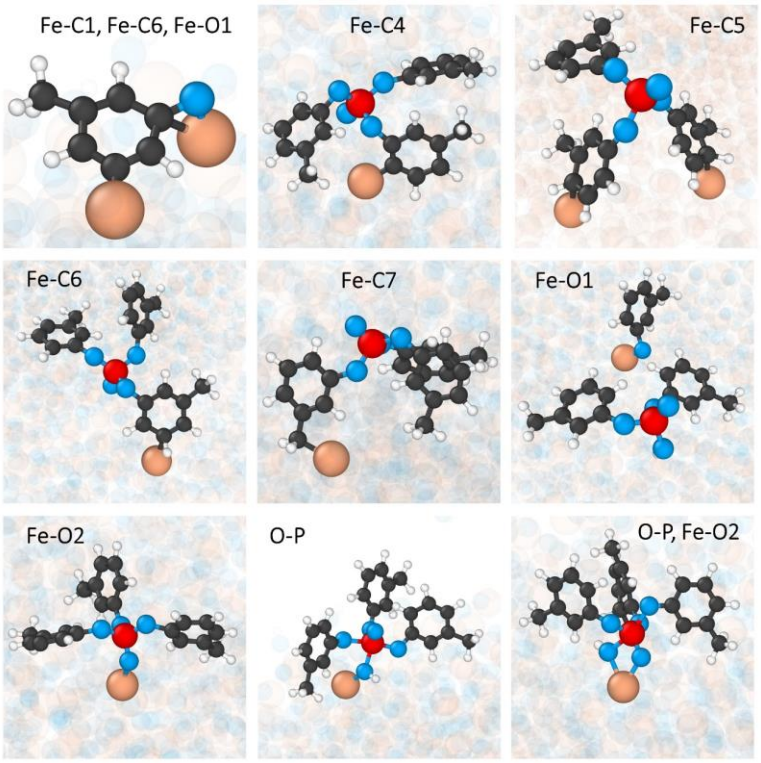


Figure 3.5 Snapshots of the simulation illustrating the statistically significant TCP– surface interactions. All atoms are faded except those in the TCP and surface involved in a given reaction.

Previous DFT studies analyzed reaction pathways for TCP on an iron (110) surface and showed that multiple pathways were possible.[73] However, all of those pathways started with bonding between O2 and Fe. The dynamic simulations shown here suggest that, while Fe–O2 bonding can occur on an amorphous iron oxide surface, it is not statistically significant compared to Fe–C or Fe–O1. This highlights the differences between reactions on ideal crystalline metal surfaces compared to those on an amorphous, passivated oxide.

The chemical reactions described above are the starting point for film formation. Therefore, the composition of the material chemisorbed to the surface in the simulations can be analyzed in the context of previous experimental measurements; specifically, experiments performed in oxygen-deficient environments, where the iron was expected to have a native oxide, but only small amounts of outside reactants (e.g. water, oxygen, hydrogen) were available to contribute to the TCP-surface reactions.[157-160] In the simulations, the composition of the material chemisorbed to the surface was quantified in terms of surface density of individual elements that originated from TCP molecules. Figure 3.6 shows that the chemisorbed material consisted of C, O and P atoms. The density of the individual elements was greatest at 400 K and, at all temperatures, C had the highest density.

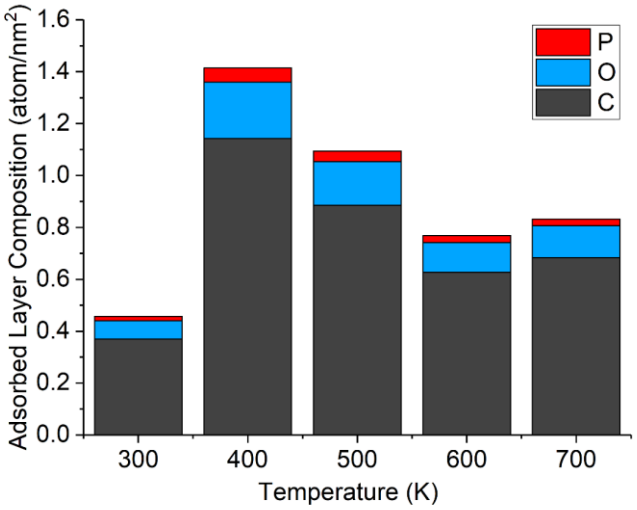


Figure 3.6 Chemical composition of adsorbed layer on the amorphous iron oxide surface at different temperatures.

Although direct comparisons between simulations and experiments cannot be made since the models capture just the initial stage of film formation, parallels can be drawn between the composition of chemisorbed species in these simulations and the composition of TCP film measured in previous oxygen-deficient experimental studies. First, the significant amount of C observed in the simulations is consistent with experimental measurements of the composition of TCP film near the surface obtained using auger electron spectroscopy (AES) and x-ray photoelectron spectroscopy (XPS).[157, 158] Further, analysis of the species chemisorbed to the surface in the simulations showed that, at lower temperatures, most chemisorbed species were complete TCP molecules, but as the temperature increased, bonds broke within the TCP resulting in chemisorption of decomposition products, predominantly cresyl. This is consistent with the composition of reactant film obtained using Auger Electron Spectroscopy (AES) and X-ray Photoelectron Spectroscopy (XPS) on the surface of iron foils exposed to TCP at elevated temperatures in an oxygen-starved environment.[157-159] Our simulations suggest both occur, with the statistical likelihood of the latter increasing with temperature.

Most previous experimental studies have identified phosphorous as a key component of film formed from TCP on ferrous surfaces[153] and the working assumption has been that this iron phosphide or iron phosphate film results from the formation of Fe–P bonds directly from the TCP molecule.[73] However, our results show that P atoms are more often indirectly bonded[161] to the surface through TCP or other species that bond with the surface via C atoms. Also, phosphate groups are likely to be present on the surface through physisorption, following chemisorption of cresyl. Therefore, at least in oxygen deficient environments, the primary mechanisms by which P is initially incorporated into a film are indirect bonding (i.e. present in species bonded to the surface via other atoms) or physisorption enabled by decomposition of TCP. This hypothesis cannot be directly tested without further extensive experimentation and reactive MD simulations. However, many previous experiments analyzed TCP film formation in terms of the composition of desorbed

species, as opposed to adsorbed species as done here. Therefore, future research specifically analyzing reaction products that leave the surface would enable additional comparisons to experiment.

## 3.2. Synergistic effect of nanodiamonds on the adsorption of tri-cresyl phosphate on iron oxide surfaces

### 3.2.1. Introduction

Chemical reactions between liquid phase species and a solid surface are the precursors to growth of solid or semi-solid films in a variety of applications. Understanding the pathways for these reactions is therefore an important step towards optimization of film growth parameters [162, 163]. Here, we focus on reactions between tri-cresyl phosphate (TCP) and an amorphous iron oxide surface. This is an important system because TCP is a chemical additive that is included in lubricant formulations to minimize wear of moving components. TCP is widely used in lubricants in the aviation industry as well as some automotive engines [158]. In a mechanical system, TCP functions by chemically reacting with ferrous surfaces to form films that protect those surfaces from wear under harsh sliding conditions [73, 153].

Despite the success of TCP as a lubricant additive, it is associated with environment and health concerns that encourage the development of alternatives [164, 165]. However, emerging lubricant additives must, at least initially, be compatible with existing additives such as TCP. One family of emerging lubricant additives that has been the focus of many studies in recent years is nanoparticles [166]. Of particular interest for some applications are diamond nanoparticles, or nanodiamonds (NDs), which offer high thermal conductivity, high hardness, high melting point and the ability to withstand extreme environments [137]. ND additives have been shown to reduce friction and wear in both oil and water-based lubricated systems [137, 167-171]. However, the compatibility of NDs with existing lubricant additives, including TCP, is not yet fully understood.

Of particular concern is the fact that NDs have been reported to increase the activation energy for some processes [172], which could adversely affect TCP–surface reactions and in turn limit TCP film growth. However, recently, a quartz crystal microbalance (QCM) was used as an in situ tool [173] to measure reaction temperatures of TCP on ferrous surfaces [174]. These measurements showed that, contrary to expectation, the addition of NDs facilitated the formation of TCP films on air baked Fe surfaces [175]. The composition of the resultant film was also found to be affected by the NDs, with the presence of NDs increasing the amount of carbon and oxygen relative to the amount of iron in the film. These findings were extremely promising because they showed that NDs can have a synergistic effect on the formation of protective films in lubricated contacts [175]. However, the experimental approach did not provide a fundamental explanation for the observed benefit of NDs on TCP films. Therefore, here we use molecular dynamics simulations (MD) here to explore the interactions between TCP, NDs and amorphous iron oxide surfaces to explain the underlying physics.

### 3.2.2. Methods

Simulations were designed to capture chemical reactions between TCP molecules and

an amorphous iron oxide surface, with and without NDs, across the same range of temperatures reported in the previous QCM study. Two models were created, one with NDs and one without NDs, as shown in Figure 3.7. In both systems, the dimensions of simulation domain were 5 nm × 5 nm × 10 nm, with periodic boundaries in the plane of the surface and a fixed boundary in the surface–normal direction. A repulsive wall at the height of 9.8 nm was employed to prevent atoms from traveling out of the simulation box. Both models contained 32 TCP molecules, corresponding to approximately a monolayer, and one of the systems also contained 5 NDs. All interactions were described by the ReaxFF force field [80], which enabled the model to capture formation and breaking of covalent bonds, with a recently developed parameter set that captured all relevant atomic interactions [156]. In both systems, atoms in the bottom 0.3 nm of the iron oxide were fixed in place. Temperature was controlled using a Nosé-Hoover thermostat with a damping parameter of 25 fs applied to all unconstrained atoms. Simulations were run using LAMMPS [130] with a time step of 0.25 fs.

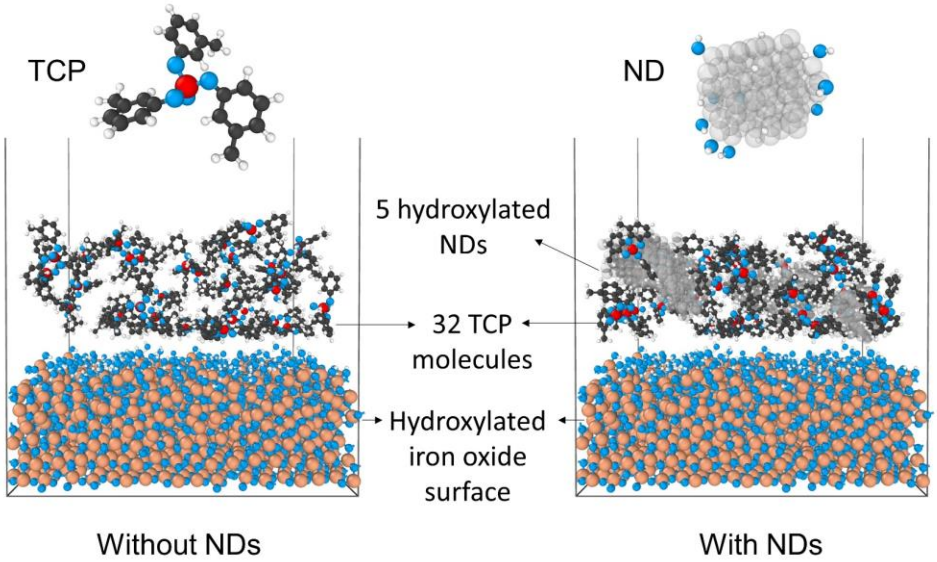


Figure 3.7 Snapshots of the simulations consisting of TCP molecules on an amorphous iron oxide surface, with and without NDs. Close-up views of the TCP and ND are shown as insets above the simulation snapshots. Colors represent: Hydrogen - white, Oxygen – blue, Phosphorous - red, carbon in TCP - black, carbon in NDs - faded grey.

The amorphous iron oxide was created by annealing a slab of crystalline Fe2O3 iron oxide (5 nm × 5 nm in the plane of the surface and 1.7 nm thick). Annealing was performed by increasing the temperature from 300 to 4000 K over 25 ps, holding at 4000 K for 125 ps, and then decreasing back to 300 K over 500 ps [156]. The surface was then passivated by introducing water molecules into the model. A simulation with the amorphous iron oxide surface and water was run at 700 K for 500 ps, after which the number of chemical bonds was constant. After the simulation, any water molecules not covalently bonded to the surface were removed from the model. The hydroxyl group density on the final surface was 8.31 nm−2, consistent with the range of 5 to 9 nm−2 reported in previous studies [176]. The resultant passivated amorphous iron oxide model was comparable to the surface of the sample used in previous experimental measurements of a pure iron film baked in air at 513

K for two hours [175].

The ND particles were created by cutting from a block of carbon atoms in a diamond structure such that the surfaces of the cut material had the minimum energy [177]. The resultant particles had a diameter of approximately 1 nm. The NDs were passivated by placing them in a simulation with water molecules at 500 K for 500 ps. During the hydroxylation process, water molecules reacted with the ND surface leading to the formation of CH and COH chemical groups. The observation of hydrogen and hydroxyl terminated carbon atoms on the surface of NDs has been reported in previous studies [178]. In the QCM experiments, the NDs had a diameter of 30 nm and, in an oil dispersion, were prepared in a manner that is expected to result in COOH termination. The presence of COOH groups is expected based on previous experimental observations [179] as this chemistry has been shown to improve dispersion by promoting electrostatic attraction with the anchoring groups of the dispersants [167]. Thus, our model NDs were several times smaller than those in the experiment and likely had different termination. The size scale was limited by the simulation method and the termination was determined by the force field through the simulation of the NDs with water. Despite these differences, the model NDs were a reasonable approximation since all of the reactions that we observed were between the un-terminated C atoms in the NDs and either O from the TCP or Fe on the surface.

Both models were initially equilibrated at room temperature for 0.25 ns. Then, the temperature was increased linearly at a rate of 1000 K/ns to a maximum temperature of 550 K. This is the same temperature range as reported in the previous QCM experiments [175], although the heating rate was orders of magnitude faster than in the experiments due to the small time scale of the model. The simulation was repeated three times for each model to enable statistical analysis of results. For each replica, the TCP molecules were placed at different initial positions such that the simulations captured the potential interaction of TCP with many different reactive sites on the surface. Also, to confirm the heating rate did not affect results, simulations were repeated once more at a rate of 500 K/ns. During the simulation, the number and type of covalent bonds between TCP and the iron oxide surface were recorded.

### 3.2.3. Results and Discussion

Figure 3.8 shows the number of bonds between TCP molecules and the iron oxide surface, with and without NDs present. At all temperatures, the chemical bonds that formed were between C atoms in the TCP and either Fe or O atoms on the surface. Two key observations can be made from these results. First, there were more chemical bonds formed between TCP and the surface when the NDs were present. This is consistent with the observation from QCM experiments on air baked Fe which showed an abrupt frequency shift (indicating film growth) only for the system with NDs [175]. Second, the increase in bonding with NDs observed in Figure 3.8 occurred between 400 and 470 K. This is similar to the temperature of the abrupt frequency shift in the QCM experiments which occurred at 500 K [175]. Further, the frequency shift observed at a single temperature on the experimental time scale is captured by the orders-of-magnitude faster simulations as an increase in bonding over a range of temperatures, potentially explaining why the shift is so abrupt in the experiments. These same trends were observed in our simulations at the slower temperature ramp rate of 500 K/ns.

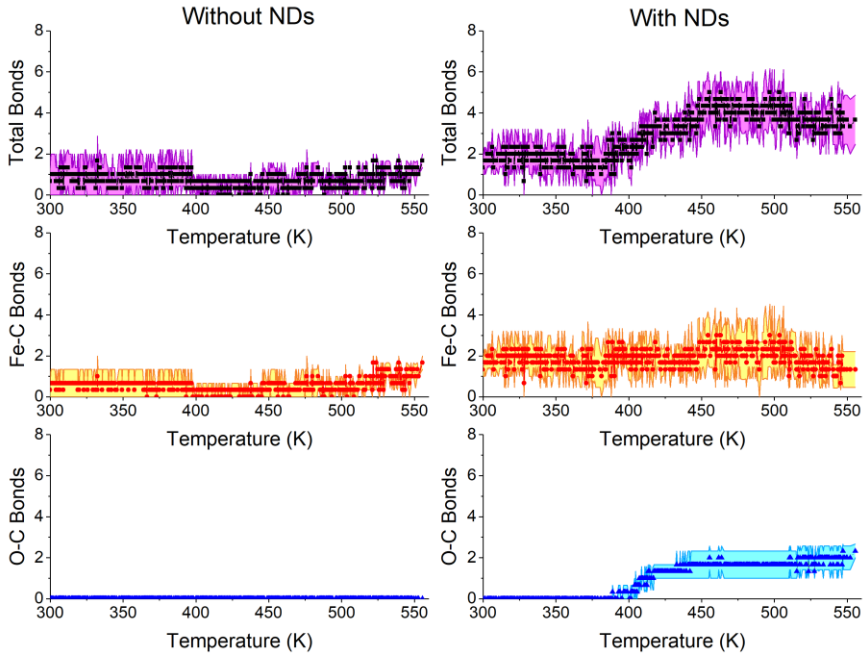


Figure 3.8 Number of covalent bonds formed between TCP and the iron oxide surface as a function of temperature without (left) and with (right) NDs as a function of temperature. The top figures show the total number of bonds and the middle and bottom figures show the total number of bonds and the middle and bottom figures show the number of Fe–C and O–C bonds, respectively. The symbols are the average and the lines/shading represent the standard error of the three independent simulations.

To better understand the elementary steps leading to TCP film formation in the presence of NDs, we analyzed individual chemical bonds formed during the simulation. The unique bonding sites on the TCP are differentiated and identified in the upper panel of Figure 3.9. We observed that most of the direct TCP–surface bonds were formed between the C5 or the C6 of the TCP and Fe on the surface. Representative snapshots of these bonds are shown in the middle panel of Figure 3.9. We also observed direct chemical bonding between the ND and the surface via Fe–CND bonds. This is consistent with experimental detection of NDs embedded in the film grown in QCM as shown in the insets to Figure 3.10. Finally, the simulations showed bonding between C atoms in the NDs and the double-bonded O atom in the TCP. In many cases the NDs to which the TCP molecules bonded were themselves bonded to the surface. Therefore, the NDs provide a means of indirectly bonding the TCP to the surface. This observation suggests that the NDs contribute to film formation by enabling indirect bonding between the TCP and surface.

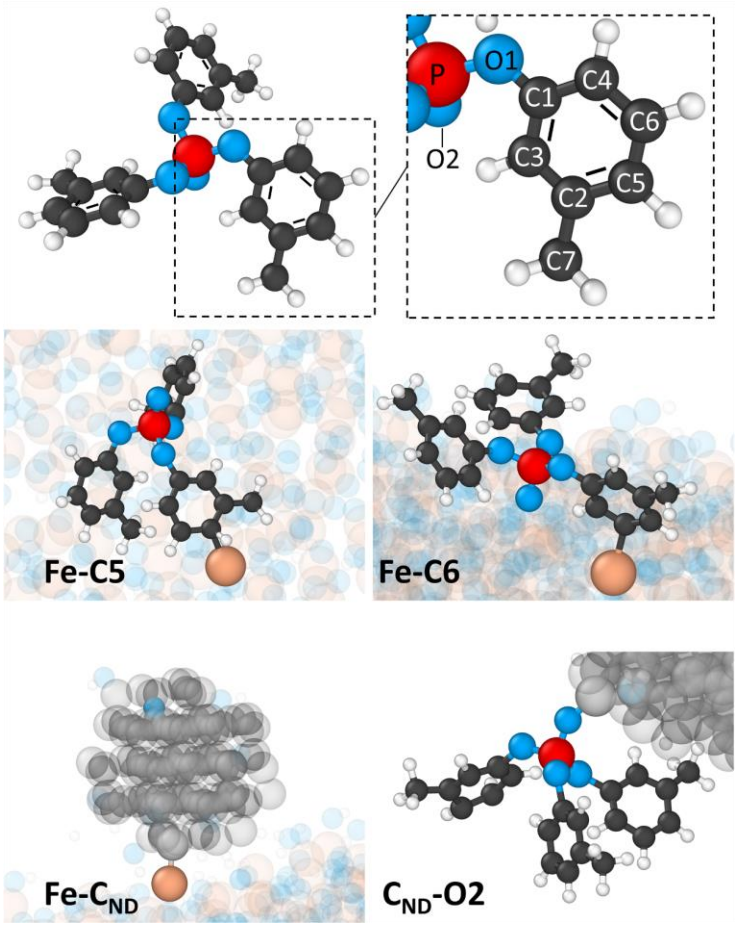


Figure 3.9 Snapshots from simulations illustrating the most commonly observed reactions between TCP, the iron oxide surface and the NDs. All atoms are faded except those involved in a given reaction. The unique reaction sites on the TCP are labeled in the upper panel.

We next analyzed the composition of the film forming on the surface through these reactions at 490 K, a temperature near which bonding was observed in the simulations and the frequency shift was measured in the experiments. From the simulations, we calculated the surface density of each type of atom that was either directly or indirectly bonded to the surface. An example of an indirectly bonded atom is an atom in a TCP molecule chemically bonded to an ND that is chemically bonded to the surface. Figure 3.10 shows that the densities of all atom types (C, O and P) were dramatically larger in the system with NDs. These results are consistent with the film composition reported from the experimental study obtained using electron dispersive X-ray spectroscopy (EDS) [175]. In the experiments, the molar composition of the film without NDs was 9.8 for C, 7.6 for O and 0.02 for P; with the NDs it was 20.0 for C, 18.0 for O and 0.3 for P. The same trend is observed in Figure 3.10 where the density of all elements is greater with the NDs present, and the relative amount of each element increases as P < O < C both with and without NDs. The ratio of C to O is higher in experiments than in simulations, which is attributable to the fact that the experimental measurement captured both the film and substrate on which it formed, while

the simulation calculation included only atoms from the TCP and NDs. The compositions of all three elements increased in the presence of the NDs, both in experiments and simulations. In the simulations, it was found that that the increase was due to both NDs directly bonded to the surface, as well as TCP molecules and NDs indirectly bonded to the surface (Figure 3.10). This effect is particularly relevant for P, which is an important constituent of the film in terms of reducing wear in moving components. Here, we show that indirectly bonded TCP molecules contribute significantly to the increased amount of P in the film with NDs. These results suggest that one mechanism by which the NDs facilitate film formation is the ability to indirectly bond the TCP to the surface.

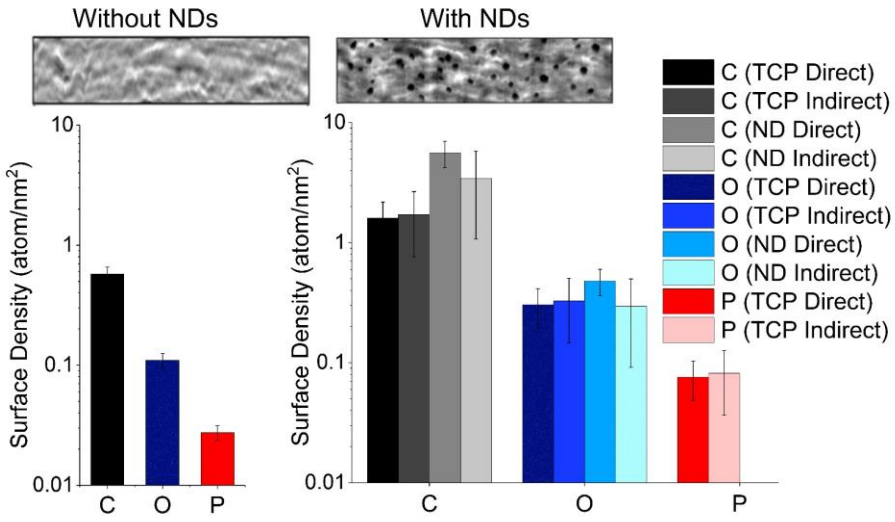


Figure 3.10 Simulation surface density of carbon, oxygen and phosphorous in the film at 490 K, quantified by the number of atoms in the TCP or NDs that are directly or indirectly bonded to the surface. Inset are 300 nm × 1500 nm atomic force microscope topography images (height scale is approximately 36 nm dark to light) of the film grown in QCM experiments; adapted from the graphical abstract of Ref. [175]

### 3.2.4. Conclusion

In the first part of this chapter (3.1), we used parallel reactive molecular dynamics simulations of TCP on an amorphous iron oxide surface to explore the initial steps leading to formation of a protective film on lubricated ferrous surfaces. Many reaction pathways are possible for TCP on iron oxide because of the multiple reaction sites on the TCP and irregularity of the amorphous surface. To capture as many of these pathways as possible in an MD simulation, we ran 100 parallel replicas of a model system consisting of one TCP at random initial locations above the surface. The simulations were run at temperatures ranging from 300 to 700 K and results were analyzed at each temperature to determine the statistical likelihood of the possible reactions. It was found that the relative reactivity of the unique reaction sites on the TCP was temperature dependent. Specifically, C atoms at the perimeter of the rings bonded most with the surface at lower temperatures and O atoms in the core of the TCP bonded most with the surface at higher temperatures. The

composition of the material chemisorbed to the surface was then analyzed which revealed that C is the most prevalent element at any temperature. Also, the most statistically likely chemisorbed species were found to be TCP or cresyl, with the former being more prevalent at lower temperatures and the latter more prevalent at higher temperatures. These trends were found to be consistent with observations from previous experimental measurements of TCP film grown on iron with a native oxide in oxygen-deficient environments.

In the second part of this study (3.2), we used reactive molecular dynamics simulation to investigate the origins of previously observed differences between TCP film formation on ferrous surfaces with and without NDs present. First, the simulations showed that NDs increased the number of bonds between TCP and iron oxide – this is consistent with the measurement of a frequency shift at 500 K in QCM experiments with NDs, indicating film formation. Second, analysis of individual chemical bonds in the simulation showed that TCP can bond with the surface both directly and indirectly. The direct bonding was shown to occur primarily between the C5 and C6 on the TCP and Fe on the surface. The indirect bonding of TCP molecules was shown to occur through the O atom on the TCP bonding with C on the ND, where that ND was bonded to the surface. Next, simulation results revealed a higher density of C, O and P directly or indirectly bonded to the surface in the presence of NDs, comparable to EDS measurements of a higher percent of those elements with NDs. The higher density of elements originally from the TCP is in part due to TCP molecules bonded to the surface via an ND.

Overall, this study has a few key outcomes. Firsts, the film illustrates that there are multiple reactions between TCP and amorphous iron oxide, and the statistical likelihood of these reactions will depend on temperature and introduced particles like NDs. Further, simulations results suggest that the presence of phosphorous in the film formed from TCP may be due to molecules that bond with the surface via carbon in the absence of nanoparticles and the formation of a network composed of NDs and TCPs adsorbed on their surface when NDs added to the system. These findings reveal that the NDs can facilitate film formation through their ability to bond TCP molecules indirectly to the surface. The statistical approach used to characterize reaction sites on TCP as it interacts and bonds with amorphous iron oxide may be applied to other systems where organic molecules react with surfaces. The approach is particularly useful for irregular or disordered surfaces present in a variety of applications and on which many possible reactions contribute to film formation.

## Chapter 4 : Chemical and Physical Contributions to the Friction at the Sliding Interfaces

Friction occurs through a complex set of processes that act together to resist relative motion. However, despite this complexity, friction is typically described using a simple phenomenological expression that relates normal and lateral forces via a coefficient, the friction coefficient. This one parameter encompasses multiple, sometimes competing, effects. To better understand the origins of friction, here we study a chemically and topographically well-defined interface between silica and graphite with a single graphene step edge. We identify the separate contributions of physical and chemical processes to friction and show that a single friction coefficient can be separated into two terms corresponding to these effects. The findings provide insight into the chemical and topographic origins of friction and suggest means of tuning surfaces by leveraging competing frictional processes.

### 4.1. Chemical and physical origins of friction on surfaces with atomic steps

#### 4.1.1. Introduction

Friction occurs at the interface between any two solid surfaces in contact and moving at different speeds or directions. Friction corresponds to wasted energy and therefore determines the efficiency and useful lifetime of all moving systems, from biological to aeronautical. At the macroscale, friction force (Ff) is often linearly proportional to the applied load (L). The proportionality constant of this relationship is called a friction coefficient (or coefficient of friction, COF, typically given the symbol $\mu$); thus, it can be expressed as $Ff = \mu \times L$, which is the well-known Amonton's law[180]. At the nanoscale, adhesive forces (Fa) become significant and an additional term is introduced, $Ff = \mu \times L + Fa$ [181]. Although this expression is phenomenologically simple and has been found to hold true in experiments for decades, the actual mechanisms determining the magnitude of the COF are very complicated. Friction has been proposed to have purely physical origins [182] as well as be related to chemical processes in sliding interfaces [183, 184]. However, the interplay of these two effects that ultimately results in observed friction is still poorly understood because often friction is associated with surface wear. In this study, we used a chemically and topographically well-defined interface without wear to identify the contributions of physical and chemical processes to friction and thereby obtain fundamental insights into the origin of the frequently reported but poorly understood COF.

#### 4.1.2. MD Simulations

To obtain molecular details at the atomic scale, the chemical and physical interactions between the atomically flat graphite surface with single-layer graphene step edge and the curved silica counter surface were modeled using molecular dynamics (MD) simulation with a ReaxFF reactive force [129, 185]. All the simulations were done using the large atomic/molecular massively parallel simulation (LAMMPS) software [130], and the post processing of results was carried out using the OVITO software [131].

The initial arrangement of the tip and the graphite is shown in Figure 4.1. The graphene step edge had an armchair structure [186]. As suggested by the experimental measurements,

the graphene edge in the simulation was terminated with hydroxyl groups and hydrogen atoms alternatively [187]. To maintain the temperature at around 300 K, the NVT (fixed number of particles, volume, and temperature) ensemble with a Langevin thermostat was applied to all atoms that were not fixed or rigid.
Considering that there is a native oxide layer on the Si tip and only the apex of the tip is in contact with the graphite surface, the amorphous silica structure was used as a model tip in the simulation. The amorphous silica was produced by melting crystalline cristobalite at 4000 K and then quenching to room temperature. To minimize the strain in the final amorphous structure, the heating and cooling rate was 0.02 K/fs, which was the slowest rate possible within the current computational constraints. Various properties of the amorphous silica model structure produced in this way were found to be comparable with experimentally measured properties [75]. To reduce computational cost, the tip was constructed in a semi-circular disc shape (Figure 4.1). The curvature (radius), thickness and height of the disc were 2.5 nm, 1.5 nm, and 1.5 nm, respectively. To passivate the silica surface contacting the graphene surface, the undercoordinated silica and oxygen atoms were terminated with hydrogen atoms. The atoms in the top 0.5 nm of the tip were treated as a rigid body. To decrease the computational cost, only two mobile graphene layers were modeled at either side of the step edge.

Each MD simulation consisted of four steps: (i) energy minimization and equilibration of the tip and the substrate far from each other; (ii) downward movement of the tip at a speed of 10 m/s until the distance between the lowest atom in tip was 0.2 nm from the top layer of the substrate; (iii) application of the normal load at the top rigid part of the tip and equilibration for 120 ps; (iv) sliding of the tip at 10 m/s in the X-direction through pulling by a harmonic spring with a stiffness of 6 N/m. MD simulations were performed for the step-up and step-down directions with loads of 5, 7.5, 10, 12.5, and 15 nN applied to the top rigid part of the tip. The real atomic area was calculated from the positions of atoms in the contact at each load [188], corresponding to pressure between ~2.1 GPa at 5 nN and ~4.8 GPa at 15 nN. During the tip sliding process, the side boundaries of the graphite substrate were constrained to be fixed in all directions. The friction force during sliding was calculated from the sum of the X-component of the forces on the atoms in the tip. Due to highly noisy force diagrams, a Fourier transform filtering was applied.

The shear strain of the silica tip along the sliding direction was quantified from the change in position of atoms relative to their neighboring atoms within a 0.5 nm cutoff distance. The cutoff radius controls the number of neighbors that are included in the calculation of the deformation gradient tensor for each atom. This radius must be large enough to include at least three non-coplanar neighbors for every atom. The larger the cutoff, the large the volume over which the local deformation gradient tensor is calculated [189, 190]. Here the minimum cutoff radius (0.5 nm) was chosen to facilitate monitoring of the changes in the shear strain value.

The number of hydrogen bonds was calculated from the positions of donator oxygens, acceptor oxygens, and the hydrogen atoms using the logic proposed by Guardia et al. [191]. This calculation was performed considering both for OH groups on the tip and the acceptor oxygen on the edge and vice versa.

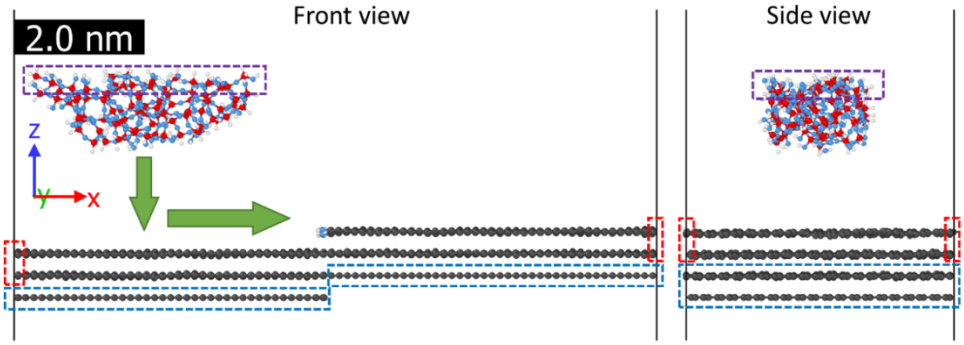


Figure 4.1 Front and side views of the MD simulation box. The box has periodic boundary conditions in the X and Y directions. The dashed boxes indicate regions in which atoms are treated as a rigid body (purple) or fixed in place (red and blue). The green arrows show the path of tip displacement during loading (downward movement) and sliding (lateral movement).

### 4.1.3. Results

Figure 4.2 schematically depicts the model system used in this study, which consists of an atomic force microscopy (AFM) probe and a graphite surface with a single-layer graphene step edge. The basal plane of graphite provides a chemically inert and defect-free flat surface. Since the graphene sheet exposed at the top surface is commensurate with the underlying layer (i.e., all topmost atoms are in registry with the underlying atoms), it provides the topographically least corrugated surface for friction tests [192]. The single-layer graphene step edge that can be found on the graphite surface provides a well-defined topographic corrugation with a height change of precisely 0.34 nm over a distance corresponding to one chemical bond length [193]. The carbon atoms at the graphene step edge are terminated with hydroxyl (C-OH) and alkyl (C-H) groups (Figure 4.2). The AFM probe made of silicon is covered with a native oxide; thus, it is hereafter referred to as a silica tip. This same system is modeled using reactive molecular dynamics (MD) simulation of the apex of the silica tip and the topmost three layers of graphene in the graphite near the step edge (Figure 4.1). Thus, it allows both experimental and computational studies of the interfacial shear of a silica surface on both an atomically-flat surface and a chemically and topographically well-defined feature at the step. Upon confirmation of agreement between the experimental and computational friction responses, the simulations provide insight into the atomic-level origins of the friction.

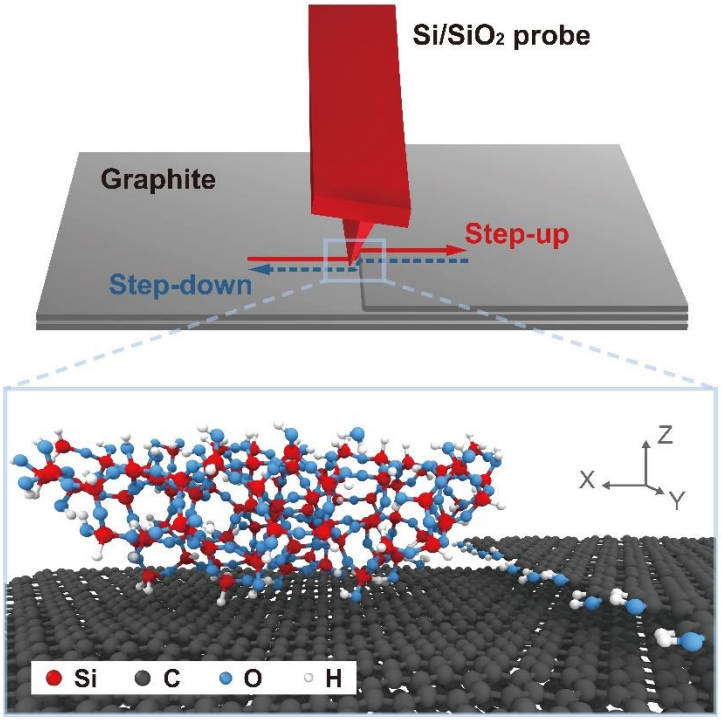


Figure 4.2 Schematic illustration and atomic-scale rendering of a silica AFM tip sliding up and down a single layer graphene step edge on an atomically flat graphite surface. The silica tip model represents the native oxide at the apex of the Si AFM tip used in the experimental study. This model system enables both experimental and computational studies that isolate the chemical and physical origins of friction.

Figure 4.3 shows the lateral force and height profiles measured from the AFM tip sliding over the graphite basal plane and moving up and down the graphene step edge at an applied load of 36.7 nN in dry nitrogen. Both sides of the graphene step edges are the basal plane of the graphite crystal, where the friction force (half the difference between the trace and re-trace lateral forces) is only 0.15 ± 0.03 nN on both the upper and lower terraces. If this friction force is divided by the sum of the adhesion force (9.4 ± 0.8 nN) and the applied load (36.7 nN), it corresponds to a COF of 0.003. This value is consistent with the super-lubricity reported for other types of carbon surfaces [194, 195]. However, when the AFM tip climbs up the step from the lower terrace to the upper terrace, friction increases by 30-40 times (positive lateral force in the step-up direction), giving a COF of about 0.1. This value is close to COFs observed for boundary lubrications by organic molecules on various surfaces under elastic deformation regimes [196]. In contrast, more complicated friction responses are observed when the AFM tip slides down from the upper terrace to the lower terrace. Note that when the sliding direction is reversed, friction corresponds to a negative lateral force. During the step down, friction first increases (negative lateral force), then decreases (change to positive lateral force) during the topographic height change, then increases again, and finally reaches the basal plane value as the tip moves away from the step edge.

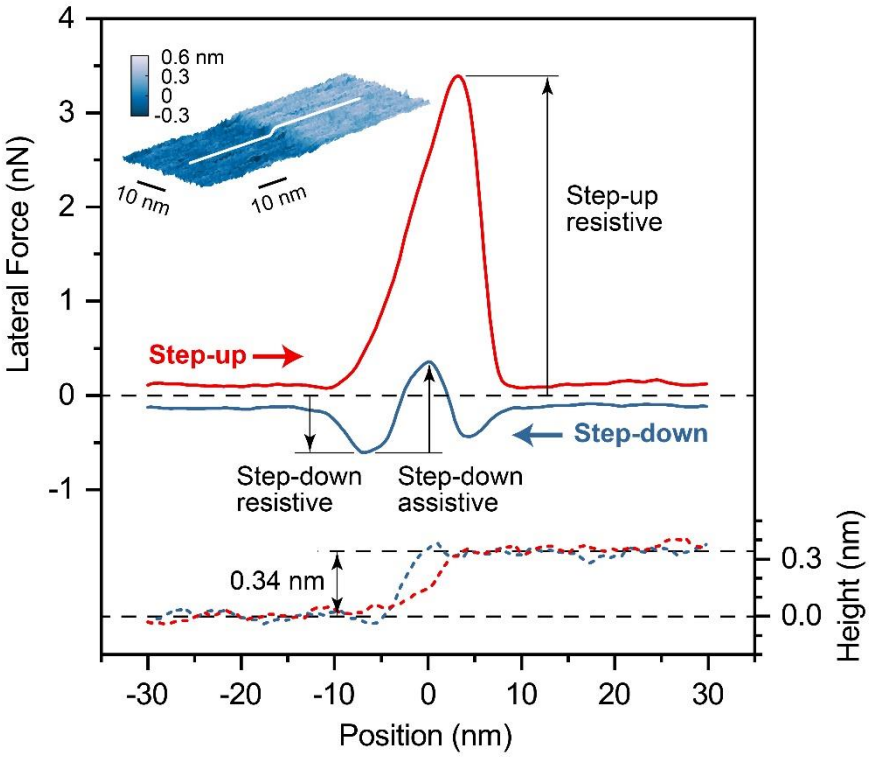


Figure 4.3 Lateral force (solid lines) and height profile (dashed lines) measured at the graphene step edge with a silica AFM tip. The normal force applied to the tip was 36.7 nN and the sliding speed was 500 nm/s. In the step-up direction, the positive lateral force means the graphene step edge is resisting tip sliding. In the step-down direction, the negative lateral force is resistive to the tip sliding and the positive (or upward deviation from the negative trend) force is assistive to the tip sliding. The inset is the AFM topographic image of the graphene step edge obtained after repeated friction measurements at applied normal forces varying from 7.3 nN to 36.7 nN (Figure 4.9 (a)); the post-scan image shows no damage of the friction-tested region (white line). The height of the step edge is 0.34 nm, corresponding to the sum of the thickness of one graphene layer and the interlayer spacing between adjacent graphene layers.

The changes in friction observed at the step edge (Figure 4.3) cannot be explained by topography alone. If the topographic effect was dominant, then the trace and re-trace hysteresis at the step edge should be the same as that on the basal plane and its center is shifted from the zero line. In the literature, the large friction (resistive force) during the step-down motion over various atomic steps has been explained in the context of a simple Prandtl-Tomlinson model with an additional potential barrier at the step edge called an Ehrlich–Schwoebel barrier [197, 198]. The concept of the Ehrlich-Schwoebel barrier was adapted from the diffusion barrier for atomic movements at a surface encountered in film growth studies [199]. Although this phenomenological model can reproduce experimentally-observed friction behavior, it does not provide molecular or atomistic insights into the origin of the Ehrlich-Schwoebel barrier. Previous modeling studies reproduced this barrier and demonstrated its ability to describe step edge friction, but the models did not explicitly

include chemical reactions [197, 198], so chemical and physical effects could not be differentiated. Here, to explore these origins, friction trends at the key points along the friction trace were analyzed as a function of load.

The experimentally observed trend was not a strong function of sliding speed and MD simulations performed at half the sliding speed exhibited the same trends (Figure 4.4). The load dependence of friction on the graphite terrace and at the graphene step edge, from both experiment and simulation, is shown in Figure 4.5. The qualitative trends from experiment and computation agree, despite differing size and time scale. This confirms that the simulations can provide atomistic insights into the interfacial processes responsible for complex friction behaviors at the single-layer graphene step edge as well as the super-lubricity on the graphene basal plane.

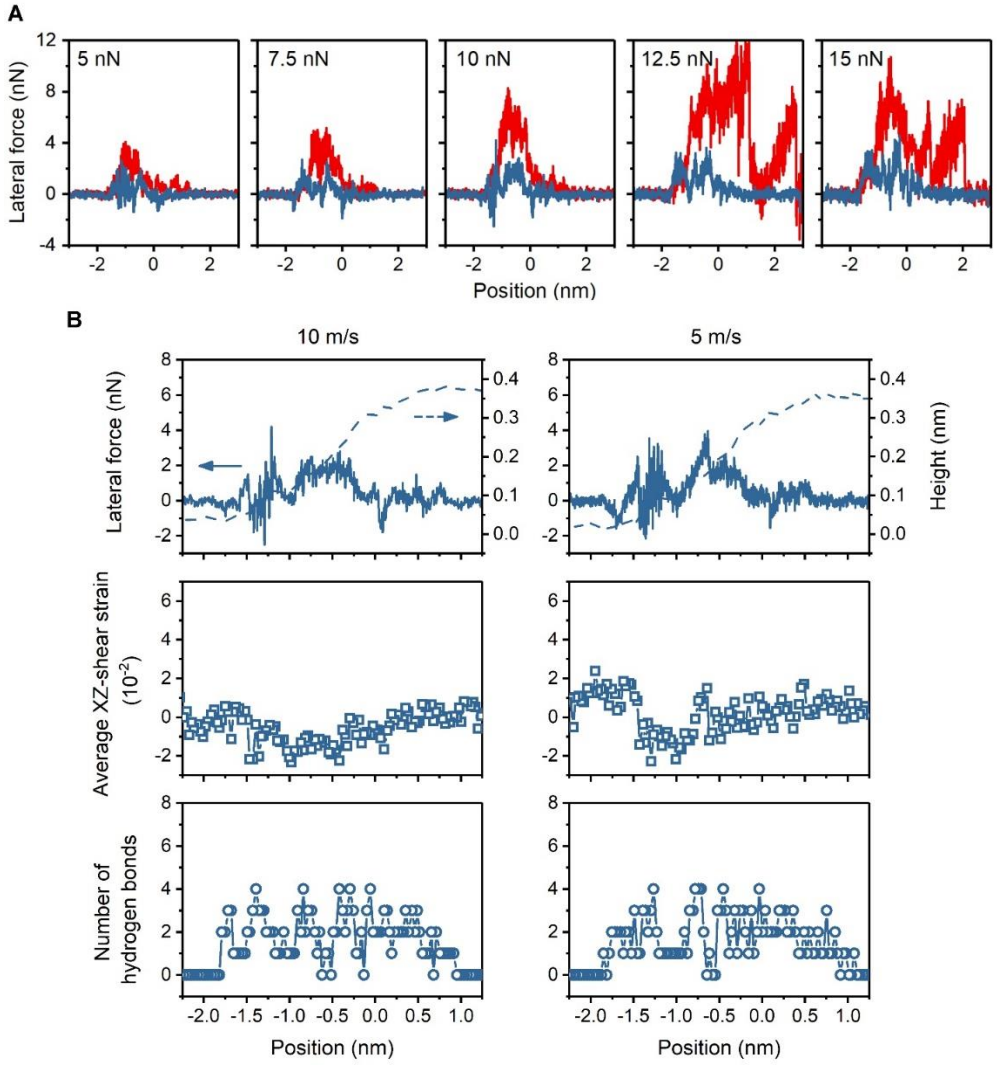


Figure 4.4 MD simulations of a tip sliding across a graphene step edge. (A) Lateral force under different applied normal loads. The sliding speed was 10 m/s. (B) Lateral force, shear strain of the tip and the number of hydrogen bonds between the tip and the graphene step edge obtained at sliding speeds of 10 m/s (left) and 5 m/s (right).

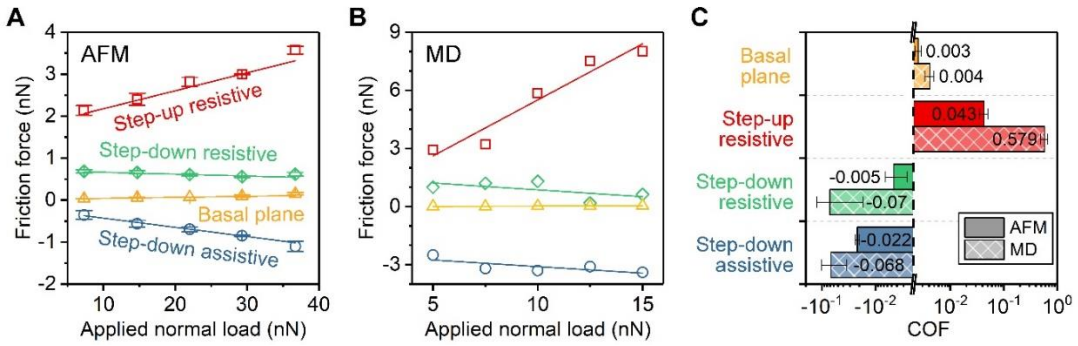


Figure 4.5 Load dependence of friction force and corresponding COF. (A) Friction force measured with the silica AFM tip under various applied normal load. The step-up resistive, step-down resistive, and step-down assistive forces are determined as marked in Figure 4.3. The mean and standard deviation were calculated from values of multiple measurements, where each measurement involved averaging over 128 scans. The standard deviations of the experimental values are similar to or smaller than the size of symbols. (B) Friction force calculated from reactive MD simulations. Note that, for the step-down case, a positive assistive lateral force corresponds to a negative friction force. (C) COF calculated from the load dependence of friction force, which is the slope of the least squares fitting lines in (A) and (B). The error bar in (C) indicates the uncertainty in the calculated slope. Since friction force for the cases of step-down resistive and step-down assistive decreases as the applied load increases, negative COF is obtained. The experimental results presented here were performed by Dr. Zhe Chen and Dr. Seong H. Kim group at Penn State University. [200]

The rate of change of friction with load at different positions along the friction trace is used to quantify COFs (Figure 4.5), with the goal of isolating the chemical and physical contributions. The COF on the basal plane is in the super-lubricity regime [201, 202]. However, during step-up, the COF increases by orders of magnitude. The step-down behavior is more complicated, as it consists of both assistive and resistive forces. The resistive force (positive friction) decreases slightly with load, corresponding to a small negative COF [203]. Lastly, the assistive force (negative friction) during step-down becomes larger in magnitude with increasing load, corresponding to a moderate negative COF. All of these measurements of friction are for the same materials sliding under the same operating conditions, the fact that there are drastic differences in the COF, including a change in sign, depending on the relative position of the tip with respect to the step, so these results could be used to identify different factors that contribute to friction. The atomic-scale information in the simulations is used to explore this.

Figure 4.6 shows the lateral force calculated from MD simulations at a load of 10 nN, along with the topographic height change (Figure 4.6 (a) and Figure 4.6 (b)). The shear strain of the silica tip is used to quantify physical contributions to friction (Figure 4.6 (c) and Figure 4.6 (d)) and chemical contributions are quantified by the number of hydrogen bonds formed between silica and graphene (Figure 4.6 (e) and Figure 4.6 (f)). Gradual changes in the out-of-plane fluctuation amplitude of the carbon atoms on the upper and lower terraces (Figure 4.7) suggest that the tip sliding over the graphene step edge is a

smooth process. When the silica tip is on the basal plane of graphite, there is no change in strain and no hydrogen bonding interaction across the interface. This is consistent with the expectation that the interlocking between atoms across the interface is negligible because the amorphous silica structure and the two-dimensional hexagonal array structure of graphite are incommensurate [204], there is no buckling of the surface because the topmost graphene layer is in registry with the underlayer [205], and the basal plane of graphite is chemically inert [206, 207]. There are no significant physical or chemical interactions causing friction, which explains the super-lubricity (COF of ~0.003) observed for the silica tip sliding on the graphite basal plane.

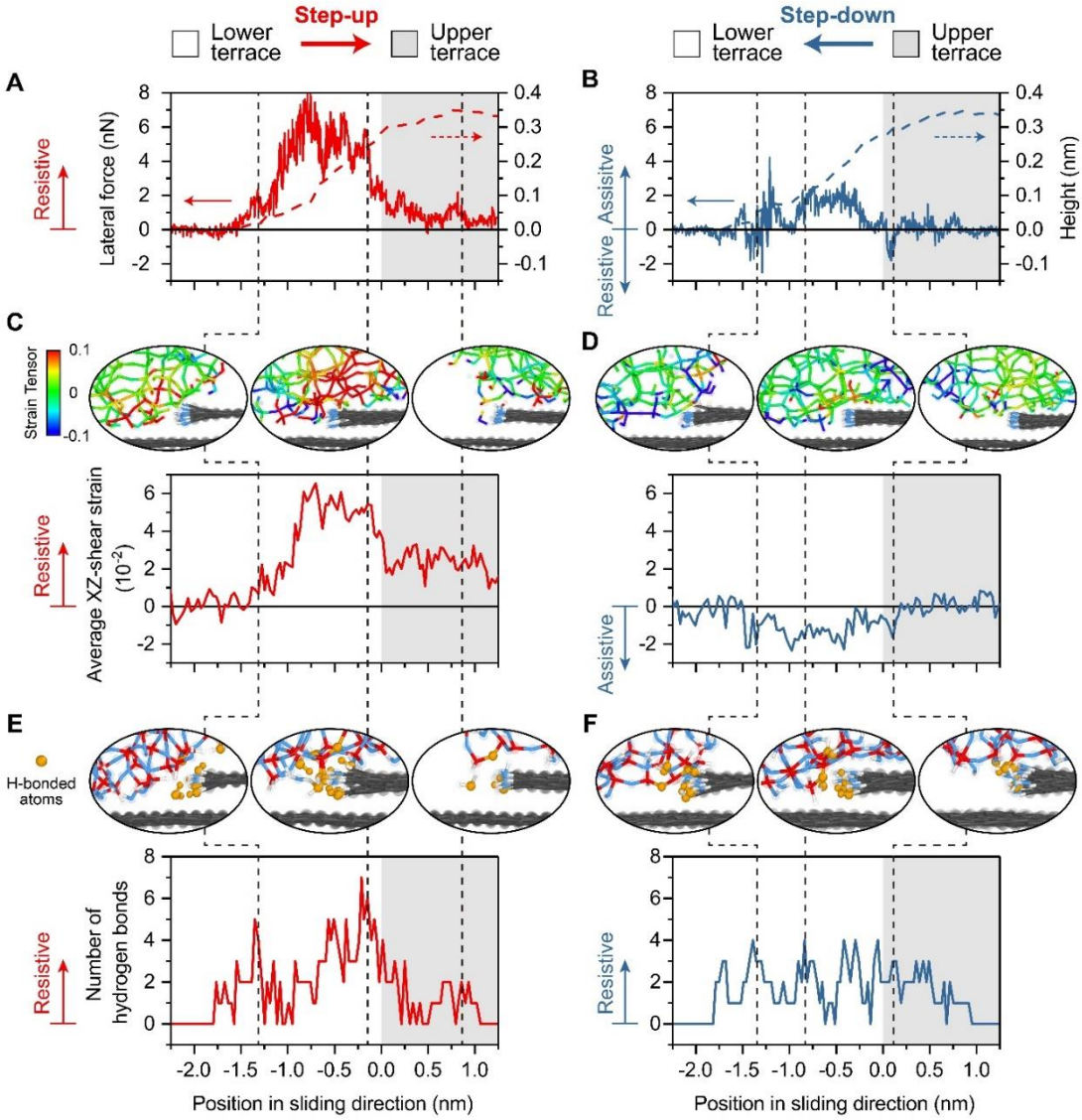


Figure 4.6 Reactive MD simulation showing the origins of chemical and physical effects on friction. (A,B) Lateral force, (C,D) shear strain of atoms in the silica where the sign indicates direction relative to sliding, and (E,F) number of hydrogen bonds formed between the graphene step edge and the silica, calculated from simulations as a function of center-of-mass position of the tip with respect to the graphene step edge for (A,C,E) step-up and

(B,D,F) step-down. The normal load applied to the silica tip is 10 nN and the sliding speed is 10 m/s. The topographic height change measured with the center of mass of the counter surface is shown with dashed lines in (A) and (B) on the secondary y-axis. The white and grey background areas are the lower and upper terraces, respectively. Also shown are the snapshots of the shear strain of atoms in the silica and the hydrogen bonds bridging two surfaces at three locations for both step-up and step-down.

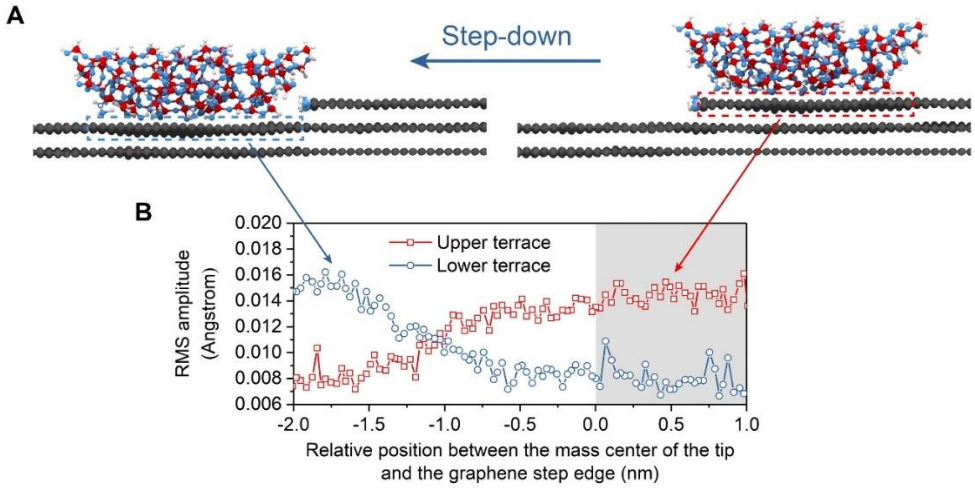


Figure 4.7 Out-of-plane fluctuations of carbon atoms on the upper and lower terraces. (A) Snapshots before and after the tip slides downward the graphene step edge. The blue dash-box indicates the lower-terrace carbon atoms involved in computation. The red and blue dash-boxes show the upper- and lower-terrace carbon atoms, respectively, involved in computations. (B) RMS amplitude of the out-of-plane fluctuations of carbon atoms on the upper and lower terraces while the tip slides from the upper terrace to the lower one at a normal load of 10 nN.

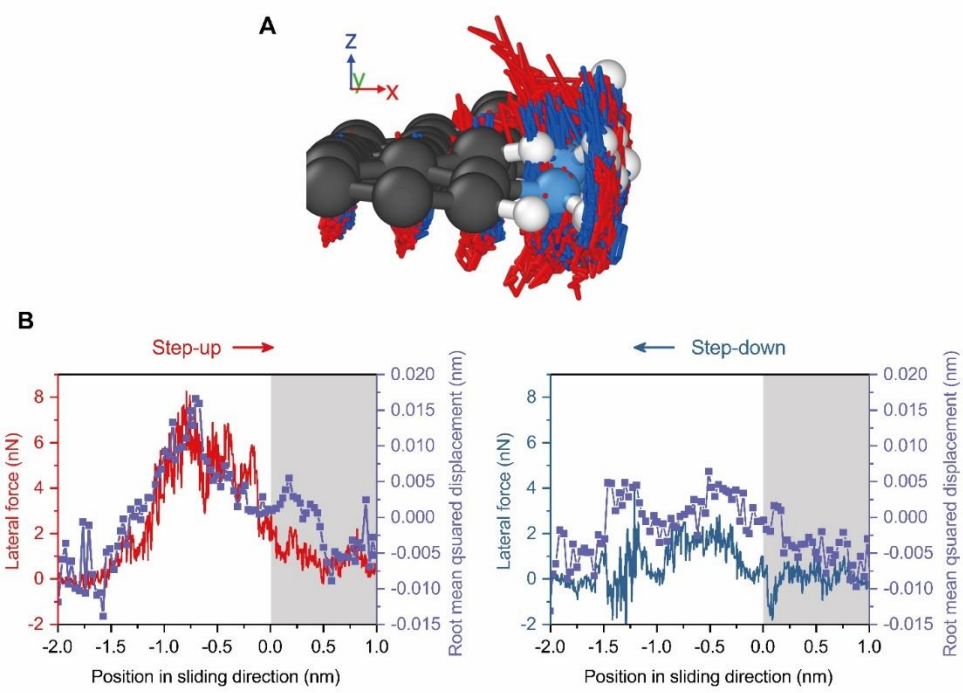


Figure 4.8 Out-of-plane deformation of C-OH groups terminating the graphene step edge. (A) Trajectory lines of C-OH groups at the graphene step edge during the step-up (red lines) than step-down (blue lines) processes due to hydrogen bonding interactions with the hydroxylated silica counter-surface. (B) Comparison between the lateral force and the deformation of the graphene step edge as a function of the center of mass of the tip from the simulations during the processes of step-up and step-down. The white and grey background areas are the lower and upper terraces, respectively.

As the silica tip steps up over the graphene edge, the shear strain of the atoms in the tip increases in the direction opposite of the sliding motion (Figure 4.6 (c)). The degree of shear strain is the largest just before the center-of-mass of the tip moves to the upper terrace. In addition, the hydrogen bonding interactions between the silica tip and the C-OH groups at the graphene edge increase during the step-up (Figure 4.6 (e)), accompanied by the out-of-plane deformation of C-OH groups terminating the step edge (Figure 4.8). So, at step-up, the physical (strain) and chemical (hydrogen bonding) mechanisms synergistically enhance resistance to sliding, leading to a COF more than 100 times larger than on the basal plane of graphite.

When the silica tip moves down the step from the upper terrace to the lower terrace, there is a small contribution from strain to assist sliding (the sign in Figure 4.6 (d) is opposite to the strain during step-up, Figure 4.6 (c)). However, hydrogen bonding between OH functional groups at the silica tip surface and the graphene step edge exerts a resistive force (Figure 4.6 (f)). This may also provide a physical explanation for the Ehrlich-Schwoebel barrier concept introduced previously to explain the resistive force at step-down. During sliding, physical and chemical mechanisms compete against each other; depending on their relative magnitudes, friction could be positive (resistive) or negative (assistive) as the tip moves down the step (Figure 4.9). The assistive effect due to shear strain is the largest when

the center-of-mass of tip transits from the upper terrace to the lower terrace, while the resistive effect due to hydrogen bonding interactions starts as soon as the leading edge of the tip approaches the graphene step edge and lasts until the trailing edge of the tip is separated from the graphene step edge. For this reason, the step-down resistive force due to hydrogen bonding interactions is observed over a large range around the step edge and the step-down assistive force from topography is seen only within the very narrow region near the step edge (Figure 4.3).

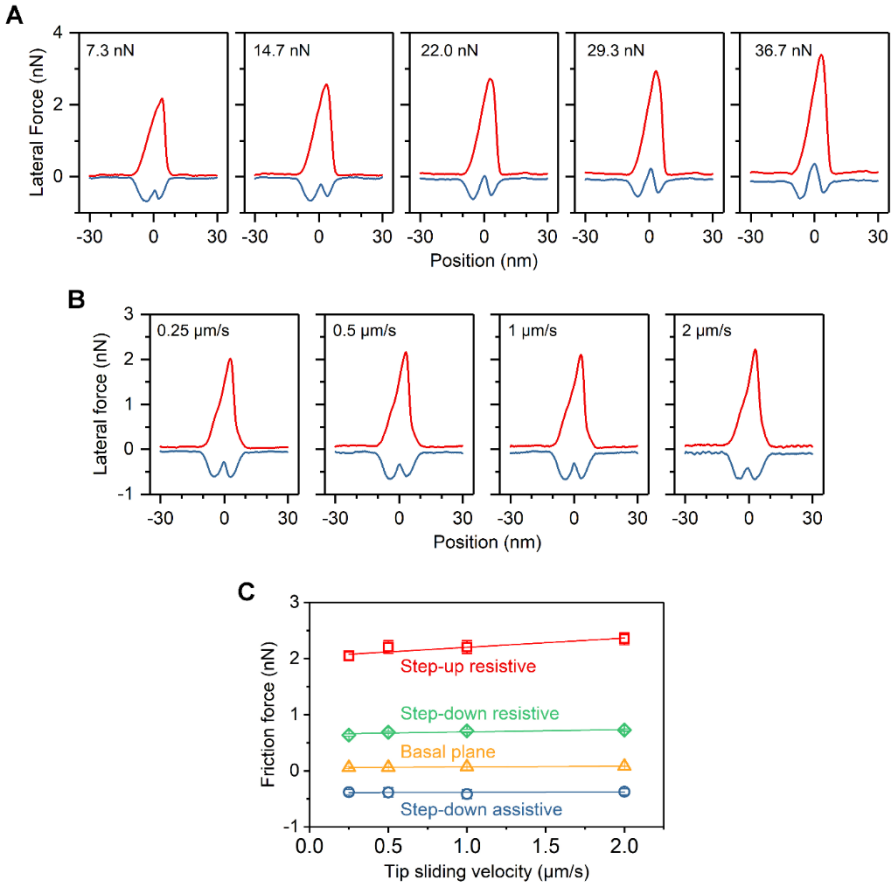


Figure 4.9 Lateral force of an AFM tip sliding across the graphene step edge. (a) Lateral force under various applied normal load. The sliding speed was 500 nm/s. (b) Lateral force at various sliding speeds. The applied load was 7.3 nN. (c) Friction force of each component at the graphene step edge at different sliding speeds. Note that the friction force during step-down is negative because it is an assistive lateral force (as explained in Figure 4.3). The experimental results presented here were performed by Dr. Zhe Chen and Dr. Seong H. Kim group at Penn State University. [200]

### 4.1.4. Discussion

Taken together, the observed COFs and analysis of the MD simulations provide insight into the physical and chemical origins of friction. Super-lubricity is achieved when

topography- and interlocking-induced strain and chemical bonding at the shear plane are negligible. The large friction during step-up over the 0.34 nm high graphene step-edge can be attributed to synergy of physical effects due to topography and chemical effects due to interfacial bonding. During the step-down direction, the negative topography change produces a force assisting the sliding motion whereas the chemical bonds between oppositely moving surfaces produce a resistive force. The balance of these two components will determine whether friction and the COF are positive or negative.

The topography effect can be explained in terms of the two forces acting on the AFM probe: the applied normal force from the cantilever and the force from the graphene step edge (Figure 4.10). The horizontal component of the force from the step edge contributes to the lateral force measured in the experiment. It is resistive for the step-up motion and assistive for the step-down motion, and its magnitude increases as the applied normal load increases. The chemical effect originates from interactions with the OH groups at the graphene step edge. This force always resists the motion, regardless of the scan direction, and its magnitude is related to the contact area between the tip and the surface (more accurately, the length over which the step edge crosses the contact area). According to the Derjaguin-Muller-Toporov (DMT) contact model [208], the contact area is proportional to the cube root of the normal force. Therefore, as the applied normal load increases, the assistive force due to the topographic height change increases much faster than the resistive force due to chemical interactions during the step-down motion, leading to a negative COF [203]. When the topography-induced assistive force is larger than the chemistry-induced resistive force, negative friction can take place.

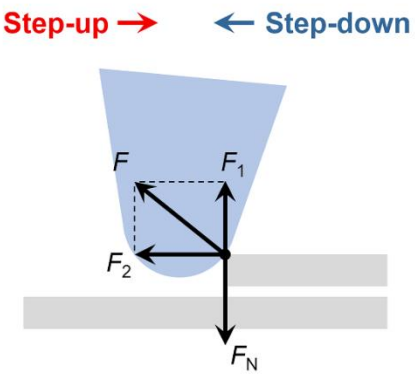


Figure 4.10 Force analysis diagram of the AFM tip at a graphene step edge.

From Figure 4.3, Figure 4.6(a) and Figure 4.6 (b), it can be seen that chemical interactions at the step edge synergistically amplify the resistive force of topography while the tip ascends the step; in contrast, the cancelation effect between the resistive force due to chemical interactions and the assistive force from the topography effect during the descending motion is not as big as the amplification effect during the ascending motion. This may explain why achieving superlubricity is difficult on atomically rough surfaces unless the topographic surface features are chemically inert. As the atomic corrugation increases, friction increases due to both chemical (more site available for hydrogen bonding)

and physical (larger topographical features) effects (Figure 4.11). When surface wear occurs during sliding, dangling bonds can be exposed at the worn surface as well as on wear debris and molecules impinging from the gas phase will react at those sites. In ambient air, reactive molecules are primarily oxygen and water and their reactions lead to surface oxidation and hydroxylation. The findings of this study suggest that the oxygenated functional groups at the newly exposed topographically corrugated surfaces will greatly enhance interfacial friction when wear is involved.

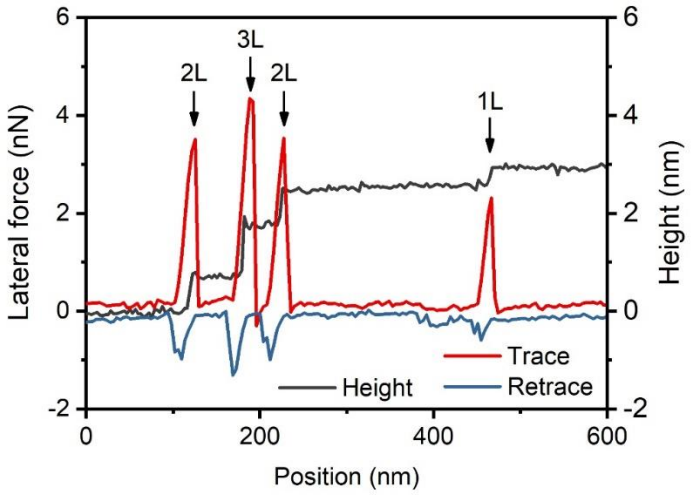


Figure 4.11 Lateral force of the AFM tip at multilayer graphene step edges. According to the height profile (dark grey line), there are four step edges in the scan area. From left to right, these four graphene step edges are of 2 layers (2 L), 3 layers (3 L), 2 layers (2 L), and 1 layer (1 L) respectively. The experimental results presented here were performed by Dr. Zhe Chen and Dr. Seong H. Kim group at Penn State University. [200]

The fact that physical and chemical factors have opposite effects on friction of the surface with atomic scale corrugations suggests that they might be leveraged to minimize sliding resistance at tribological interfaces. This concept is illustrated by the zero friction that is observed between the chemically-dominated and physically-dominated regions during step-down (at lateral positions of -2.5 nm and 2.5 nm in Figure 4.3). At these positions, friction is even smaller than the super-lubricity observed on the basal plane. These findings suggest opportunities to tune the COF with prescribed topographic features and terminating species. While this concept may be impractical in an industrial setting with current technology, fundamental understanding of chemical and topographic origins of friction holds great promise for future scientific advances and opens the possibility of tunable friction.

## 4.2. Identifying physical and chemical contributions to friction: A comparative study of chemically inert and active graphene step edges

Here, we explored the atomistic mechanisms governing the magnitude of friction during the step-up and step-down processes on a topographic step of a single layer

graphene edge (0.34 nm high) on a graphite basal plane. This system was studied experimentally using atomic force microscopy (AFM) with a sharp silicon tip covered with an amorphous native oxide layer and computationally using reactive molecular dynamics (MD) simulations. As shown in Figure 4.12, three different cases were studied: (i) graphene step edges with OH groups capable of H-bonding interactions, (ii) graphene step edges with hydrophobic species, and (iii) buried graphene step edges covered with another graphene layer. The second case was implemented by the physisorption of alcohol at the OH sites in experiments or chemisorption of alcohol via dehydration reaction with the OH group forming alkoxide groups in simulations. Depending on the size of the alkyl moiety of the alcohol molecule or the alkoxide group, the deformability of molecular species at the topographic step can vary. In our study, methanol (ii-α) and n-pentanol (ii-β) were used to model short and long alkyl chains at the step edge. Results revealed that, unless the topographic step is completely chemically inert, the resistive force during the step-up process is always larger than the assistive force during the step-down process. The magnitude of this hysteresis depends on the degree of the sliding direction-dependent physical deformation of molecular moieties at the topographic step, which in turn depends on their chemical interactions with the counter-surface.

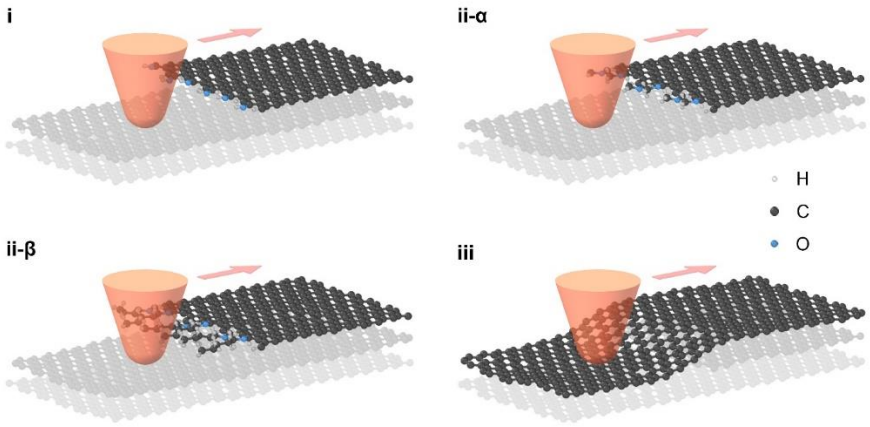


Figure 4.12 Illustrations of the systems studied. Each system comprises an AFM tip (counter-surface) and a graphite surface with an atomic step edge whose height is 0.34 nm, corresponding to the thickness of a single graphene layer. (i) The graphene step edge is exposed and terminated with chemically active OH groups. (ii) The step edge is exposed and terminated with physisorbed alcohol molecules or chemisorbed alkoxide groups; short (ii-α) and long (ii-β) alkyl groups are considered. (iii) The step edge is buried under another graphene layer.

### 4.2.1. Materials and Methods

*4.2.1.1. Nanoscale friction measurement*

The experiments described as followed were performed by Dr. Zhe Chen and Dr. Seong H. Kim group at Penn State University. [209]A fresh graphite surface was prepared through tape-exfoliation on a highly oriented pyrolytic graphite (HOPG) crystal in ambient air. Nanoscale friction tests were performed with AFM (Multimode, Bruker, US) using Si tips (ESP-V2, Bruker, US; nominal spring constant: 0.2 N/m, nominal tip radius: 8 nm) to

rub against the fresh graphite surface in contact mode. The sliding direction of the AFM tip was kept nearly perpendicular to the graphene step edges. Before the friction test, the AFM tip was treated with UV/ozone for 15 minutes to remove possible organic contaminants. During the test, the reciprocating frequency of the tip was 2 Hz and the scan size was 80 nm, so the tip sliding speed was 0.32 μm/s. The applied normal force on the AFM tip was in the range of 7.8 nN to 23.5 nN. According to the Derjaguin-Muller-Toporov (DMT) contact model,[208] based on the nominal tip radius, the contact pressure varied between 2.2 GPa to 2.7 GPa. The normal spring constant of the AFM probe cantilever was calibrated following the Sader's method.[210] The lateral sensitivity of the cantilever and detector was calculated by comparing the measured lateral signal (in the unit of mV) on a reference sample with the known coefficient of friction (COF).[200] The reference sample was a Si wafer coated with diamond-like carbon, and the COF was about 0.15 in n-pentanol vapor.[211] Each of the lateral force and vertical position profiles was the average of 128 scans at the same location. The friction tests were carried out at room temperature (22 °C to 25 °C). A mixture vapor of dry N2 and alcohol vapor flowed through the sample chamber. P/Psat of the alcohol vapor was controlled via the ratio between the dry N2 and the saturated alcohol vapor.[212] The alcohol used here includes methanol (Sigma-Aldrich, 99.8%) and n-pentanol (Sigma-Aldrich, ≥99%). The dry N2 used in our experiments had a dew point of about -35 °C, meaning that the water concentration was 200-300 ppm.

#### *4.2.1.2. Characterization of the adsorbed molecules on graphite surfaces*

The adsorption of methanol and n-pentanol on the freshly-exfoliated graphite surface was analyzed with polarization-modulation reflection-absorption infrared spectroscopy (PM-RAIRS). PM-RAIRS analysis was carried out with a Thermo Nicolet Nexus 670 spectrometer equipped with a custom-designed reflection-absorption unit consisting of a ZnSe PM crystal, an environment control chamber, and an MCT-A detector.[213] The PM operation was done using a photoelectric modulator (HINDS Instruments PEM-90) and a demodulator (GWC Instruments). The IR beam incidence angle was 81° from the surface normal. The PM-RAIRS spectra of the graphite surface were normalized with the spectrum of a clean gold surface obtained in dry N2 to remove the Bessel function shape background from the phase demodulation process. The environment control was the same as that in the nanoscale friction measurement.

### 4.2.2. Reactive MD simulations

Reactive MD simulations were used to model a silica tip sliding across a single-layer graphene step edge from the upper terrace to the lower terrace and back. The graphene step edge had an armchair structure, and four model systems with different edge terminations were created (see Figure 4.13). The first model system mimicked the measurement in dry nitrogen condition by terminating the step edge with alternating hydrogen and OH groups and the silica tip with OH groups. The second model system mimicked the experimental measurement in methanol vapor with a graphene step edge terminated with alternating hydrogen and methoxy groups and the silica tip terminated with methoxy groups. The third model system imitated the experimental measurement in n-pentanol vapor by modeling a graphene step edge terminated with alternating hydrogen

and pentoxy groups. To ensure that the model tip size was comparable to the other cases, the silica tip was terminated with methoxy groups. Finally, the fourth system simulated sliding on a buried step edge, where a complete graphene layer covered a non-passivated step edge.

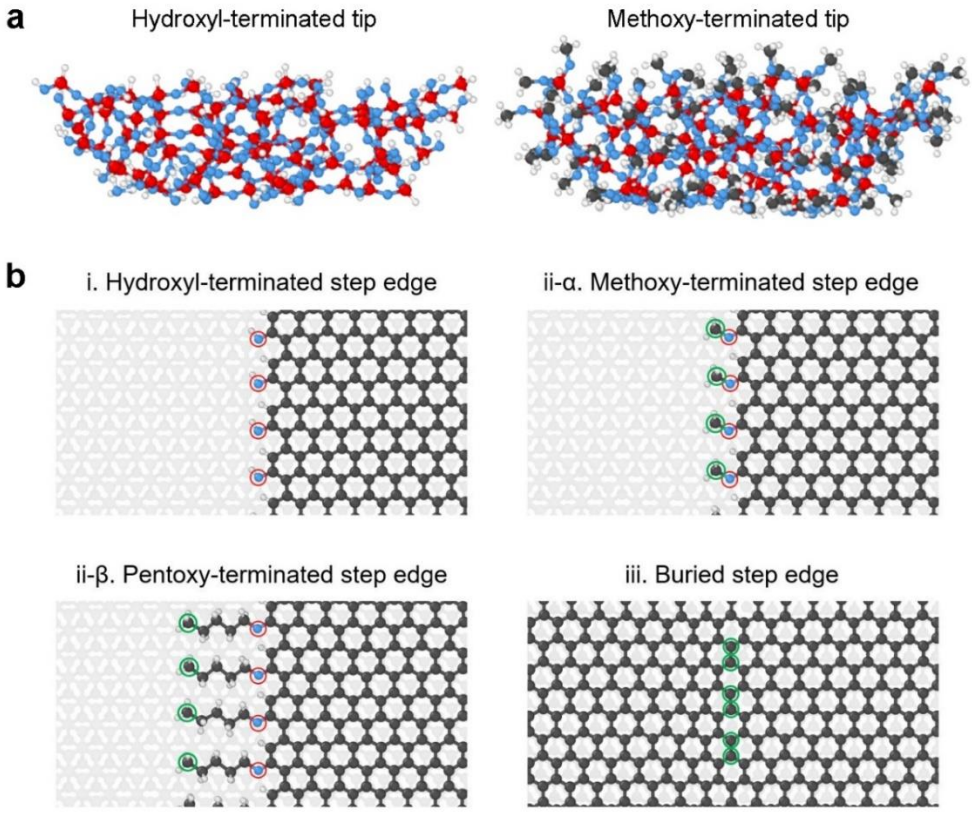


Figure 4.13 (a) Front view of the model tips and (b) top view of the graphite surfaces in the MD simulations. The displacement of the carbon and oxygen atoms indicated by red and green circles in (b) are calculated and displayed in Figure 4.16.

The simulations used the ReaxFF[129] force field with a set of parameters previously developed[214] from a combination of parameters for C/H/O [215, 216] and Si/C [217] interactions. The amorphous silica structure of the tip was created by heating cristobalite to 4000 K and then quenching to room temperature at a rate of 0.02 K/fs.[75, 200] To increase computational efficiency, the tip was created in a semi-circular disc shape, with curvature (radius), thickness, and height of 2.5 nm, 1.5 nm, and 1.5 nm, respectively. As for the graphite surface, only three layers of graphene were considered and only the top two layers were deformable both at the upper and lower graphite basal planes. The substrate dimensions were 9.8 nm in the sliding direction (x-direction), 4.2 nm perpendicular to the sliding direction on the basal plane (y-direction), and about 1.0 nm normal to the graphite basal plane (z-direction).

Each simulation was performed in four different steps: i) initial energy minimization and equilibrium until the potential energy reached steady state; ii) vertical displacement of the tip toward the substrate at the speed of 10 m/s until the minimum

distance between the tip and substrate reached 0.3 nm; iii) application of 10 nN normal force to the top rigid part of the tip for 120 ps, which corresponds to about 5.0 GPa pressure based on the DMT model;[208] and iv) dragging the tip in the sliding direction (perpendicular to the step edge) at a speed of 10 m/s using a harmonic spring with a 6 N/m stiffness constant. The canonical ensemble was employed with a Langevin thermostat to maintain the temperature at 300 K throughout the simulations. The velocity of the atoms in the sliding direction was excluded from the temperature calculation used by the thermostat. During the sliding process, the lateral force was calculated as the sum of the forces on all the tip atoms in the sliding direction. To reduce the noise in the lateral force, averages were taken every 0.1 ps. All the simulations were performed using the large atomic/molecular massively parallel simulation (LAMMPS) code,[130] and OVITO software [131] was used to visualize the results.

### 4.2.3. Results and Discussion

*4.2.3.1. AFM-based single-asperity friction measurement*

Figure 4.14 illustrates the AFM-based single-asperity friction tests. The Si tip used for AFM measurements had a native oxide layer terminated with silanol groups due to UV/ozone cleaning.[212] The exposed graphene step edges were terminated with H atoms and OH groups due to reactions with water molecules in the gas phase during mechanical exfoliation in ambient air.[187, 218] In case (i), the nanoscale friction tests were performed in dry nitrogen, where transient H-bonding interactions can occur between the tip and the step edge (Figure 4.14 (a) i).[200] In case (ii), friction tests were performed in alcohol vapor conditions.[123, 219] We tested two alcohols with different alkyl chain lengths – methanol (Figure 4.14 (a), ii-α) and n-pentanol (Figure 4.14 (a), ii-β). In these two cases, H-bond formation between the tip and the step edge is suppressed because the alcohol molecules readily adsorb on the native silicon oxide surface,[220] covering the silanol groups. As shown in Figure 4.15, the C-H stretching vibration signals in the PM-RAIRS spectra collected in alcohol vapor verify that alcohol molecules adsorb on the HOPG surface that consists of primarily graphite basal planes and a small number of steps. The OH-terminated step edges should be the primary sites for alcohol adsorption because of the H-bonding interactions. By comparing the spectra of graphite and Au, we confirmed that, at 80% relative partial pressure of alcohol with respect to its saturation (P/Psat), the number of alcohol molecules adsorbed on the graphite surface is less than a monolayer but far exceeds what is needed to fully cover the step edge sites. If physisorbed molecules are removed due to the shear or sliding action, molecules impinging from the gas phase instantaneously replenish the vacant sites.[219] Thus, the adsorption of alcohol molecules on the sliding surfaces can be assumed to remain constant. In case (iii), friction was measured on a buried step edge (Figure 4.14 (a) iii) with the same height (0.34 nm) that was nearly parallel to the nearby exposed step edge. Thus, friction forces were measured for both exposed and buried step edges with the same AFM tip under identical applied load and sliding speed conditions in different environments (dry nitrogen, methanol vapor, and n-pentanol vapor).

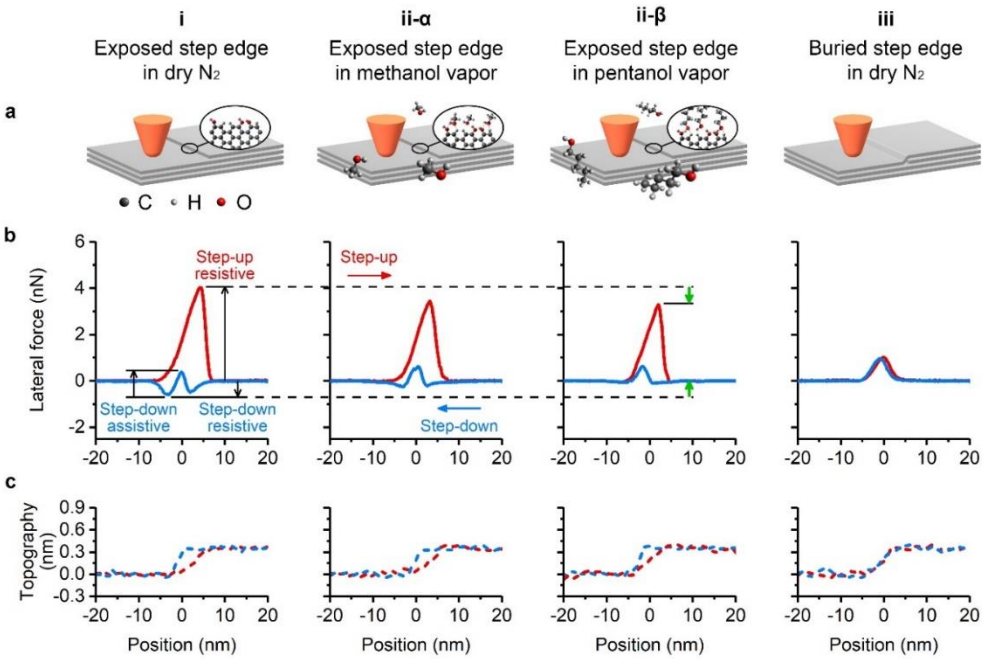


Figure 4.14 Experimental setup and results of the AFM-based nanoscale friction tests. (a) Four sets of friction tests in which a Si AFM tip slides over an exposed single-layer graphene step edge in (i) dry nitrogen, (ii-α) methanol vapor, and (ii-β) n-pentanol vapor, and (iii) the same Si tip sliding over a buried single-layer graphene step edge in dry nitrogen. (b) Lateral force for the tip sliding in the step-up (red) and step-down (blue) directions. The resistive force during step-up and step-down and the assistive force during step-down are identified by black arrows in the leftmost panel. The green arrows in the third panel indicate changes in the contribution of chemical interactions. (c) Topography recorded along its sliding path where zero is defined as the position of the tip on the lower terrace. All friction tests were conducted with a single AFM probe with an applied normal force of 23.5 nN. The experimental results presented here were performed by Dr. Zhe Chen and Dr. Seong H. Kim group at Penn State University. [209]

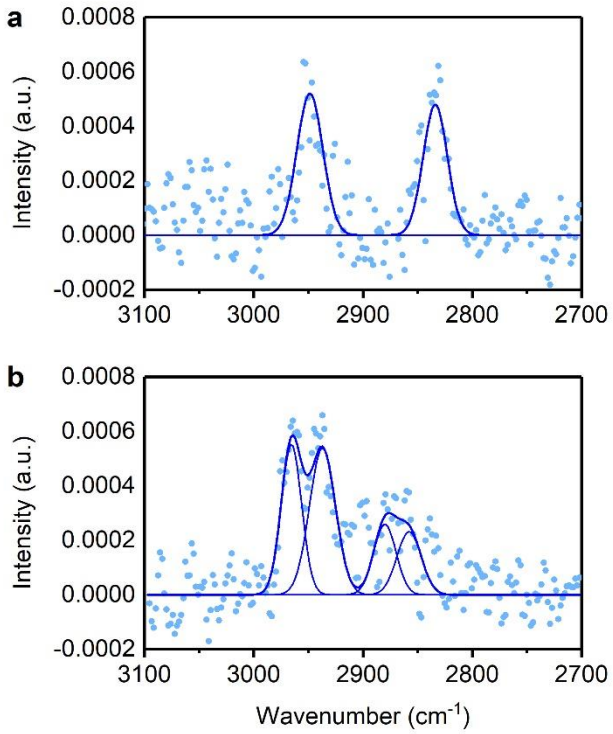


Figure 4.15 PM-RAIRS spectra on the graphite surface. Spectra were taken in (a) methanol vapor and (b) n-pentanol vapor at P/Psat = 80%. The raw spectra obtained from 4000 scans are shown as symbols and the fit results are shown as lines. The experimental results presented here were performed by Dr. Zhe Chen and Dr. Seong H. Kim group at Penn State University. [209]

Figure 4.14 (b) shows the lateral force measured with an applied normal force of 23.5 nN. Each of the lateral force profiles is the average of data collected from 128 scans at the same location. Adhesion measured before and after the friction tests was unchanged, indicating minimal wear of the tip. Data collected at other normal forces (7.8 and 15.7 nN) exhibit similar trends. During the step-up scan, a positive lateral force means resistance to the sliding motion of the AFM tip, and a negative lateral force corresponds to assistance to the motion. During the step-down scan, because the sliding direction is reversed, the sign of the lateral force has the opposite meaning; i.e., negative is resistive and positive is assistive. The three components of the lateral force signal, i.e. step-up resistive, step-down resistive, and step-down assistive, are identified with black arrows in Figure 4.15 (b), i.

In dry nitrogen (case i), there is a strong resistive force as the AFM tip ascends the OH-terminated step, while the friction behavior during the step-down process is composed of the superposition of a broad resistive force and a sharp assistive force.[221, 222] According to a previous study,[200] the step-up resistive component is due to the combined effects of the topographic height increase and the transient H-bond formation at the step, the step-down resistive component originates from the H-bonding interaction, and the step-down assistive component is caused by the height decrease. Interestingly, the magnitude of the step-up resistive component is much larger than the sum of the magnitudes of the step-down assistive and step-down resistive components. The step edge is not damaged by the

repeated scans, the OH coverage does not change over time and the resistive force induced by H-bonding is expected to be the same (at least similar) for both step-up and step-down scans. Therefore, it can be deduced that, in the presence of H-bonding interactions, the topography-induced resistive force during the step-up is much larger than the topography-induced assistive force during the step-down. In contrast, for the case of the buried step edge (case iii), where there is no chemical interaction so that the step-down resistive component is zero, the magnitudes of the step-up resistive and step-down assistive forces are the same within the experimental error. Based on these observations, one may hypothesize that the topography effect during the step-up process is magnified by the H-bonding interaction at the graphene step edge.[200]

However, this hypothesis is not fully supported by the results of friction tests conducted in methanol or n-pentanol vapor (case ii). When the environmental condition is switched from dry nitrogen to methanol vapor (case ii-α), the magnitudes of both step-up resistive and step-down resistive components decrease. When the environment is switched to n-pentanol vapor (case ii-β), there is a larger decrease in the step-up resistive and step-down resistive components (green arrows in Figure 4.15 (b), ii-β); in fact, the step-down resistive component becomes negligible. This indicates that the adsorbed alcohol molecules can suppress the transient H-bonding interaction between the Si tip and the exposed graphene step edge. The observation that the resistive force in methanol vapor is larger than that in n-pentanol could mean that the methyl group is not large enough to fully suppress the H-bonding interactions. Regardless, for both cases with and without H-bonding interactions, the magnitude of the step-up resistive force is much larger than that of the step-down assistive force.

The height profile recorded during the contact scan is plotted in Figure 4.15 (c). For the exposed graphene step edges (cases i, ii-α, and ii-β), the step-up profile has a smaller slope compared to the step-down profile, resulting in a hysteresis between step-up and step-down. This hysteresis is not observed for the buried step edge (case iii). Thus, the hysteresis in the recorded topography cannot be attributed to an artifact caused by the feedback control during the AFM scan across the topographic feature with the 0.34 nm height. Rather, it must be related to the large difference in the magnitude of the step-up resistive force and the step-down assistive force. In AFM, the recorded topography is the vertical trajectory of the upper part of the tip attached to the cantilever, not the position of the lower end of the tip in contact with the sample. The exact position of the tip apex in contact with the surface is difficult to determine; thus, AFM height profiles cannot provide a definitive explanation for the friction hysteresis at the exposed step edges.

#### *4.2.3.2. Reactive MD simulations*

MD simulations were performed to explain why the magnitude of the step-up resistive force is larger than that of the step-down assistive force for the exposed step edges with various chemical functionalities – hydrophilic OH groups and hydrophobic alkoxide groups. As shown in Figure 4.16 (a) and Figure 4.13, four model systems mimic the four experimental cases. To model the friction tests in dry nitrogen, the silica tip was terminated with silanol groups (cases i and iii), and the exposed graphene step edge was terminated with H atoms and OH groups alternately (case i). To model the friction tests in methanol or n-pentanol vapor, where alcohol molecules adsorb on both the AFM tip and the graphene

step edge, the silanol groups on the silica tip surface were approximated by methoxy groups and the OH groups at the exposed graphene step edge were replaced with methoxy groups or pentoxy groups (cases ii-α and ii-β). This strategy of modeling alkoxide groups to terminate the tip surface and the step edge was adopted to capture the important chemical features of the four cases with model systems small enough to simulate using reactive MD.

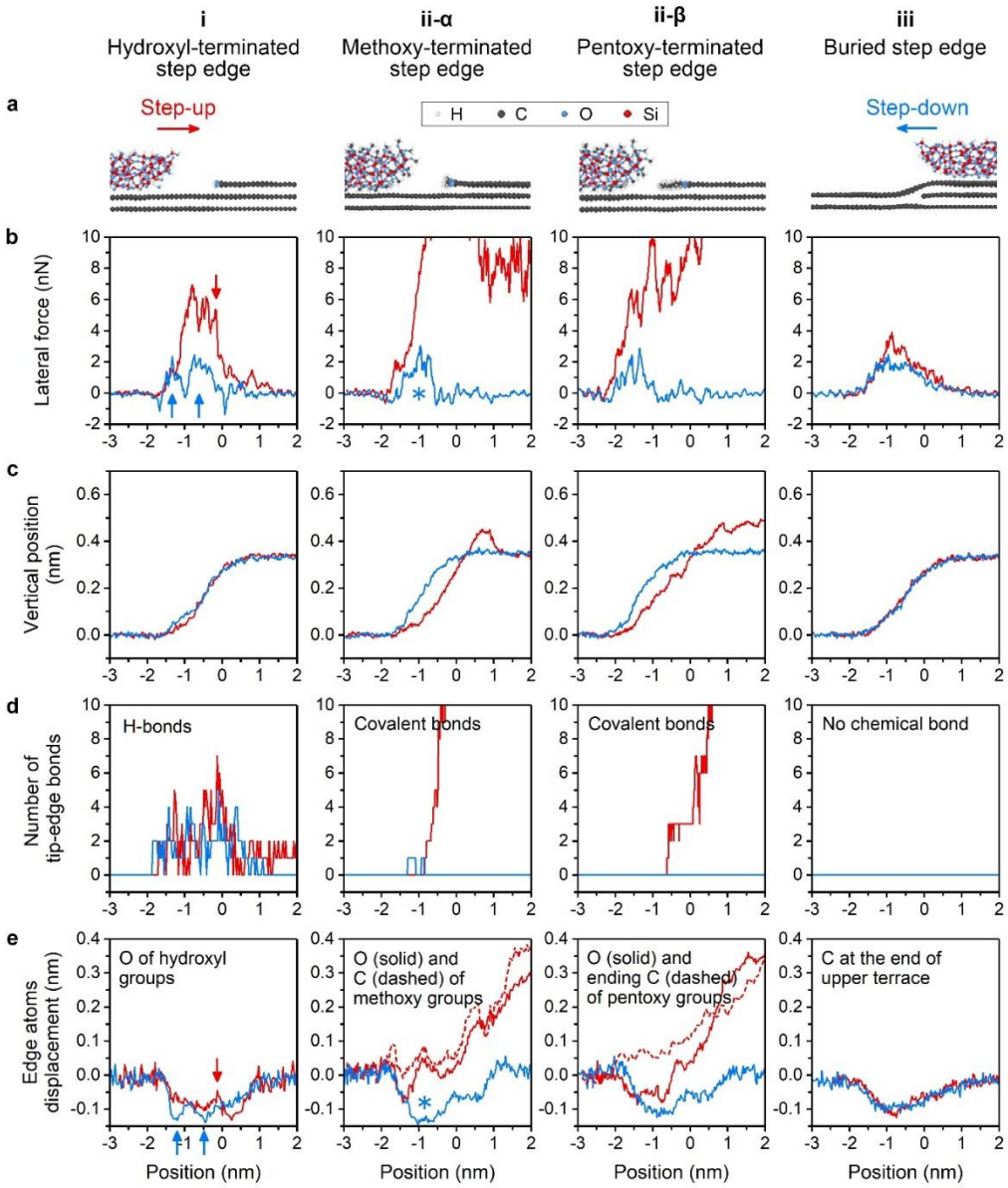


Figure 4.16 Reactive MD simulations of a silica tip sliding over a single-layer graphene step edge. (a) Close-up, side-view snapshots of the different models: (i) silanol-terminated tip on OH-terminated exposed step edge, (ii-α) methoxy-terminated tip on methoxy-terminated exposed step edge, (ii-β) methoxy-terminated tip on pentoxy-terminated

exposed step edge, and (iii) silanol terminated tip on buried step edge. (b) The lateral force and (c) vertical position of the tip. (d) The number of hydrogen or covalent bonds between the tip and the graphene step edge. (e) The average displacement of the carbon and/or oxygen atoms at the graphene step edge (see Figure 4.13 for the exact location of the atoms) where the x-axis refers to the lateral position of the center of the tip with respect to the step edge. The data collected during step-up are in red and during step-down are in blue. The arrows and asterisks are shown to guide the discussion in the main text.

As shown in Figure 4.16 (b), the lateral force obtained from MD simulations exhibits similar trends as measured in the AFM experiments. First, the resistive force during step-up is much larger than the assistive force during step-down for the OH-terminated step edge (Figure 4.16 (b) i), whereas these assistive and resistive forces have similar magnitudes for the buried step edge (Figure 4.16 (b) iii). Further, there are clearly identifiable resistive peaks during step-down for the OH-terminated graphene step (case i) that are not present for the buried step edge (case iii). Finally, the step-down resistive force is smaller for the methoxy-terminated and pentoxy-terminated graphene step edges (Figure 4.16 (b), ii-α and ii-β) than for the OH-terminated edge. These trends are consistent with the experimental results shown in Figure 4.14 (b). However, unlike the experiments, the simulation results predict the step-up resistive force can be significantly larger for the methoxy-terminated and pentoxy-terminaed graphene step edges than the OH-terminated step edge. The simulated lateral force eventually drops back to the basal plane value when the tip moves far enough from the step. Despite this difference, the simulations capture the key trends of the experiments and therefore will be analyzed to understand the mechanisms underlying those trends.

Figure 4.16 (c) shows the vertical position of the center of mass of the amorphous silica tip in the MD simulations. For the buried step edge (case iii), the tip trajectories during the step-up and step-down processes are identical. For the OH-terminated step edge (case i), there is a small hysteresis between the step-up and step-down trajectories. For the methoxy-terminated (cases ii-α) and pentoxy-terminated (case ii-β) graphene step edges, there is hysteresis between the step-up and step-down trajectories and the slope of the step-up trajectory is slightly smaller than that for step-down, consistent with the experimental measurements. This hysteresis indicates that the location at which the tip starts ascending the step edge differs from the location at which the tip finishes descending the step edge. The main difference from the experiments is that the simulated tip trajectory reaches a final position much higher than the upper terrace, although it eventually comes back to the level of the upper terrace (as shown in case ii-α). This is attributable to the difference between the chemisorbed alkoxide groups in simulations and the physisorbed alcohol in AFM experiments (discussed later along with Figure 4.17).

Figure 4.16 (d) shows the transient chemical bonds formed between the tip and the step edge. As expected, there are several transient H-bonds formed between the OH-terminated silica tip and the OH-terminated step edge during both step-up and step-down processes (case i), while there are no chemical bonds between the tip and the buried step edge (case iii). For the methoxy-terminated (case ii-α) and pentoxy-terminated (case ii-β) graphene step edges, there are no chemical interactions between the tip and the step edge during the step-down process. However, covalent bonding is observed during the step-up

process for these two cases. As the tip ascends the step, initially the friction increases but there is no bonding. However, when the tip is partially up the step, there is a sharp increase of covalent bonding for both the methoxy-terminated and pentoxy-terminated graphene step edges. The origin and implications of this covalent bonding in methoxy (ii-α) and pentoxy (ii-β) cases will be discussed later.

The degree of physical deformation or deflection of functional groups during the scan was quantified from the displacement of individual atoms at the step edge in the simulations. Figure 4.16 (e) shows the average displacement of the carbon and/or oxygen atoms at the graphene step edges (atoms being tracked are identified in Figure 4.13). For the buried step edge (case iii), the terminal carbon atoms are deflected downward by almost the same magnitude during step-up and step-down. For the OH-terminated step edge (case i), the maximum downward deflection is similar for step-up and step-down, but they occur at different lateral positions. This trend can be attributed to the transient H-bonds (Figure 4.16 (d), i) and their effect on the tip trajectory (Figure 4.16 (c), i). Specifically, as the tip ascends the step, it is pulled down due to the H-bonding with the surface OH groups; at the same time, the step-edge OH groups H-bonded to the tip are pulled up slightly.[200] Such upward bending of the H-O-Cgraphene could cause a large resistive force (see, for example, the red arrows in Figure 4.16 (b), i and Figure 4.16 (e), i). Quantitative correlations between H-bonding, deflection and friction could not be drawn because the calculated friction force is the sum of various processes stochastically occurring over a specific time frame and location in MD simulations. Nonetheless, the qualitative correlation suggests that local deformation of the terminal groups at the topographic step, which are coupled with transient chemical interactions with the counter-surface, play critical roles in determining the magnitude of friction.

In the first part of the simulated step-up processes for the methoxy-terminated (case ii-α) and pentoxy-terminated (case ii-β) step edges, there are no covalent bonds formed between the tip and the step edge (i.e. before -0.8 nm in Figure 4.16, ii-α and ii-β). In this region, the terminal carbon atoms of the alkoxide groups are pushed upwards, while their oxygen atoms are pushed downwards. This means that the alkoxide groups are highly deformed or physically strained from their equilibrium conformations. To show this clearly, the deformation of pentoxy groups (case ii-β) is analyzed in Figure 4.17; the lateral force is replotted for this case in Figure 4.17 (a). A series of snapshots from the MD simulations during the step-up process are shown in Figure 4.17 (b). Initially only the terminal methyl group is bent upward, but gradually the whole pentoxy group is bent up as the tip travels further toward the upper terrace. Similar behavior was observed for the methoxy group in case ii-α. Thus, it can be concluded that the physical deformation of the alkoxide group is the main cause of the high friction during the step-up process in this region. A similar process is likely to occur for the physisorbed alcohol molecules in the AFM experiment. Such severe deformation does not occur during the step-down process; only small and gradual downward deformations are observed (see Figure 4.17 (c)). These results indicate that the difference in lateral force associated with the anisotropic deflection of the alkyl groups at the graphene step edge is the origin of the friction hysteresis between step-up and step-down.

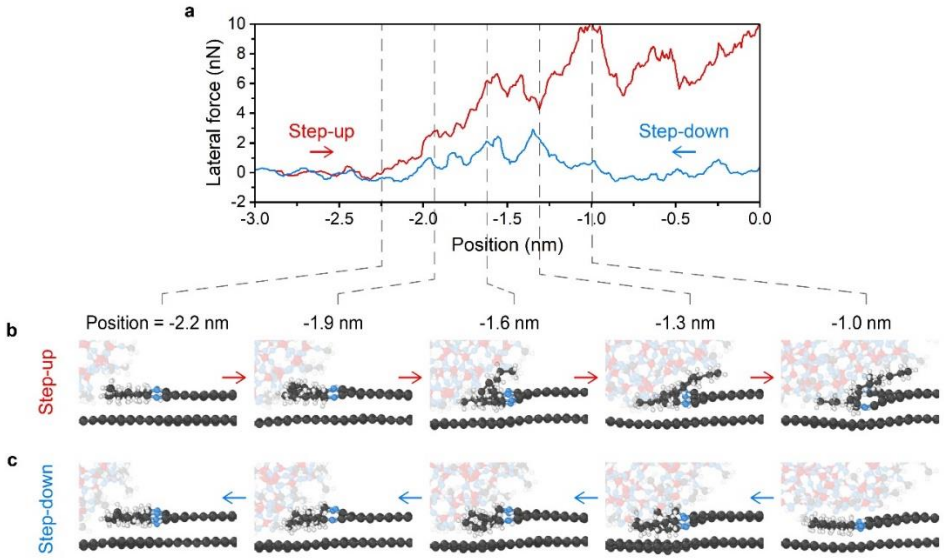


Figure 4.17 Anisotropic deformation of the pentoxy groups at the graphene step edge. (a) Lateral force from simulations of the pentoxy-terminated step edge (case ii-β). Side view snapshots of the MD simulation showing the deformation of the pentoxy groups at the step edge during the (b) step-up and (c) step-down processes. Tip atoms are faded to highlight the behavior of the step edge.

Deflection of the alkyl groups at the step edge also explains the chemical bonding that dominates the lateral force behavior in the latter part of the step up process (tip position > 0.8 nm) for the methoxy-terminated and pentoxy-terminated step edges (Figure 4.16 (d), ii-α and ii-β). In this region, the chemisorbed alkoxide groups are substantially deformed (severely bent), so that chemical reactions occur between the deformed alkoxide groups and the counter-surface. It is known that the shear-induced physical deformation of chemisorbed molecules can lower reaction barriers, thereby facilitating chemical reactions that normally do not happen in thermal reaction conditions.[75, 133] This is called a tribochemical reaction.[18, 24, 223, 224] Based on the high degree of strain in the molecular conformation of pentoxy group that can be seen in the last frame of Figure 4.17 (b), one can imagine that further deformation will destabilize the pentoxy group enough to cause the dissociation of the Opentoxy-Cgraphene bonds at the step edge and the formation of new chemical bonds with the counter-surface. Subsequently, the position of the oxygen atom of the alkoxide group follows the trajectory of the terminal carbon atom. Such tribochemical processes may not occur readily for the physisorbed molecules because they can be pushed to a lower pressure zone in the contact area.[133] Since the decrease in the resistive force magnitude during step-up is similar to the decrease in resistive force during step-down in our experiments (see green arrows in Figure 4.14 (b), ii-β), it is unlikely that the physisorbed alcohol molecules are completely squeezed out of the contact region, which would allow direct H-bonding between the tip and the step edge.

During the step-down process in all four cases, the edge atoms are pushed downwards (Figure 4.16 (e)). Taking a closer look at the buried step edge (case iii), the step-down assistive force correlates well with, almost mirroring, the downward deflection of the edge atom. In the OH-terminated (case i) and methoxy-terminated (case ii-α) step edges, the locations of large assistive force in Figure 4.16 (b) also closely coincide with tip positions where the downward deflection of the edge atoms is large in Figure 4.16 (e) (marked with blue arrows in case i and asterisks in case ii-α). In the pentoxy-terminated step edge (case ii-β), the positions of small spikes in the assistive force during step-down correspond with positions where the pentyl groups are highly kinked (for instance, see three snapshots at -2.0 nm, -1.6 nm, and -1.3 nm in Figure 4.17 (c)). All these observations suggest that the elastic recovery of the deformed moieties at the step-edge exerts an assistive force that pushes the tip along the descending direction.

The observations made here based on AFM measurements and MD simulations of an ideal graphene step edge have practical implications for real engineering materials and systems. For example, these results explain the environmental sensitivity of hydrogenated diamond-like carbon (H-DLC).[225-229] In dry nitrogen, H-DLC exhibits superlubricity with a friction coefficient lower than 0.01 after the initial run-in period.[225] During the run-in, the oxidized surface layer wears off [229] and the material in the sliding interface becomes graphitic.[230] Such graphitic layers are neither highly crystalline nor atomically flat,[231, 232] likely exhibiting step-edge-like defects. If such defects are chemically inert or deform reversibly, they would not increase friction significantly (similar to case iii). When H-DLC friction is measured in humid air, the formation of OH groups is inevitable due to reactions of dangling bonds with water molecules impinging from the gas phase. The H-bonding interactions at the edges of graphitic layers will cause high friction (similar to case i), which could be a reason that H-DLC loses its superlubricity in ambient air. Even if H-DLC friction is measured in alcohol vapor environments, which can suppress the H-bonding interactions,[228] the superlubricity is lost due to the anisotropic deformation of alcohol molecules or alkoxide groups at the edges of sliding graphitic layers (similar to case ii). The present study has shown that both chemical interactions and physical deflection must be mitigated to obtain ultra-low friction, suggesting new directions in surface engineering.

### 4.3. Effect of Ambient Chemistry on Friction at the Basal Plane of Graphite

Graphite is widely used as a solid lubricant due to its layered structure which enables ultra-low friction. However, the lubricity of graphite is affected by ambient conditions and previous studies have shown a sharp contrast between frictional behavior in vacuum or dry environments compared to humid air. Here we studied the effect of organic gaseous species in the environment, specifically comparing the adsorption of phenol and pentanol vapor. Atomic force microscopy experiments and reactive molecular dynamics simulations showed that friction was larger with phenol than pentanol. The simulation results were analyzed to test multiple hypotheses to explain the friction difference and it was found that mechanical force-driven chemical bonding between the tip and phenol molecules plays a critical role. Bonding increases the number of phenol molecules in the contact which increases adhesion as well as the number of atoms in registry with the topmost graphene layer that act as pinning sites to resist sliding. The findings of this research provide insight into how the chemistry of the operating

environment can affect the frictional behavior of graphite and layered materials more generally.

### 4.3.1. Introduction

Graphite is used as a solid lubricant in many applications due to its excellent tribological performance. Ideally, graphite solid lubricants could function across a wide range of environmental conditions. Unfortunately, ultra-low friction is not an intrinsic property and many previous studies have shown that the lubricity of graphite is highly sensitive to the environment.[233] Macro and micro-scale measurements have shown that friction on graphite is relatively high in vacuum or dry nitrogen,[234 235] but can be decreased significantly by the presence of gaseous species including water and oxygen. [234, 236] The same trends have been observed in nanoscale experiments based on atomic force microscopy (AFM)[237-242] as well as atomic-scale simulations.[237-239, 243]

Nanoscale studies have suggested multiple mechanisms for the environment-dependent friction of graphite. Most of these mechanisms are centered around the physical and chemical interactions between gas phase species in the environment and atomic-scale defects on the graphite surface.[237, 240-245] AFM and nanoindentation studies suggested that friction of graphite in dry conditions can increase due to interactions between the tip and defects on the graphite surface generated during sliding.[241, 242] In this context, the role of water molecules is to neutralize dangling bonds and reduce covalent bond formation in the interface, thus decreasing the probability of wear and associated friction.[241, 242] These experiments were supported by density functional theory (DFT) calculations, which showed that water molecules physisorb on the basal plane of graphite and chemisorb at point defects like vacancies. [243, 244] Further, lower friction achieved with a hydrophobic tip compared to a hydrophilic tip showed that chemical interactions between the AFM tip and graphite surface also contribute to friction. [240, 245] Other studies that did not consider defects attributed environment effects to physisorption. A recent study [238] using AFM complemented by molecular dynamics (MD) simulations suggested an intrinsic friction hysteresis mechanism related to the motion of water molecules across the graphene basal plane that strongly depends on both humidity and the hydrophobicity of graphite basal plane. This study attributed friction hysteresis between loading and unloading in a humid environment to changing contact angles due to physisorbed water on the graphite. Grand Canonical Monte Carlo simulations and AFM experiments [237] showed that friction varied nonmonotonically with humidity and that this trend could be explained by physisorption of water in the contact region that affected the quality of the contact. However, the hypothesis of water adsorption on the basal plane of graphite may not fully explain the observed humidity dependence of friction because a recent study measuring water adsorption isotherm on a freshly exfoliated graphite surface showed that water adsorption does not occur readily until the humidity approaches the saturation point.[222]

Most studies mentioned above compared vacuum or dry nitrogen with humid air environments. However, in typical ambient conditions, chemical species other than water and oxygen are present, for example organic molecules. Further, graphitic surface coatings [246] and lubricant additives [247-249] may be exposed to hydrocarbons and their derivatives in lubricating oils. Vapor phase lubrication studies at the macro scale showed that hydrocarbons have a more significant effect on lubricity than water since they require lower

relative partial pressure than water for effective lubrication.[250] These experiments suggested that molecular species adsorbed on the graphite basal plane can act as a reservoir from which the molecules can migrate to and neutralize defect sites during the sliding process. Further, it was shown that the lubricity of alcohols and alkanes on graphite improves with increasing molecular size, since adsorption energy increases with molecular chain length. [250]

Previous MD simulations have investigated the effect of organic species on graphite friction. [251-257] Among these studies, simulations suggested that the energy barrier for lateral translation and molecular mobility of benzene and C60 molecules on a graphite basal plane was dependent on the rotational degree of freedom of these species.[255 256, 257] These results suggested that the friction force and energy barrier required for sliding could be attributed to the mobility of molecules present on the graphite surface which is determined by the structure of the species and temperature. However, these studies assumed that the behavior of the molecules could be explained by physisorption, and the possible effects of chemical bonding in the interface were not considered.

In the present study, we performed friction experiments using AFM along with reactive MD simulations of a silica AFM tip sliding on a graphite basal plane in the presence of pentanol and phenol. Phenol ($C_6H_5OH$) is an aromatic compound composed of a hydroxyl group attached to a benzyl ring, and pentanol ($C_5H_{11}OH$) is an aliphatic alcohol with five carbon atoms. The selection of pentanol and phenol for this study enabled investigation of the effect of molecular structure on friction for two broad categories of hydrocarbon derivatives, namely aromatic and linear organic molecules. Friction was measured as a function of load in both AFM experiments and MD simulations. Then, the simulations were used to test hypotheses to explain observed friction differences by calculating parameters including the accumulation of molecules due to physical adsorption near the contact, the registry of atoms relative to the graphite basal plane, the direction of molecular motion on the surface, and chemical bonding between the molecules and the tip. The results show that differences in the chemistry of molecules can affect friction and that the difference can be explained in the terms of covalent bonding between the organic molecules and the tip. Lastly, this bonding is correlated to the force exerted by the contacting bodies and the resulting internal strain within the molecules.

### 4.3.2. Methods

#### *4.3.2.1. AFM Experiments*

A clean graphite surface was produced on a highly-oriented pyrolytic graphite (HOPG) crystal through tape-exfoliation in ambient air. Nanoscale friction tests were performed using an AFM system (Multimode, Bruker, US) with Si probes (CONTV, Bruker, US) in contact mode. The spring constant of the Si probe cantilever was determined with Sader's method.[210] The probe surface had a native silica layer, so it was regarded as a silica probe. The lateral sensitivity of the cantilever in this setup was obtained by comparing the measured lateral signal on a reference sample with a known coefficient of friction (COF). The reference sample was a hydrogenated diamond-like carbon (H-DLC) coating, whose COF was about 0.15 in a pentanol vapor (40% of the saturation pressure) lubrication condition.[258] Before the friction test, the AFM probe was treated with UV/ozone for 15 minutes.[259] During the test, the AFM tip rubbed against the graphite surface in a

reciprocating motion. A region without graphene step edges was selected as the scan area. The stroke length was 200 nm and the frequency was 2.5 Hz, so the relative sliding speed was 1 μm/s. The friction tests were performed in pentanol and phenol vapor environments. For the pentanol environment, a gas stream of pentanol and nitrogen was passed through the AFM chamber at a rate of 50 $cm^3$/min; the partial pressure of pentanol was 80% of its saturation pressure. For the phenol environment, small crystallites of phenol were put inside the AFM chamber to maintain the partial pressure of phenol near the saturation pressure. Friction was measured at applied normal load increases from 6.4 nN to 38.3 nN and all tests were performed at room temperature (around 22°C). The adhesive force measured from pull-off experiments was found to be 30.9 nN in dry $N_2$, 15.0 nN in pentanol vapor and 43.4 nN in phenol vapor. Assuming a tip radius of 120 nm (based on the relative magnitudes of adhesive force with a 2 nm radius tip and the tip used in the friction experiments), the DMT contact model was used to calculate contact pressures of 0.37 - 0.51 GPa in pentanol vapor and 0.50 - 0.59 GPa in phenol vapor. Please note that the experiments presented here were performed by Dr. Zhe Chen and Dr. Seong H. Kim group at Penn State University. [133]

*4.3.2.2. MD Simulations*

To complement the AFM experiments, the friction of an amorphous silica tip apex sliding over the basal plane of a graphite substrate was modeled using reactive MD simulations. The ReaxFF[260] force field used in this work was previously developed for the C/O/H/Si/F system[214] from a combination of parameters for C/H/O [215, 216] and Si/C [217]. Although ReaxFF is known to underestimate the low-temperature reactivity of phenol compared to DFT calculations [261-263], it has been used to explore the chemical interactions between these molecules and other materials including graphite at room temperature [264, 265]. It has been also shown that ReaxFF performs adequately in its representation of graphite compressibility [266]. The amorphization of silica was performed using a heat-quench process which consisted of heating of crystalline cristobalite to 4000 K and then cooling to room temperature at a rate of 0.02 K/fs. [200 75] Based on previous experiments, silica adsorbs organic compounds such as phenol and pentanol when they are available in the environment.[267] To mimic this adsorption while keeping the model size small for computational efficiency, the model tip surface was terminated with methoxy groups. Figure 4.18 illustrates the structure of pentanol (a) and phenol (b) molecules as well as the setup used in simulations (c), including the silica tip, organic molecules and graphite substrate. The simulation was initially assembled by placing the tip at the top of the model system, the graphite substrate at the bottom and 50 pentanol or phenol molecules in the middle. To decrease the computational cost, only a three-layer graphite substrate was considered. The substrate dimensions were 5.0 nm in the sliding direction (x-direction), 4.0 nm perpendicular to the sliding direction on the basal plane (y-direction), and about 1.0 nm normal to the graphite basal plane (z-direction). The amorphous silica tip had a half-disk shape with 3.5 nm radius in the xz-plane and 1.5 nm thickness in the y-direction. Throughout the simulation, the bottom graphene layer was fixed, and the top 0.5 nm of the tip was treated as a rigid body; all other atoms could move freely.

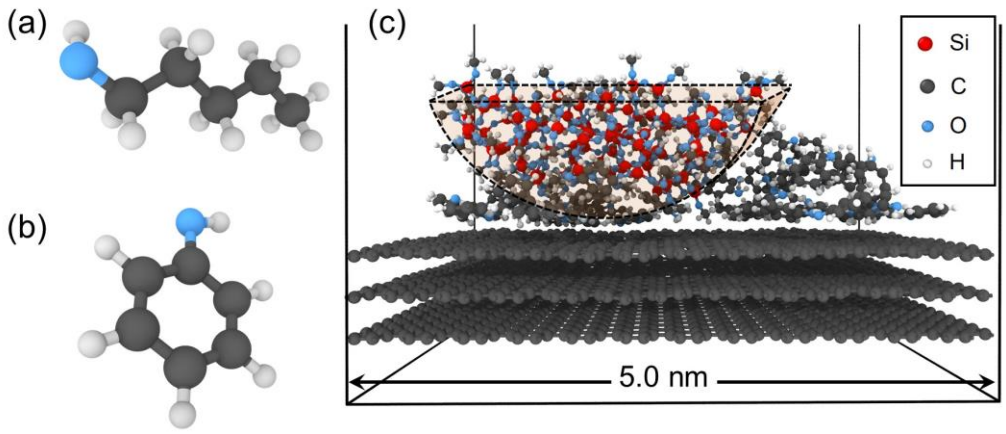


Figure 4.18 Snapshots of (a) pentanol, (b) phenol, and (c) the simulation of friction between a nanoscale silica probe and the basal plane of graphite in the presence of phenol. A second model is the same except phenol molecules are replaced with pentanol. The tip structure (shaded area) is amorphous silica terminated with methoxy groups to mimic a native oxidized silicon tip in the presence of organic molecules.

Each simulation consisted of four steps: i) Energy minimization and initial equilibration until a stable potential energy was reached; ii) Vertical compression of the tip toward the substrate at 10 m/s until the minimum distance between the tip and the substrate reached 0.3 nm; iii) Application of a 10, 30 or 50 nN normal load at the top rigid part of the tip for 120 ps; and iv) Sliding at 10 m/s by pulling the tip with a harmonic spring with a stiffness of 6 N/m. The adhesion force was measured from simulations of pull off tests to be 3.4 nN and 4.3 nN for pentanol and phenol, respectively. Although the model tip was not spherical, the apparent contact area calculated from the size of a rectangle that enclosed all tip atoms within 0.3 nm of the substrate was used to approximate an effective spherical tip radius of 1.6 nm. Then, for the applied normal load range of 10 - 50 nN, the DMT model was used to estimate contact pressures of 5.0 - 8.1 GPa in both pentanol and phenol. Simulations were run in the canonical ensemble with the temperature maintained at 300 K using a Langevin thermostat applied to the unconstrained atoms. Due to the high velocity during the sliding step, the motion of the atoms in the sliding direction was excluded from the temperature calculation used by the thermostat. A 0.25 fs time step and 20 fs thermostat damping factor were used in all simulations. The friction force during sliding was calculated by monitoring the force on the tip atoms in the sliding direction. Throughout the simulations, bonds between atoms were identified as those with a bond order of 0.3 or larger. All the simulations were performed using the large atomic/molecular massively parallel simulation (LAMMPS) code [130], and OVITO software [131] was used to visualize the results.

### 4.3.3. Results and Discussion

Figure 4.19 (a) reports the mean friction force as a function of normal load from AFM experiments performed in pentanol and phenol vapor conditions. These results show that, within the range of applied normal loads tested, there is higher friction between the sliding AFM tip and graphite substrate in phenol compared to pentanol. The standard

deviation (STDEV) of the friction force collected in one scan (512 data points in a trace or retrace scan) is shown in Figure 4.19 (b), and it is also higher for phenol than pentanol. The mean and STDEV of the friction force at different applied normal loads in the MD simulations are shown in Figure 4.19 (c) and Figure 4.19 (d), respectively. In the simulations, the difference between the mean friction forces for pentanol and phenol is not as large as observed in the experiments. However, the STDEV of the friction signal is significantly higher for phenol than pentanol in the simulations. The raw friction data from the simulations with pentanol and phenol at the 10 nN load are shown in Figure 4.20 (a) and Figure 4.20 (b) and illustrate the larger force fluctuations for phenol, particularly after about 2 nm of sliding. It has been previously proposed that the STDEV of the lateral force can be used as a measure of frictional energy dissipation.[268] Therefore, both the mean and STDEV of the force are relevant to the comparison between phenol and pentanol, and, as shown in Figure 4.19, both are larger for phenol in experiments and simulations.

Although simulations and experiments exhibit similar trends, there are differences in magnitudes that are attributable to the substantial differences in the contact size and sliding speed. For example, the smaller STDEV in the experiments can be explained by the significantly larger tip size which makes the system more stable compared to the simulation setup. Also, since atomic-scale friction is known to increase with applied pressure and sliding speed [269, 270], the higher mean friction in the simulations may be partially explained by the much larger pressures and speeds in the simulations compared to the experiments. Nonetheless, the qualitative trends are the same in both AFM and MD results, i.e. both indicate larger mean friction and STDEV for phenol.

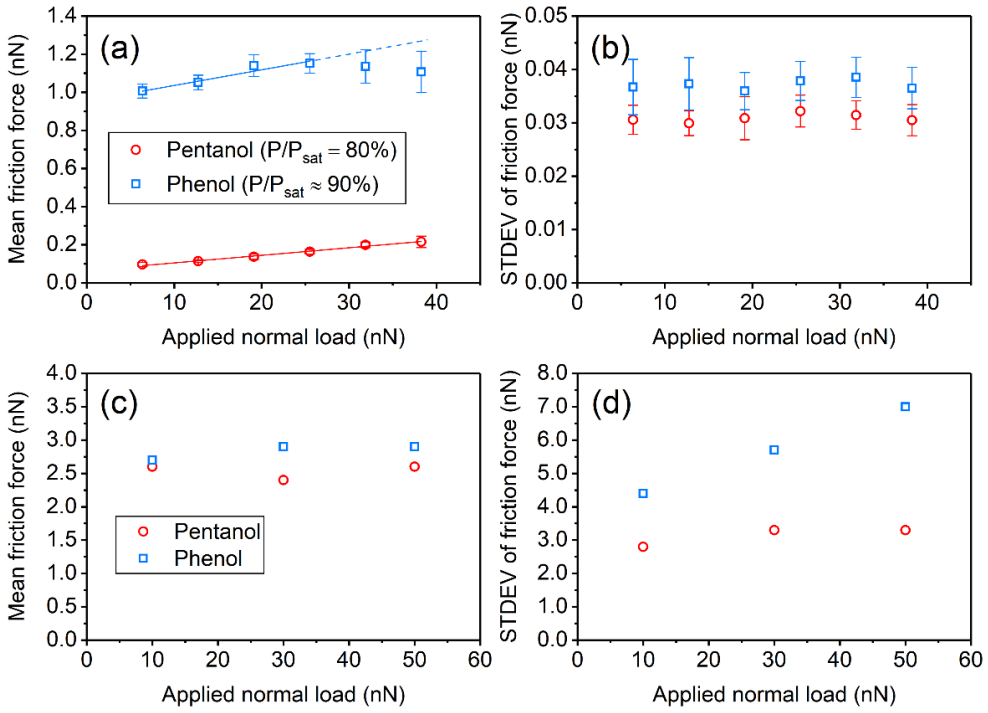


Figure 4.19 Mean (a and c) and standard deviation (b and d) of the friction force for a silica AFM tip sliding on the graphite basal plane in the presence of pentanol and phenol vapor from AFM experiments (a and b) and MD simulations (c and d). The error bars in (a) and

(b) correspond to the deviation across different scans. The experimental results presented here were performed by Dr. Zhe Chen and Dr. Seong H. Kim group at Penn State University. [133]

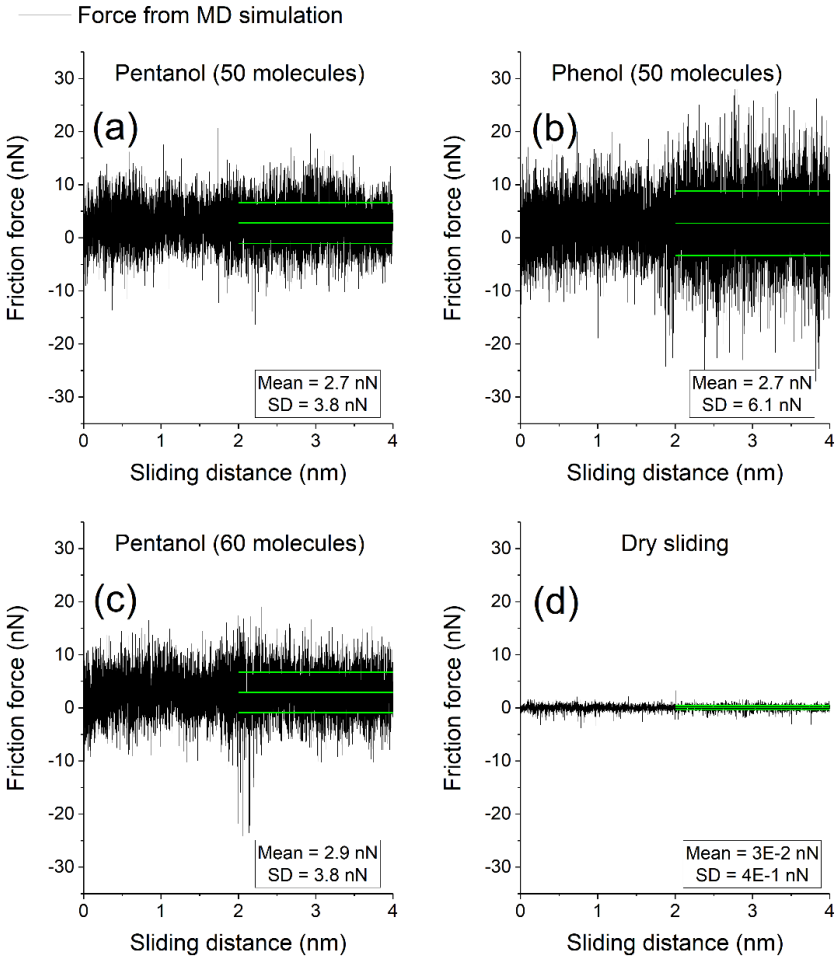


Figure 4.20 Raw friction force data from the simulations for sliding with (a) 50 pentanol molecules, (b) 50 phenol molecules, (c) 60 pentanol molecules and (d) without molecules at 10 nN normal load. The green lines show the mean force and standard deviation. In (b), the friction force fluctuations increase after 2 nm of sliding, indicating that steady-state was achieved after 2 nm.

As a reference, a simulation of dry sliding was performed without molecules; the result was considerably smaller friction force fluctuations (see Figure 4.20 (d)). This indicates that the organic species are directly responsible for the observed friction trends. Also, the simulations at 10 nN load were repeated with 60 pentanol molecules (as opposed to 50) to match the number of carbon atoms in the phenol system, and the same STDEV was obtained, as reported in Figure 4.20 (c). Therefore, the friction difference between phenol and pentanol is attributable to the chemistry of the molecules rather than the number of atoms they contain.

The effect of environment on friction for graphite is typically attributed to physical and chemical adsorption of species at defects such as step edges or vacancies [241, 242, 271, 272]. However, the simulations here describe an ideal graphite basal plane, so those explanations are not applicable in this case. Other hypotheses that might explain the difference between friction with phenol and pentanol are: (i) accumulation of molecules due to physical adsorption at the tip-surface interface [240, 245]; (ii) differences in commensurability between molecular species being dragged inside the contact area with one of the two sliding bodies [237]; or (iii) tribochemical reactions happening at the sliding interface.[273] Each of these hypotheses was tested through the simulations.

To investigate the first hypothesis, the positions of the molecules were analyzed during the sliding simulations. At the beginning of simulation, the molecules were distributed across the surface at a vertical position between the top layer of graphene and the bottom of the tip. During the equilibration step, the molecules approached the surface and physisorbed to the graphite basal plane (Figure 4.21). After the tip was brought into contact and sliding began, these molecules remained on the surface, as shown in the representative snapshots in Figure 4.22. To directly compare phenol and pentanol, the positions of physisorbed carbon atoms along the sliding direction were averaged over the last 2 nm of sliding (the steady-state region, based on trends in Figure 4.20 (b)). As shown in Figure 4.23, there were more carbon atoms in the contact area and in front of the tip with phenol than with pentanol. This difference may contribute to the greater friction observed with phenol.

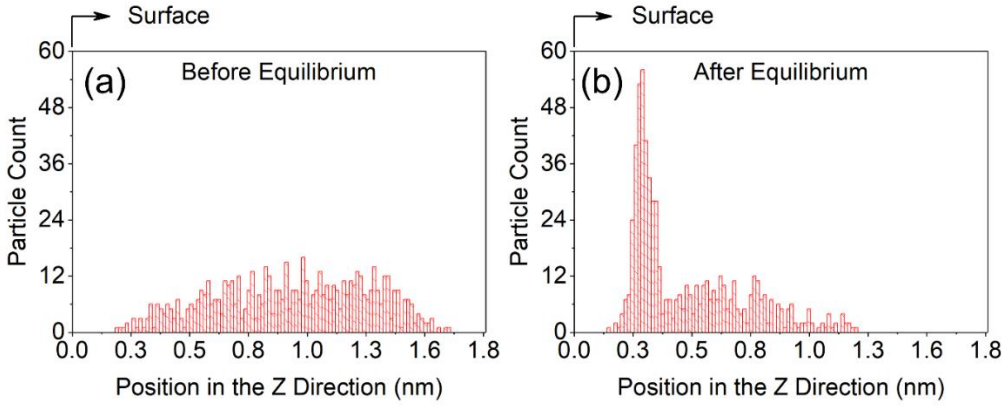


Figure 4.21 The distribution of the vertical (z-direction) position of atoms in the phenol molecules before (a) and after (b) the equilibration step in simulation, where zero corresponds to the position of the topmost graphene layer. The shift in the distribution shows that the molecules move to physisorb on the surface during equilibration.

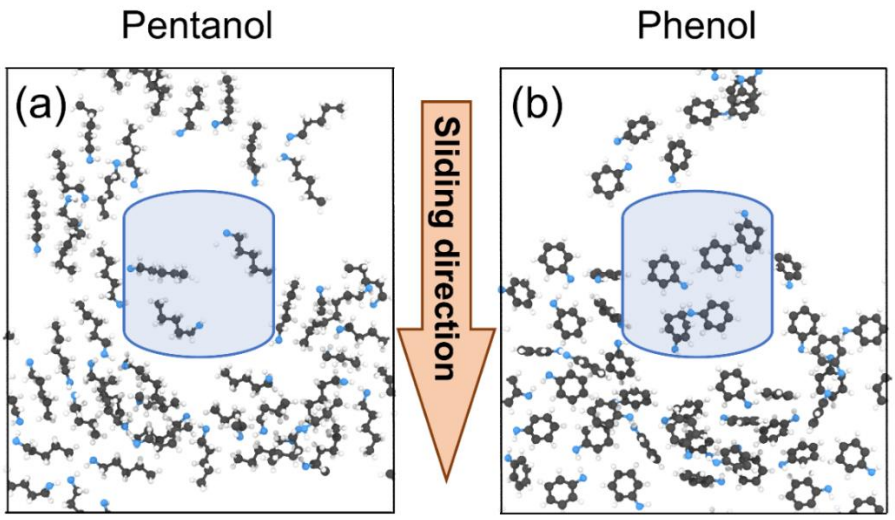


Figure 4.22 Top view snapshots showing the positions of (a) pentanol and (b) phenol molecules physisorbed to the surface after equilibration. The approximate effective contact area, determined based on the shape of the model tip, is shown as a light blue rectangle. More phenol molecules were observed in the contact area between the tip and graphene substrate than pentanol molecules.

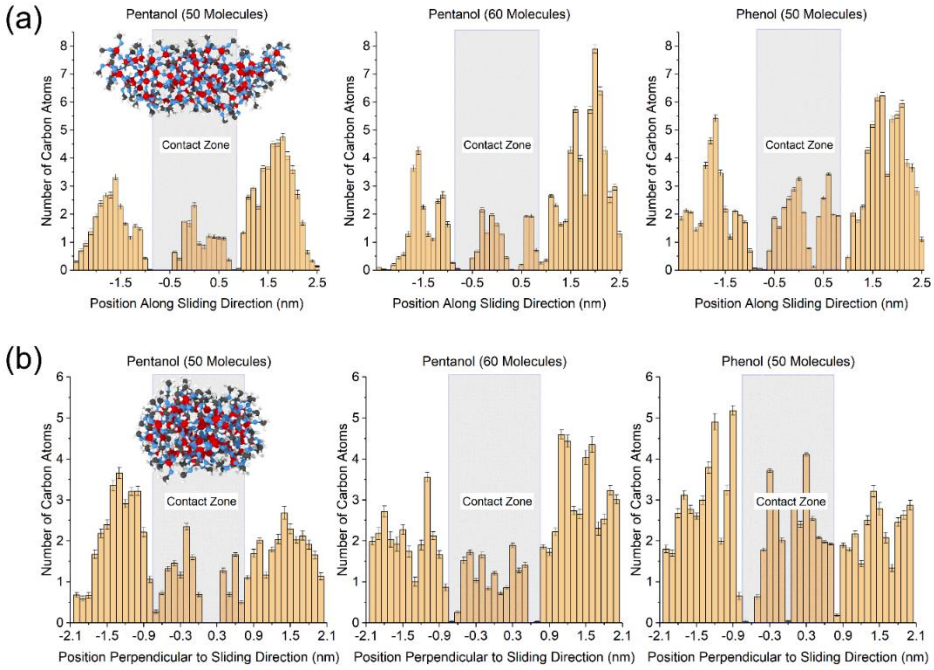


Figure 4.23 Histograms of carbon atoms' positions (a) along sliding direction and (b) in the direction perpendicular to sliding. A snapshot of the tip is shown above the leftmost graphs in each case to illustrate the direction of the distribution relative to the tip and the contact region.

The effect of commensurability was explored by characterizing the registry index (RI) [274, 275] of atoms at the interface. RI is usually employed to study the tribological properties of solid interfaces with different crystal lattices. For example, for a bilayer graphene interface, the most energetically favorable position for a carbon atom is above the middle of the hexagon of carbon atoms in the adjacent layer; this position corresponds to an RI of 0. In the other limiting case, where a carbon atom is directly above another carbon atom in an adjacent layer, the RI is 1. Intermediate positions correspond to RI values between 0 and 1, where a lower RI indicates a more energetically favorable position. Here, the RI was calculated for individual carbon atoms in the molecules relative to the carbon atoms in the graphite basal plane, where a smaller RI corresponds to a greater commensurability between an adsorbate atom and the topmost surface of graphite. The RI values were averaged over the last 2 nm of sliding for both phenol and pentanol. As shown in Figure 4.24 (a), there were more phenol atoms with low RI than pentanol atoms. Based on previous studies [237], atoms with low RI at the interface can act as pinning sites and contribute to friction during the sliding process. The observed difference in RI is unlikely to be due to stronger interactions between the phenol and the surface vs. the pentanol since the pi-pi interactions between the benzene ring and the surface are relatively weak (comparable to thermal energy at room temperature). Further, after normalizing the RI by the total number of carbon atoms in the contact area, as shown in Figure 4.24 (b), no difference between pentanol and phenol molecules was observed. Therefore, there are more pinning sites in the case of phenol, but this is explained by the larger number of molecules in the contact as opposed to the positions of those molecules on the surface.

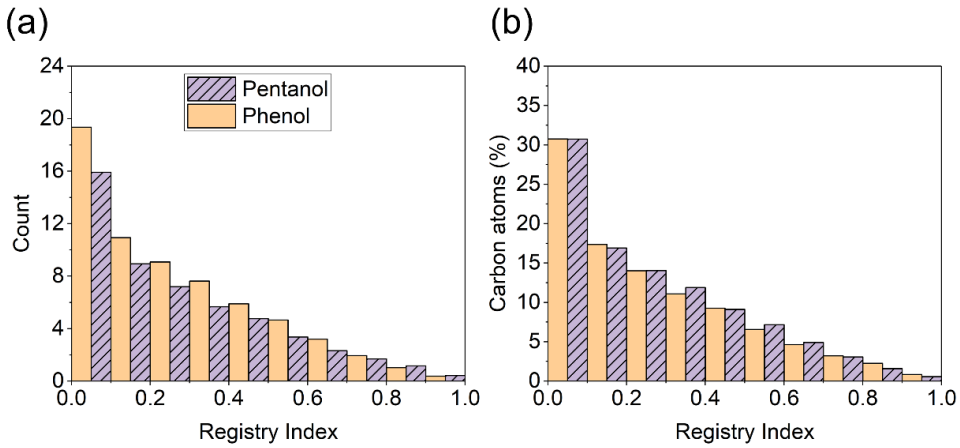


Figure 4.24 (a) Histograms of the RI for carbon atoms in the molecules with respect to carbon atoms on the topmost layer of the graphite averaged over the last 2 nm of sliding. The RI is higher for phenol than pentanol, but this difference is not observed when (b) the data is normalized by the number of atoms in the contact area.

The trajectories of the molecules are illustrated by the positions of the oxygen atoms during sliding in Figure 4.25 and provide information about the motion of pentanol and phenol molecules in the simulation. Comparing two cases, it can be observed that there are many short and inclined trajectories diverging from the sliding direction in the case of pentanol, while there are longer trajectory lines along the sliding direction in the case of

phenol. These observations suggest that pentanol can escape the contact area while phenol molecules are dragged along with the tip. This is consistent with previous experiments [276-278] and classical MD simulations [279, 280] that compared linear to cycloaromatic hydrocarbons and showed that the greater flexibility of the linear hydrocarbons enabled them to more easily slide relative to one another and escape the contact area [280]. However, physical mechanisms may not fully explain the mobility of the phenol and pentanol in our simulations.

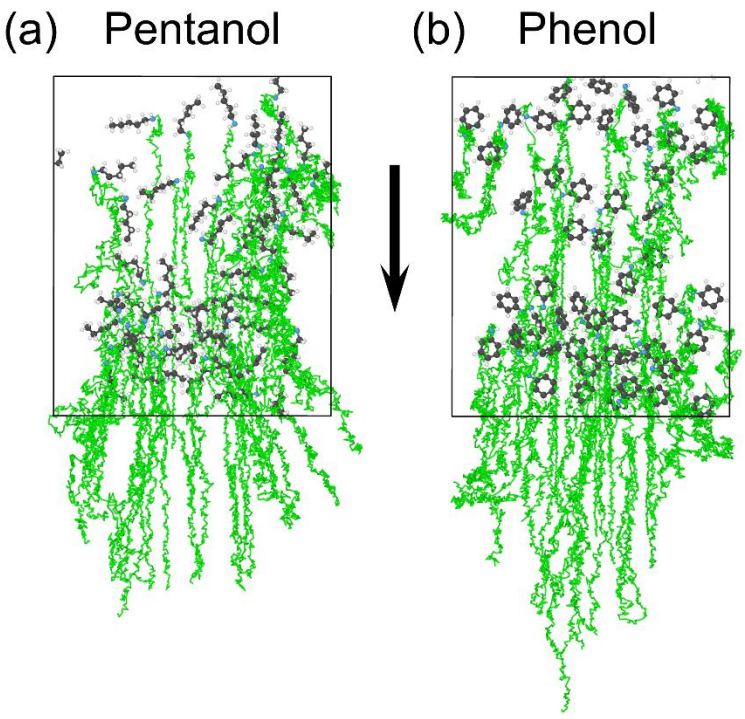


Figure 4.25 Top view of the trajectories of oxygen atoms in (a) pentanol and (b) phenol molecules (indicated by green lines) during the sliding process. The molecules shown in the figures represent their positions before sliding. The trajectories are longer in the sliding direction (arrow in figure) for phenol, indicating that these molecules are being dragged in the contact by the tip, while pentanol molecules can escape out from the sides of the contact.

Although the graphite surfaces remained intact and unreactive throughout the simulations, covalent and hydrogen bonds between the tip and molecules were observed. Snapshots of the simulation illustrating representative bonds that were observed are shown in Figure 4.26. In the case of pentanol, only hydrogen bonds were observed between the molecules and the tip. However, for phenol, we observed $Si_{tip}$-$C_{phenol}$ and $O_{tip}$-$C_{phenol}$ covalent bonds. This observation is not surprising since the aromatic ring in phenol is considerably more reactive than the aliphatic alcohol chain due to activation of the benzene ring by the attached hydroxyl group.[281, 282]

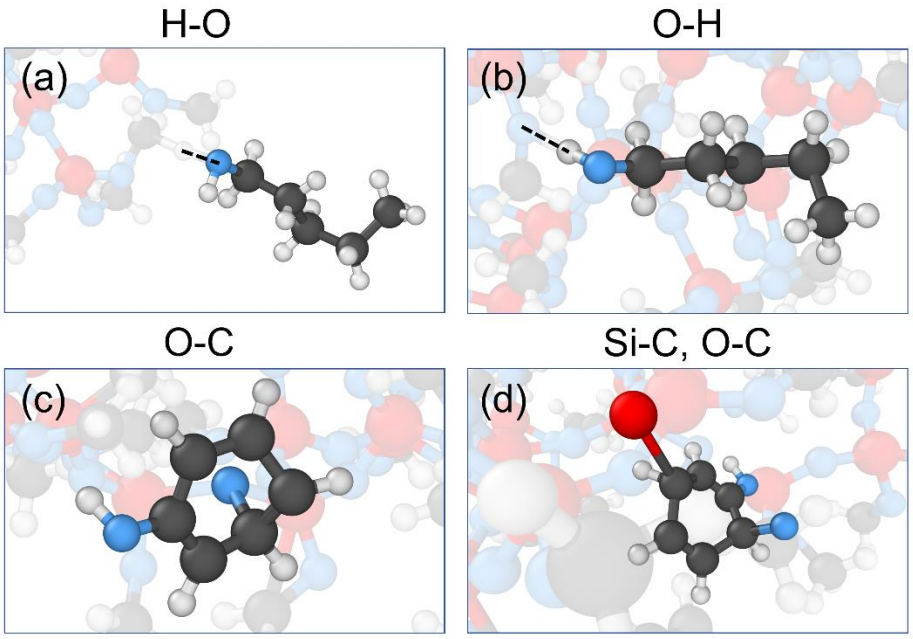


Figure 4.26 Snapshots showing examples of bonding between the molecules and the tip. Pentanol interacts with the tip primarily via hydrogen bonds (a and b) while phenol exhibits covalent bonding with the tip (c and d). All atoms not involved in the bonds being emphasized are shown as faded.

The tip-molecule bonding during the simulation was quantified as the number of bonds vs. time. As shown in Figure 4.27 (a) and Figure 4.27 (b) for the simulations performed at the applied normal load of 10 nN, there were more tip-phenol bonds than tip-pentanol bonds. The pentanol exhibits few and short-duration hydrogen bonds during the simulation while phenol forms $O_{tip}$-$C_{phenol}$ and $Si_{tip}$-$C_{phenol}$ bonds that persist throughout the simulation. To understand this difference, simulations were repeated without load or sliding and with load but no sliding. As shown in Figure 4.27 (c) and Figure 4.27 (e), tip-pentanol bonding was not observed for any load or sliding condition. However, the simulations of phenol with applied normal load only and without load or sliding (Figure 4.27 (d) and Figure 4.27 (f)) showed that covalent bonds were observed only when load was applied. The number of bonds was averaged over the last 0.1 ns of the simulation at all three loads and the results are shown in Figure 4.28. Higher loads did not increase bonding with pentanol but, except for the $O_{tip}$-$C_{phenol}$ bonds at 10 nN, the number of covalent bonds between phenol and the tip increased with load.

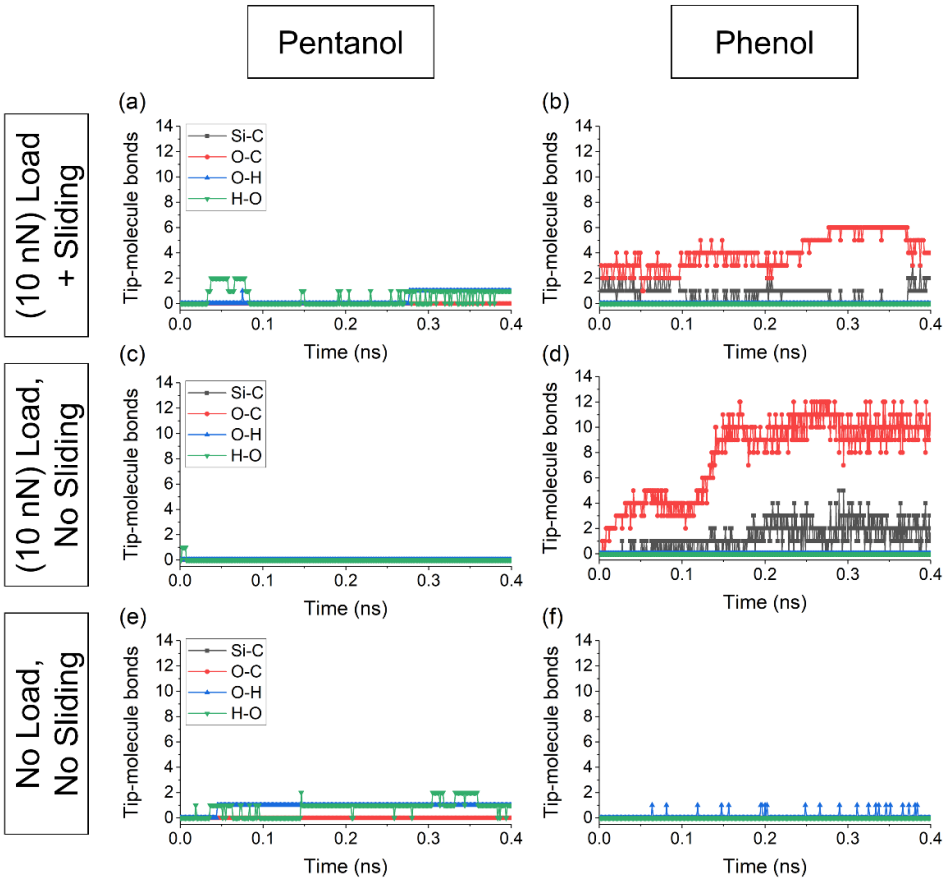


Figure 4.27 Number of bonds between the tip and molecules as a function of time for each atom–atom pair, where the first element corresponds to an atom in the tip and the second is in the molecule, from simulations with 10 nN load and sliding (a and b), 10 nN load only (c and d), and with no load (e and f). Few bonds are observed under any condition with pentanol (a, c, e). However, with phenol, the load and sliding cases (b and d) exhibit bonding, suggesting bond formation is driven by mechanical forces exerted on the molecules in the contact.

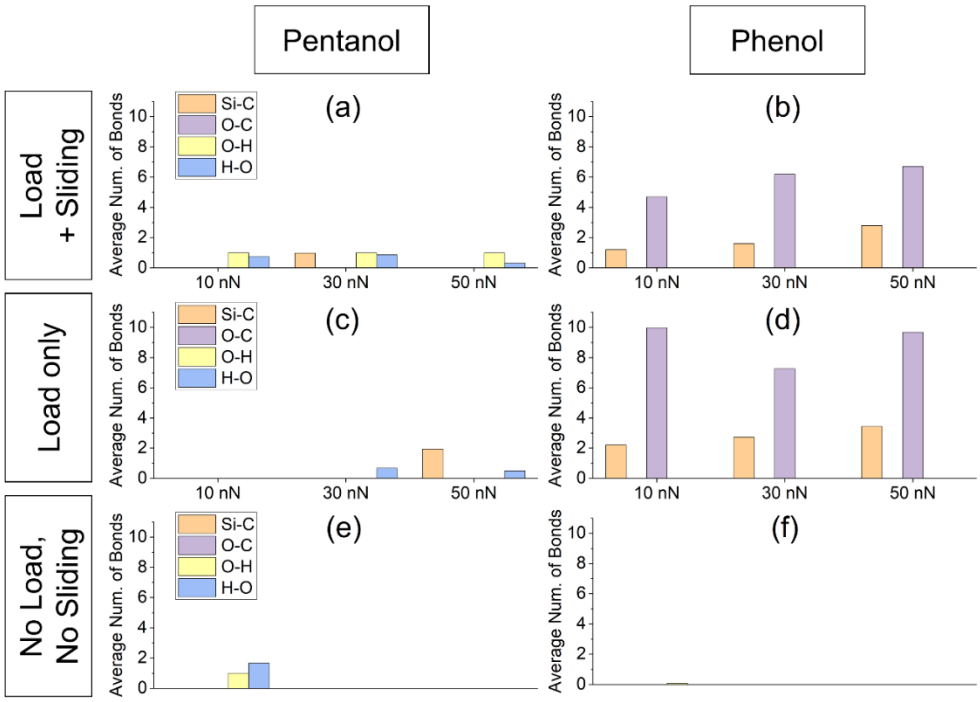


Figure 4.28 Average number of bonds between the tip and molecules averaged over the second half (0.1 ns) of simulations with load and sliding (a and b), load only (c and d), and with no load or sliding (e and f). Few bonds are observed under any condition with pentanol (a, c, e). However, with phenol, the load and sliding cases (b and d) both exhibit bonding, suggesting bond formation is driven by mechanical forces exerted on the molecules in the contact.

The fact that the covalent bonds are only observed when the normal load is applied suggests that the chemical reactions between the tip and phenol molecules are driven by mechanical force in the contact. Both experiments [283] [75] and numerical studies [75, 139, 273] have previously reported mechanochemical reactions during the sliding process. Note that there are more tip-phenol covalent bonds during loading (Figure 4.27 (d)) than during sliding (Figure 4.27 (f)). This can be attributed to the movement of phenol molecules away from the contact during the sliding process, as observed in Movie S1, such that there are fewer opportunities for tip-phenol bonding in the short duration of the simulation. In the case of load only, the molecules are trapped in the contact region where they can then bond with the tip.

To understand how mechanical force drives tip-phenol bonding, the atomic shear strain[189, 190] was quantified as the change in the positions of neighbor atoms within a 0.25 nm radius with respect to their position at the beginning of the equilibrium step. Figure 4.29 (a)-(d) illustrate the shear strain of representative molecules after bonding to the tip during the sliding process; these are the same molecules shown interacting with the tip in Figure 4.26. These snapshots show that pentanol molecules (a and b) experience much less internal strain than phenol molecules (c and d). Also, since phenol-tip bonding was only observed in simulations with load (see Figure 4.27 and Figure 4.28), this result suggests

that the normal load which causes shear strain is responsible for the interfacial bond formation and that this process may be facilitated via deformation of the molecule.

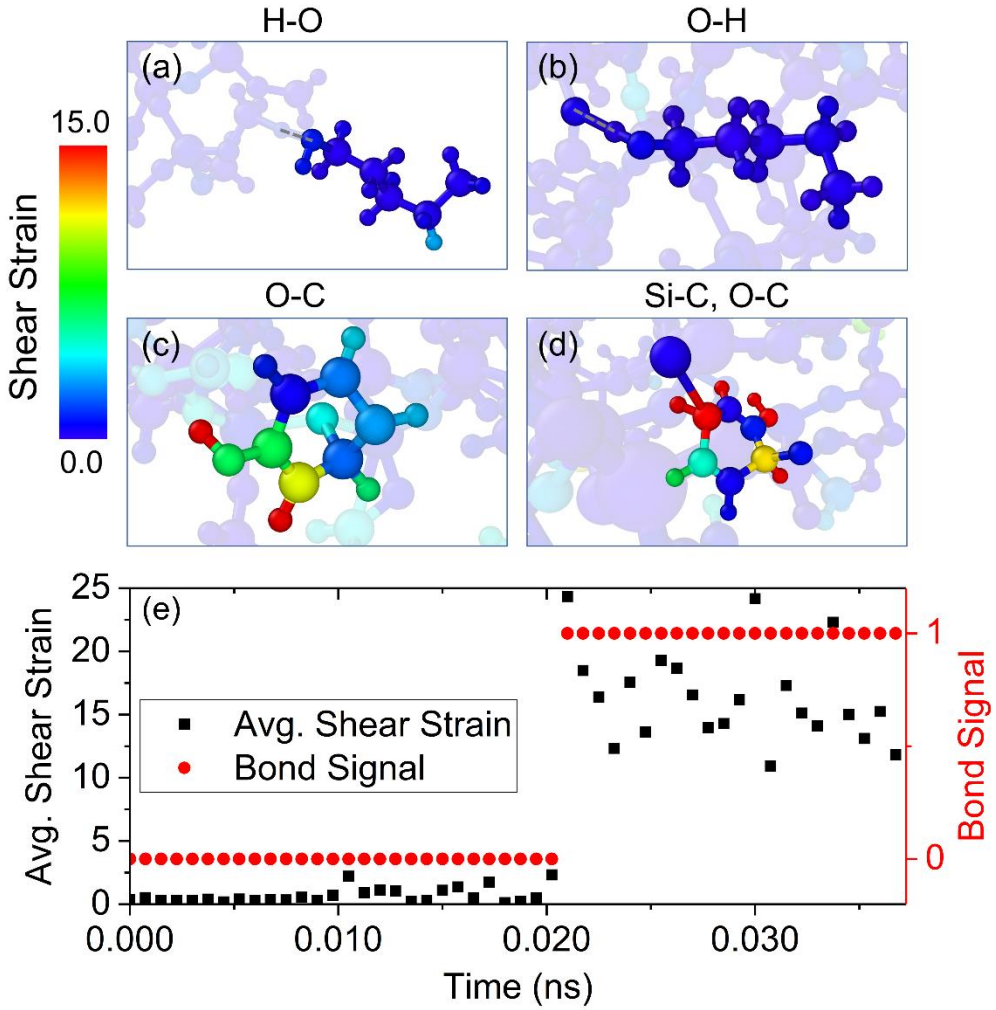


Figure 4.29 (a-d) The atomic shear strain on representative molecules bonded to the tip (same molecules as in Figure 4.26). Pentanol molecules experience negligible shear strain while phenol molecules bonded to the tip experience a significant amount of shear deformation. (e) Shear strain and bond status (0=no bond; 1=bond) for a carbon atom in the aromatic ring of a phenol molecule during the load application step (a 10 nN load is applied at time zero).

To confirm the role of applied load, the atomic shear strain for a carbon atom in a representative phenol molecule was characterized during the load application step. Figure 4.29 (e) shows the change in atomic shear strain and the bond status with time, starting at the point when the normal load is first applied to the tip. Initially, the shear strain on the carbon atom is negligible and is only due to thermal vibration of atoms. Then, the shear strain increases gradually until, at 0.02 ns, it increases rapidly. This moment is coincident with the formation of a covalent bond between the carbon atom in the aromatic ring of

phenol and an oxygen atom in the tip. The other phenol atoms that bond to the tip exhibit similar trends. These findings confirm that the role of applied load is to strain the molecule, which facilitates covalent bond formation. This is consistent with the previous finding reported for mechanochemical reactions of allyl alcohol and α-pinene molecules at tribological interfaces of silicon oxide.[75, 90] Further, since neither strain nor covalent bonding is observed with pentanol, these results show that the susceptibility of a molecule to mechanochemical reactions is dependent on its structure.[38, 284]

The mechanically-driven chemisorption of phenol to the counter-surface is directly related to the observed friction trends. The covalent bonds are strong enough to drag the phenol molecules during sliding (Figure 4.25) which explains the presence of more phenol in the contact area (Figure 4.23) that can act as pinning sites resisting sliding (Figure 4.26). The covalently bonded phenol atoms also increase adhesion, as observed in both simulations and experiments. Taken together, these effects result in larger friction when sliding in a phenol compared to pentanol environment.

### 4.3.4. Conclusion

In the first part of this chapter (4.1), we used reactive MD simulations to study a chemically and topographically well-defined interface between silica and graphite with a single graphene step edge. The experimental and computational friction responses were in agreement and enabled us to provide insight into the atomic-level origins of the friction through exploring atomic-scale simulation results. To this end, we identified separate contributions of physical and chemical processes to be the shear strain applied to the tip due to topographical change and hydrogen bonding between the C-O-H groups on the step edge and the tip, respectively. Both experimental and simulation results showed that the direction of both the applied friction forces originating from H-bonding and shear strain were against sliding during the step-up sliding. However, in the stepping-down process, the force from shear strain was assistive, and the force due to H-bond was resistive. Accordingly, the friction coefficient was separated into two positive COF (resistive) terms that added up during the step-up sliding, whereas there was a positive (resistive) and a negative (assistive) term that canceled out each other during the step-down process. As a result of the different contributions to the friction, both resistive and assistive sliding forces were possible depending on the position of the tip with respect to the step-edge.

In the second part of this chapter (4.2), we explored the effect of step-edge reactivity on friction at the step-edges of graphite. By comparing single-asperity friction at chemically inert and active graphene step edges on the graphite basal plane, the physical and chemical contributions to friction at the nanoscale have been successfully identified. It is found that the friction at an exposed step edge can be reduced in an alcohol vapor, because the adsorbed alcohol molecules can suppress the H-bonding between the step edge and the counter surface. However, even if the chemical contribution to friction is eliminated, because of the anisotropic deformation of the exposed step edge, the friction of an exposed step edge is still higher than that of a buried step edge. More generally, it is demonstrated that, within one cycle of a tip sliding up and down a topographic step, the energy consumed during the step-up process can be restored during the step-down process only if (a) there is no chemical interaction between the tip and the step and (b) the deflection of terminal groups at the step is identical during the step-up and step-down processes.

Otherwise, there will be a net energy loss when shear occurs at a topographically corrugated interface, leading to an increase of friction.

In the last part of this chapter (4.3), we explored the effect of environment on the friction at the basal plane of graphite. We employed AFM experiments and reactive MD simulations to explore the friction behavior of an amorphous silica tip sliding on a graphite basal plane in the presence of phenol and pentanol. The mean and STDEV of the friction force in both simulations and experiments were larger with phenol than pentanol. The STDEV of the friction force was used as a measure of energy dissipation for these two systems. To understand the observed friction trends, the simulations were used to calculate parameters that could affect friction, including the number of atoms in the contact area, the RI of the atoms in the molecules on the graphite surface, the motion of the molecules, and chemical bonding between the molecules and the tip. All of these were found to be different for phenol and pentanol, and the results indicated that there were more phenol molecules in the contact that moved along with the tip and were in registry with the graphite, thereby increasing adhesion and friction. This observation was explained by the presence of covalent bonding between phenol molecules and the tip that was not exhibited with pentanol. Further, simulations performed at different loads showed that phenol-tip bonding was driven by mechanical forces in the contact. The role of applied force was explained by the shear deformation of the phenol molecules. The results illustrate how differences in the structure of organic molecules can affect their susceptibility to strain and therefore mechanochemical bonding in a sliding contact, which in turn affects the number of species in the contact area leading to different friction behavior.

Overall, this study provides insight into the effect of the physical and chemical contributors to the friction both at the step edges and basal plane of graphite. The results revealed that the share of physical and chemical contribution to the friction varies many parameters, including sliding direction, applied load, chemical nature of edge and the tip, and environment. The provided insight into physical and chemical effects on the friction discussed in this study suggested that they might be leveraged to minimize sliding resistance at tribological interfaces and can be used to explain the nanoscale mechanism of friction at larger scales where the sliding surfaces are neither atomically smooth nor chemically inert.

# Chapter 5 : Conclusions

## 5.1. Summary and Future work

In chapter 2, we found that non-hydroxylated surfaces reacted more with a-pinene and had more oligomerization during shear than hydroxylated surfaces. The activation volume was calculated from the pressure dependence of the yield in simulations to explain the role of shear deformation in mechanically driven chemical reactions. The detailed analysis of individual molecules during the simulation revealed that shear facilitates association reactions through the deformation of strained parts of the molecule, which in turn enables the molecule to bond with surface oxygen as the first step towards oligomerization. While the goal of this study was to understand the effect of surface reactivity on the mechanochemical reactions by investigating a simple model system, the more complicated chemical species and surfaces in engineering conditions should not be disregarded. This work can be extended by studying the mechanochemical reactions for other species that contribute to the formation of ZDDP tribofilms[9] on amorphous ferrous surfaces due to applied shear and heat. While several studies have been previously conducted to investigate the formation of ZDDP using quantum calculations[285, 286], to perform the simulations at a larger scale, new reactive forcefield needs to be developed due to the lack of availability of potential for ZDDP. Although the suggested system will be more complex due to the larger number of elements involved, it is directly relevant to real engineering applications. The challenges of studying the suggested complicated systems may be tackled by some simplifications, such as modeling a subset of molecules on the surface or modeling other materials that form tribofilms similar to ZDDP.

In chapter 3, we found several possible reaction pathways for chemisorption of TCP on iron oxide because of the multiple reaction sites on the TCP and irregularity of the amorphous surface. It was also revealed that the relative reactivity of the unique reaction sites on the TCP was temperature dependent. The composition of the material chemisorbed to the surface was then analyzed, which revealed that C was the most prevalent element at any temperature. Also, the most statistically likely chemisorbed species were TCP or cresol, with the former being more prevalent at lower temperatures and the latter more prevalent at higher temperatures. Next, simulations with NDs showed an increase in the number of bonds between TCP and iron oxide, which was consistent with the frequency shift observed at 500 K in QCM experiments with NDs. The analysis of individual chemical bonds in the simulation showed that TCP could bond with the surface both directly and indirectly through adsorption on the surface of NDs. It should be noted that the parallel simulations used in the first part of this study were useful to statistically analyze and detect the most important reactions in a small system consisting of one molecule on a surface at a time and this approach can reduce the computational cost. However, the effect of interactions among the TCP molecules and their effect on the thermal film formation should be explored further. Also, other chemical species, including oxygen, water, and carbon dioxide, are expected in engineering applications, and their effects should be explored. To extend this study, we suggest reactive MD simulations on a larger system composed of several TCP molecules with and without the presence of other molecules such as O2, H2O, and CO2. Also, in addition to the usual statistical analysis, other computational tools, including machine learning and deep learning techniques, can be

employed to discover the most critical contributors to surface adsorption and to predict the adsorption sites on the surface.

In chapter 4, we attributed the large friction during step-up of a silica tip over the exposed graphene step edge to the synergy of physical effects due to topography and chemical effects results from interfacial hydrogen bonding between the H-bonding between the step edge and the tip surface. Based on our findings, during the step-down, the negative topography change produces a force assisting the sliding motion, whereas the chemical bonds between oppositely moving surfaces produce a resistive force. It was also found that the friction at an exposed step edge can be reduced in an alcohol vapor because the adsorbed alcohol molecules suppress the H-bonding between the step edge and the counter surface. We demonstrated that, within one cycle of a tip sliding up and down a topographic step, the energy consumed during the step-up process could be restored only partially due to chemical interaction between the tip and the step and deflection of terminal groups at the step edge. Finally, the friction was found to be different for phenol and pentanol when a silica tip slides on the graphite basal plane. The results indicated more phenol molecules in the contact that moved along with the tip and were in registry with the graphite, thereby increasing adhesion and friction. This observation was explained by the presence of covalent bonding between phenol molecules and the tip that was not exhibited with pentanol. Although the sliding silica tip on the graphite surface is a well-defined surface and allows us to isolate the effect of chemical and physical phenomena on friction behavior, this system is far from reality since the presence of irregularities like surface roughness and amorphous structure on the surface is expected in engineering conditions. Such systems can be explored in future steps to explore the interactions between chemical reactions and surface roughness and their effect on friction. Investigating such a complex system could be challenging but rewarding, and various methods, including machine learning, can be used to identify the most correlated features with friction signals.

## 5.2. Outcomes and Implications

To summarize, the role of chemical reactions in the formation of thermal films and tribofilms, as well as their contribution to the friction at sliding interfaces, was studied using reactive molecular dynamics simulations for various scenarios at surfaces and interfaces. The first study of oligomerization of alpha-pinene between sliding surfaces of hydroxylated and non-hydroxylated silica provided atom-scale explanations for shear-induced mechanochemical reactions, which are an essential element in tribofilm formation. The agreement between the simulations and experimental results and the detailed time evolution information of molecules that simulations provide suggest that reactive molecular dynamics is a powerful tool for studying tribological systems that are hidden between sliding surfaces and difficult to study. In the second study, the formation of a protective film from TCP on amorphous ferrous surfaces was investigated. The results of this study again emphasize the complexity of surface chemical reactions due to interactions between different players, including the involved chemical species, thermal and mechanical parameters. The parallel molecular dynamics simulation and the statistical approach used to characterize reactions in this study can be applied to other systems where organic molecules react with surfaces. The approach is particularly useful for irregular or disordered surfaces which are present in a variety of applications and on which many

possible reactions contribute to surface film formation. In the last study, the effect of chemical and physical interactions between a sliding silica tip on the friction on the step edge and the basal plane of graphite was explored. The fact that physical and chemical factors during the sliding process suggest opportunities to tune the COF with prescribed topographic features and terminating species. While this concept may be impractical in an industrial setting with current technology, a fundamental understanding of the chemical and topographic origins of friction holds great promise for future scientific advances and opens the possibility of tunable friction. This study also pointed to the importance of the environment on the observed friction. The findings have important implications for applications that rely on graphite for lubrication in varying environmental conditions, where chemical and physical factors will contribute to sliding resistance.

## References


1. Holmberg, K.; Andersson, P.; Erdemir, A. J. T. I., Global energy consumption due to friction in passenger cars. **2012,** *47*, 221-234.
2. Bannister, K. E., *Lubrication for industry*. Industrial Press Inc.: 1996.
3. Sloman, E., 40 - Lubrication. In *Plant Engineer's Reference Book (Second Edition)*, Snow, D. A., Ed. Butterworth-Heinemann: Oxford, 2002; pp 40-1-40-46.
4. Sharma, V.; Erdemir, A.; Aswath, P. B., An analytical study of tribofilms generated by the interaction of ashless antiwear additives with ZDDP using XANES and nano-indentation. *Tribology International* **2015,** *82*, 43-57.
5. Ratoi, M.; Niste, V. B.; Walker, J.; Zekonyte, J., Mechanism of Action of WS2 Lubricant Nanoadditives in High-Pressure Contacts. *Tribology Letters* **2013,** *52* (1), 81-91.
6. Heuberger, R.; Rossi, A.; Spencer, N. D., XPS study of the influence of temperature on ZnDTP tribofilm composition. *Tribology Letters* **2007,** *25* (3), 185-196.
7. Hsu, S. M.; Gates, R. S. *Boundary Lubrication and Boundary Lubricating Film| NIST*; 2005.
8. Hsu, S. M. J. M. B., Boundary lubrication of materials. **1991,** *16* (10), 54-58.
9. Spikes, H. J. T. l., The history and mechanisms of ZDDP. **2004,** *17* (3), 469-489.
10. Yin, Z.; Kasrai, M.; Fuller, M.; Bancroft, G. M.; Fyfe, K.; Tan, K. H. J. W., Application of soft X-ray absorption spectroscopy in chemical characterization of antiwear films generated by ZDDP Part I: the effects of physical parameters. **1997,** *202* (2), 172-191.
11. Fujita, H.; Spikes, H. J. P. o. t. I. o. M. E., Part J: Journal of Engineering Tribology, The formation of zinc dithiophosphate antiwear films. **2004,** *218* (4), 265-278.
12. Mosey, N. J.; Müser, M. H.; Woo, T. K. J. S., Molecular mechanisms for the functionality of lubricant additives. **2005,** *307* (5715), 1612-1615.
13. John, S. T.; Song, Y.; Liu, Z. J. T. L., Effects of temperature and pressure on ZDDP. **2007,** *28* (1), 45-49.
14. Zhang, J.; Spikes, H. J. T. L., On the mechanism of ZDDP antiwear film formation. **2016,** *63* (2), 24.
15. Shimizu, Y.; Spikes, H. A., The Influence of Slide–Roll Ratio on ZDDP Tribofilm Formation. *Tribology Letters* **2016,** *64* (2), 19.
16. Tysoe, W. T.; Spencer, N. D. J. T.; Technology, L., Reaction to rubbing. **2015,** *71* (8), 84.
17. Mohammadtabar, K.; Eder, S. J.; Dörr, N.; Martini, A., Heat-, Load-, and Shear-Driven Reactions of Di-tert-butyl Disulfide on Fe(100). *The Journal of Physical Chemistry C* **2019,** *123* (32), 19688-19692.
18. Martini, A.; Eder, S. J.; Dörr, N. J. L., Tribochemistry: A Review of Reactive Molecular Dynamics Simulations. **2020,** *8* (4), 44.
19. James, S. L.; Adams, C. J.; Bolm, C.; Braga, D.; Collier, P.; Friščić, T.; Grepioni, F.; Harris, K. D.; Hyett, G.; Jones, W. J. C. S. R., Mechanochemistry: opportunities for new and cleaner synthesis. **2012,** *41* (1), 413-447.
20. Tian, Y.; Boulatov, R., Comparison of the predictive performance of the Bell–Evans, Taylor-expansion and statistical-mechanics models of mechanochemistry. *Chemical Communications* **2013,** *49* (39), 4187-4189.
21. Ribas-Arino, J.; Marx, D. J. C. r., Covalent mechanochemistry: theoretical concepts and computational tools with applications to molecular nanomechanics. **2012,** *112* (10), 5412-5487.
22. Makarov, D. E. J. T. J. o. c. p., Perspective: mechanochemistry of biological and synthetic molecules. **2016,** *144* (3), 030901.

23. Chen, L.; Wen, J.; Zhang, P.; Yu, B.; Chen, C.; Ma, T.; Lu, X.; Kim, S. H.; Qian, L., Nanomanufacturing of silicon surface with a single atomic layer precision via mechanochemical reactions. *Nature Communications* **2018,** *9* (1), 1542.
24. Gosvami, N.; Bares, J.; Mangolini, F.; Konicek, A.; Yablon, D.; Carpick, R. J. S., Mechanisms of antiwear tribofilm growth revealed in situ by single-asperity sliding contacts. **2015,** *348* (6230), 102-106.
25. Jacobs, T. D.; Carpick, R. W., Nanoscale wear as a stress-assisted chemical reaction. *Nature nanotechnology* **2013,** *8* (2), 108-112.
26. Jacobs, T. D.; Gotsmann, B.; Lantz, M. A.; Carpick, R. W., On the application of transition state theory to atomic-scale wear. *Tribology letters* **2010,** *39* (3), 257-271.
27. Vahdat, V.; Ryan, K. E.; Keating, P. L.; Jiang, Y.; Adiga, S. P.; Schall, J. D.; Turner, K. T.; Harrison, J. A.; Carpick, R. W., Atomic-scale wear of amorphous hydrogenated carbon during intermittent contact: a combined study using experiment, simulation, and theory. *Acs Nano* **2014,** *8* (7), 7027-7040.
28. Felts, J. R.; Oyer, A. J.; Hernández, S. C.; Whitener Jr, K. E.; Robinson, J. T.; Walton, S. G.; Sheehan, P. E. J. N. c., Direct mechanochemical cleavage of functional groups from graphene. **2015,** *6*, 6467.
29. Hibi, Y.; Enomoto, Y., Mechanochemical reaction and relationship to tribological response of silicon nitride in n-alcohol. *Wear* **1999,** *231* (2), 185-194.
30. Li, T. Q.; Zhang, M. Q.; Song, L.; Zeng, H. M., Friction induced mechanochemical and mechanophysical changes in high performance semicrystalline polymer. *Polymer* **1999,** *40* (16), 4451-4458.
31. He, X.; Kim, S. H., Surface Chemistry Dependence of Mechanochemical Reaction of Adsorbed Molecules□ An Experimental Study on Tribopolymerization of α-Pinene on Metal, Metal Oxide, and Carbon Surfaces. *Langmuir* **2018,** *34* (7), 2432-2440.
32. Chen, L.; He, H.; Wang, X.; Kim, S. H.; Qian, L., Tribology of Si/SiO2 in Humid Air: Transition from Severe Chemical Wear to Wearless Behavior at Nanoscale. *Langmuir* **2015,** *31* (1), 149-156.
33. Liu, Z.; Gong, J.; Xiao, C.; Shi, P.; Kim, S. H.; Chen, L.; Qian, L., Temperature-Dependent Mechanochemical Wear of Silicon in Water: The Role of Si–OH Surfacial Groups. *Langmuir* **2019,** *35* (24), 7735-7743.
34. Guo, S.; Xu, X., Effect of Mechanochemical Degradation on Rheological Behavior of PVC. *Polymer-Plastics Technology and Engineering* **1994,** *33* (5), 605-614.
35. Huang, Z.-q.; Tong, Z.-f.; Li, X.-h.; Ye, S.-f.; Pan, L.-p.; Qin, X.-j. J. J. o. C. E. o. C. U., Effects of mechanical activation on cold-water-solubility and rheological properties of cassava starch. **2006,** *20* (3), 449.
36. Ganglani, M.; Torkelson, J. M.; Carr, S. H.; Khait, K., Trace levels of mechanochemical effects in pulverized polyolefins. *Journal of Applied Polymer Science* **2001,** *80* (4), 671-679.
37. Spikes, H. J. F., Stress-augmented thermal activation: Tribology feels the force. **2018,** *6* (1), 1-31.
38. He, X.; Kim, S. H., Mechanochemistry of Physisorbed Molecules at Tribological Interfaces: Molecular Structure Dependence of Tribochemical Polymerization. *Langmuir* **2017,** *33* (11), 2717-2724.
39. Mate, C. M. J. I. J. o. R.; Development, Force microscopy studies of the molecular origins of friction and lubrication. **1995,** *39* (6), 617-627.
40. Feldman, K.; Fritz, M.; Hähner, G.; Marti, A.; Spencer, N. D. J. T. i., Surface forces, surface chemistry and tribology. **1998,** *31* (1-3), 99-105.
41. Bhushan, B.; Israelachvili, J. N.; Landman, U. J. N., Nanotribology: friction, wear and lubrication at the atomic scale. **1995,** *374* (6523), 607.

42. Goertz, M. P.; Moore, N. W., Mechanics of soft interfaces studied with displacement-controlled scanning force microscopy. *Progress in Surface Science* **2010,** *85* (9), 347-397.
43. Rai, Y.; Neville, A.; Morina, A., Transient processes of MoS2 tribofilm formation under boundary lubrication. **2016,** *28* (7), 449-471.
44. Paolicelli, G.; Tripathi, M.; Corradini, V.; Candini, A.; Valeri, S., Nanoscale frictional behavior of graphene on SiO2and Ni(111) substrates. *Nanotechnology* **2015,** *26* (5), 055703.
45. Geng, Y.; Yan, Y.; He, Y.; Hu, Z., Investigation on friction behavior and processing depth prediction of polymer in nanoscale using AFM probe-based nanoscratching method. *Tribology International* **2017,** *114*, 33-41.
46. Ingole, S.; Charanpahari, A.; Kakade, A.; Umare, S. S.; Bhatt, D. V.; Menghani, J., Tribological behavior of nano TiO2 as an additive in base oil. *Wear* **2013,** *301* (1), 776-785.
47. Gangopadhyay, A.; Sinha, K.; Uy, D.; McWatt, D. G.; Zdrodowski, R. J.; Simko, S. J., Friction, Wear, and Surface Film Formation Characteristics of Diamond-Like Carbon Thin Coating in Valvetrain Application. *Tribology Transactions* **2010,** *54* (1), 104-114.
48. Minfray, C.; Martin, J.; Esnouf, C.; Le Mogne, T.; Kersting, R.; Hagenhoff, B. J. T. S. F., A multi-technique approach of tribofilm characterisation. **2004,** *447*, 272-277.
49. Martin, J.-M.; Grossiord, C.; Le Mogne, T.; Igarashi, J., Transfer films and friction under boundary lubrication. *Wear* **2000,** *245* (1), 107-115.
50. Minfray, C.; Martin, J. M.; De Barros, M. I.; Mogne, T. L.; Kersting, R.; Hagenhoff, B., Chemistry of ZDDP Tribofilm by ToF-SIMS. *Tribology Letters* **2004,** *17* (3), 351-357.
51. Buckley, D. H. J. A. T., Friction induced surface activity of some simple organic chlorides and hydrocarbons with iron. **1974,** *17* (1), 36-43.
52. Hsu, S. M.; Klaus, E. E., Estimation of the Molecular Junction Temperatures in Four-Ball Contacts by Chemical Reaction Rate Studies. *A S L E Transactions* **1978,** *21* (3), 201-210.
53. Martin, J.; Mansot, J.; Berbezier, I.; Belin, M.; Balossier, G. J. W., Microstructural aspects of lubricated mild wear with zinc dialkyldithiophosphate. **1986,** *107* (4), 355-366.
54. Rossi, A.; Eglin, M.; Piras, F. M.; Matsumoto, K.; Spencer, N. J. W., Surface analytical studies of surface-additive interactions, by means of in situ and combinatorial approaches. **2004,** *256* (6), 578-584.
55. Martin, J. M. J. T. l., Antiwear mechanisms of zinc dithiophosphate: a chemical hardness approach. **1999,** *6* (1), 1-8.
56. Martin, J. M.; Grossiord, C.; Le Mogne, T.; Bec, S.; Tonck, A. J. T. i., The two-layer structure of Zndtp tribofilms: Part I: AES, XPS and XANES analyses. **2001,** *34* (8), 523-530.
57. Martin, J. J. J. J. o. T., Lubricant additives and the chemistry of rubbing surfaces: metal dithiophosphates triboreaction films revisited. **1997,** *42* (9), 1095.
58. Minfray, C.; Le Mogne, T.; Martin, J.-M.; Onodera, T.; Nara, S.; Takahashi, S.; Tsuboi, H.; Koyama, M.; Endou, A.; Takaba, H.; Kubo, M.; Del Carpio, C. A.; Miyamoto, A., Experimental and Molecular Dynamics Simulations of Tribochemical Reactions with ZDDP: Zinc Phosphate–Iron Oxide Reaction. *Tribology Transactions* **2008,** *51* (5), 589-601.
59. Philippon, D.; De Barros-Bouchet, M. I.; Lerasle, O.; Le Mogne, T.; Martin, J. M., Experimental Simulation of Tribochemical Reactions Between Borates Esters and Steel Surface. *Tribology Letters* **2011,** *41* (1), 73-82.
60. Ghanbarzadeh, A.; Parsaeian, P.; Morina, A.; Wilson, M. C.; van Eijk, M. C.; Nedelcu, I.; Dowson, D.; Neville, A. J. T. L., A semi-deterministic wear model considering the effect of zinc dialkyl dithiophosphate tribofilm. **2016,** *61* (1), 12.
61. Ghanbarzadeh, A.; Wilson, M.; Morina, A.; Dowson, D.; Neville, A. J. T. I., Development of a new mechano-chemical model in boundary lubrication. **2016,** *93*, 573-582.
62. Fuller, M.; Yin, Z.; Kasrai, M.; Bancroft, G. M.; Yamaguchi, E. S.; Ryason, P. R.; Willermet, P. A.; Tan, K. H. J. T. I., Chemical characterization of tribochemical and thermal films

generated from neutral and basic ZDDPs using X-ray absorption spectroscopy. **1997,** *30* (4), 305-315.
63. Gosvami, N. N.; Ma, J.; Carpick, R. W., An In Situ Method for Simultaneous Friction Measurements and Imaging of Interfacial Tribochemical Film Growth in Lubricated Contacts. *Tribology Letters* **2018,** *66* (4), 154.
64. Dorgham, A.; Parsaeian, P.; Azam, A.; Wang, C.; Morina, A.; Neville, A., Single-asperity study of the reaction kinetics of P-based triboreactive films. *Tribology International* **2019,** *133*, 288-296.
65. Bockstedte, M.; Kley, A.; Neugebauer, J.; Scheffler, M., Density-functional theory calculations for poly-atomic systems: electronic structure, static and elastic properties and ab initio molecular dynamics. *Computer Physics Communications* **1997,** *107* (1), 187-222.
66. Rapaport, D. C.; Rapaport, D. C. R., *The art of molecular dynamics simulation*. Cambridge university press: 2004.
67. Voter, A. F., Introduction to the kinetic Monte Carlo method. In *Radiation effects in solids*, Springer: 2007; pp 1-23.
68. Burke, K., Perspective on density functional theory. *The Journal of Chemical Physics* **2012,** *136* (15), 150901.
69. Mardirossian, N.; Head-Gordon, M., Thirty years of density functional theory in computational chemistry: an overview and extensive assessment of 200 density functionals. *Molecular Physics* **2017,** *115* (19), 2315-2372.
70. Battaile, C. C.; Srolovitz, D. J. J. A. R. o. M. R., Kinetic Monte Carlo simulation of chemical vapor deposition. **2002,** *32* (1), 297-319.
71. Onodera, T.; Kawasaki, K.; Nakakawaji, T.; Higuchi, Y.; Ozawa, N.; Kurihara, K.; Kubo, M. J. T. J. o. P. C. C., Effect of tribochemical reaction on transfer-film formation by poly (tetrafluoroethylene). **2014,** *118* (22), 11820-11826.
72. Mosey, N. J.; Woo, T. K. J. I. c., Formation of zinc phosphate polymers and networks through the insertion of metathiophosphates into zinc dialkyldithiophosphates. **2005,** *44* (21), 7274-7276.
73. Osei-Agyemang, E.; Berkebile, S.; Martini, A., Decomposition Mechanisms of Anti-wear Lubricant Additive Tricresyl Phosphate on Iron Surfaces Using DFT and Atomistic Thermodynamic Studies. *Tribology Letters* **2018,** *66* (1), 48.
74. Luo, Y.; Maeda, S.; Ohno, K. J. T. J. o. P. C. A., DFT study on isomerization and decomposition of cuprous dialkyldithiophosphate and its reaction with alkylperoxy radical. **2008,** *112* (25), 5720-5726.
75. Khajeh, A.; He, X.; Yeon, J.; Kim, S. H.; Martini, A., Mechanochemical Association Reaction of Interfacial Molecules Driven by Shear. *Langmuir* **2018,** *34* (21), 5971-5977.
76. Yue, D.-C.; Ma, T.-B.; Hu, Y.-Z.; Yeon, J.; van Duin, A. C.; Wang, H.; Luo, J. J. T. J. o. P. C. C., Tribochemistry of phosphoric acid sheared between quartz surfaces: a reactive molecular dynamics study. **2013,** *117* (48), 25604-25614.
77. Erdemir, A.; Ramirez, G.; Eryilmaz, O. L.; Narayanan, B.; Liao, Y.; Kamath, G.; Sankaranarayanan, S. K. R. S., Carbon-based tribofilms from lubricating oils. *Nature* **2016,** *536* (7614), 67-71.
78. Li, X.; Wang, A.; Lee, K.-R., Role of unsaturated hydrocarbon lubricant on the friction behavior of amorphous carbon films from reactive molecular dynamics study. *Computational Materials Science* **2019,** *161*, 1-9.
79. Yue, D.-C.; Ma, T.-B.; Hu, Y.-Z.; Yeon, J.; van Duin, A. C. T.; Wang, H.; Luo, J., Tribochemical Mechanism of Amorphous Silica Asperities in Aqueous Environment: A Reactive Molecular Dynamics Study. *Langmuir* **2015,** *31* (4), 1429-1436.

80. van Duin, A. C. T.; Dasgupta, S.; Lorant, F.; Goddard, W. A., ReaxFF: A Reactive Force Field for Hydrocarbons. *The Journal of Physical Chemistry A* **2001,** *105* (41), 9396-9409.
81. Brenner, D. W.; Shenderova, O. A.; Harrison, J. A.; Stuart, S. J.; Ni, B.; Sinnott, S. B., A second-generation reactive empirical bond order (REBO) potential energy expression for hydrocarbons. *Journal of Physics: Condensed Matter* **2002,** *14* (4), 783-802.
82. Stuart, S. J.; Tutein, A. B.; Harrison, J. A. J. T. J. o. c. p., A reactive potential for hydrocarbons with intermolecular interactions. **2000,** *112* (14), 6472-6486.
83. Yu, J.; Sinnott, S. B.; Phillpot, S. R. J. P. R. B., Charge optimized many-body potential for the Si⁄SiO 2 system. **2007,** *75* (8), 085311.
84. Shan, T.-R.; Devine, B. D.; Hawkins, J. M.; Asthagiri, A.; Phillpot, S. R.; Sinnott, S. B. J. P. R. B., Second-generation charge-optimized many-body potential for Si/SiO 2 and amorphous silica. **2010,** *82* (23), 235302.
85. Senftle, T. P.; Hong, S.; Islam, M. M.; Kylasa, S. B.; Zheng, Y.; Shin, Y. K.; Junkermeier, C.; Engel-Herbert, R.; Janik, M. J.; Aktulga, H. M. J. n. C. M., The ReaxFF reactive force-field: development, applications and future directions. **2016,** *2* (1), 1-14.
86. Loehlé, S.; Righi, M. J. L., Ab initio molecular dynamics simulation of tribochemical reactions involving phosphorus additives at sliding iron interfaces. **2018,** *6* (2), 31.
87. Righi, M. C.; Loehlé, S.; de Barros Bouchet, M.; Philippon, D.; Martin, J. J. R. A., Trimethyl-phosphite dissociative adsorption on iron by combined first-principle calculations and XPS experiments. **2015,** *5* (122), 101162-101168.
88. Adams, H. L.; Garvey, M. T.; Ramasamy, U. S.; Ye, Z.; Martini, A.; Tysoe, W. T. J. T. J. o. P. C. C., Shear-induced mechanochemistry: pushing molecules around. **2015,** *119* (13), 7115-7123.
89. Loehle, S. Understanding of adsorption mechanism and tribological behaviors of C18 fatty acids on iron-based surfaces: a molecular simulation approach. Ecully, Ecole centrale de Lyon, 2014.
90. Yeon, J.; He, X.; Martini, A.; Kim, S. H., Mechanochemistry at Solid Surfaces: Polymerization of Adsorbed Molecules by Mechanical Shear at Tribological Interfaces. *ACS Applied Materials & Interfaces* **2017,** *9* (3), 3142-3148.
91. Perez, D.; Uberuaga, B. P.; Shim, Y.; Amar, J. G.; Voter, A. F., Chapter 4 Accelerated Molecular Dynamics Methods: Introduction and Recent Developments. In *Annual Reports in Computational Chemistry*, Wheeler, R. A., Ed. Elsevier: 2009; Vol. 5, pp 79-98.
92. Martini, A.; Dong, Y.; Perez, D.; Voter, A. F., Low-Speed Atomistic Simulation of Stick–Slip Friction using Parallel Replica Dynamics. *Tribology Letters* **2009,** *36* (1), 63-68.
93. Claude Le, B.; Tony, L.; Mitchell, L.; Danny, P., A mathematical formalization of the parallel replica dynamics. *Monte Carlo Methods and Applications* **2012,** *18* (2), 119-146.
94. Yeon, J.; Adams, H. L.; Junkermeier, C. E.; Van Duin, A. C.; Tysoe, W. T.; Martini, A. J. T. J. o. P. C. B., Development of a ReaxFF force field for Cu/S/C/H and reactive MD simulations of methyl thiolate decomposition on Cu (100). **2017,** *122* (2), 888-896.
95. Najman, M.; Kasrai, M.; Bancroft, G. J. T. L., Chemistry of antiwear films from ashless thiophosphate oil additives. **2004,** *17* (2), 217-229.
96. Aktary, M.; McDermott, M. T.; McAlpine, G. A. J. T. l., Morphology and nanomechanical properties of ZDDP antiwear films as a function of tribological contact time. **2002,** *12* (3), 155-162.
97. Ma, H.; Li, J.; Chen, H.; Zuo, G.; Yu, Y.; Ren, T.; Zhao, Y. J. T. i., XPS and XANES characteristics of tribofilms and thermal films generated by two P-and/or S-containing additives in water-based lubricant. **2009,** *42* (6), 940-945.
98. Coy, R.; Jones, R. J. A. t., The thermal degradation and EP performance of zinc dialkyldithiophosphate additives in white oil. **1981,** *24* (1), 77-90.

99. Aktary, M.; McDermott, M. T.; Torkelson, J. J. W., Morphological evolution of films formed from thermooxidative decomposition of ZDDP. **2001,** *247* (2), 172-179.
100. Khaled, K.; Amin, M. A. J. C. S., Corrosion monitoring of mild steel in sulphuric acid solutions in presence of some thiazole derivatives–molecular dynamics, chemical and electrochemical studies. **2009,** *51* (9), 1964-1975.
101. Mohammadtabar, K.; Eder, S. J.; Bedolla, P. O.; Dörr, N.; Martini, A. J. L., Reactive molecular dynamics simulations of thermal film growth from di-tert-butyl disulfide on an Fe (100) surface. **2018,** *34* (51), 15681-15688.
102. Chia, C.-L.; Avendaño, C.; Siperstein, F. R.; Filip, S. J. L., Liquid Adsorption of Organic Compounds on Hematite α-Fe2O3 Using ReaxFF. **2017,** *33* (42), 11257-11263.
103. Gao, G. T.; Mikulski, P. T.; Harrison, J. A., Molecular-Scale Tribology of Amorphous Carbon Coatings: Effects of Film Thickness, Adhesion, and Long-Range Interactions. *Journal of the American Chemical Society* **2002,** *124* (24), 7202-7209.
104. Schall, J. D.; Gao, G.; Harrison, J. A., Effects of Adhesion and Transfer Film Formation on the Tribology of Self-Mated DLC Contacts. *The Journal of Physical Chemistry C* **2010,** *114* (12), 5321-5330.
105. Pastewka, L.; Moser, S.; Moseler, M., Atomistic Insights into the Running-in, Lubrication, and Failure of Hydrogenated Diamond-Like Carbon Coatings. *Tribology Letters* **2010,** *39* (1), 49-61.
106. Glosli, J. N.; McClelland, G. M. J. P. r. l., Molecular dynamics study of sliding friction of ordered organic monolayers. **1993,** *70* (13), 1960.
107. Kong, Y.; ALEJANDRE, D. T.; Physics, J. J. M., The molecular dynamics simulation of boundary-layer lubrication. **1997,** *92* (1), 7-18.
108. Chandross, M.; Grest, G. S.; Stevens, M. J. J. L., Friction between alkylsilane monolayers: Molecular simulation of ordered monolayers. **2002,** *18* (22), 8392-8399.
109. Zhang, L.; Leng, Y.; Jiang, S. J. L., Tip-based hybrid simulation study of frictional properties of self-assembled monolayers: effects of chain length, terminal group, scan direction, and scan velocity. **2003,** *19* (23), 9742-9747.
110. Chen, J.; Ratera, I.; Park, J. Y.; Salmeron, M. J. P. r. l., Velocity dependence of friction and hydrogen bonding effects. **2006,** *96* (23), 236102.
111. Kapila, V.; Deymier, P. A.; Raghavan, S. J. M.; Science, S. i. M.; Engineering, Molecular dynamics simulations of friction between alkylsilane monolayers. **2006,** *14* (2), 283.
112. Ewen, J. P.; Gattinoni, C.; Morgan, N.; Spikes, H. A.; Dini, D. J. L., Nonequilibrium molecular dynamics simulations of organic friction modifiers adsorbed on iron oxide surfaces. **2016,** *32* (18), 4450-4463.
113. Briscoe, B.; Evans, D. J. P. o. t. R. S. o. L. A. M.; Sciences, P., The shear properties of Langmuir—Blodgett layers. **1982,** *380* (1779), 389-407.
114. Chandross, M.; Grest, G. S.; Stevens, M. J., Friction between Alkylsilane Monolayers: Molecular Simulation of Ordered Monolayers. *Langmuir* **2002,** *18* (22), 8392-8399.
115. Eyring, H., Viscosity, plasticity, and diffusion as examples of absolute reaction rates. *The Journal of chemical physics* **1936,** *4* (4), 283-291.
116. Zhurkov, S. N. In *Kinetic concept of the strength of solids*, ICF1, Japan 1965, 1965.
117. Prandtl, L. J. Z. J. o. A. M.; Mechanik, M. Z. f. A. M. u., Ein Gedankenmodell zur kinetischen Theorie der festen Körper. **1928,** *8* (2), 85-106.
118. Drummond, C.; Israelachvili, J.; Richetti, P., Friction between two weakly adhering boundary lubricated surfaces in water. *Physical Review E* **2003,** *67* (6), 066110.
119. Kauzmann, W.; Eyring, H., The viscous flow of large molecules. *Journal of the American Chemical Society* **1940,** *62* (11), 3113-3125.

120. Spikes, H.; Tysoe, W., On the Commonality Between Theoretical Models for Fluid and Solid Friction, Wear and Tribochemistry. *Tribology Letters* **2015,** *59* (1), 21.
121. Murphy, K. L.; Tysoe, W. T.; Bennett, D. W., A comparative investigation of aryl isocyanides chemisorbed to palladium and gold: An ATR-IR spectroscopic study. *Langmuir* **2004,** *20* (5), 1732-1738.
122. Murphy, K.; Azad, S.; Bennett, D.; Tysoe, W., Adsorption, decomposition and isomerization of methyl isocyanide and acetonitrile on Pd (111). *Surface science* **2000,** *467* (1), 1-9.
123. Barthel, A. J.; Al-Azizi, A.; Surdyka, N. D.; Kim, S. H., Effects of gas or vapor adsorption on adhesion, friction, and wear of solid interfaces. *Langmuir* **2013,** *30* (11), 2977-2992.
124. Smith, D. K., Opal, cristobalite, and tridymite: noncrystallinity versus crystallinity, nomenclature of the silica minerals and bibliography. *Powder diffraction* **1998,** *13* (1), 2-19.
125. Stachurski, Z. H., On Structure and Properties of Amorphous Materials. *Materials* **2011,** *4* (9), 1564-1598.
126. Yeon, J., *Development of a reaxff reactive force field for silicon/oxygen/hydrogen/fluoride interactions and applications to hydroxylation and friction*. The Pennsylvania State University: 2016.
127. Mozzi, R.; Warren, B., The structure of vitreous silica. *Journal of Applied Crystallography* **1969,** *2* (4), 164-172.
128. Zhuravlev, L., The surface chemistry of amorphous silica. Zhuravlev model. *Colloids and Surfaces A: Physicochemical and Engineering Aspects* **2000,** *173* (1), 1-38.
129. Senftle, T. P.; Hong, S.; Islam, M. M.; Kylasa, S. B.; Zheng, Y.; Shin, Y. K.; Junkermeier, C.; Engel-Herbert, R.; Janik, M. J.; Aktulga, H. M., The ReaxFF reactive force-field: development, applications and future directions. *npj Computational Materials* **2016,** *2*, 15011.
130. Plimpton, S., Fast Parallel Algorithms for Short-Range Molecular Dynamics. *Journal of Computational Physics* **1995,** *117* (1), 1-19.
131. Stukowski, A., Visualization and Analysis of Atomistic Simulation Data with OVITO–the Open Visualization Tool. *Modelling and Simulation in Materials Science and Engineering* **2009,** *18* (1), 015012.
132. Banerjee, J.; Bojan, V.; Pantano, C. G.; Kim, S. H., Effect of heat treatment on the surface chemical structure of glass: Oxygen speciation from in situ XPS analysis. *Journal of the American Ceramic Society* **2018,** *101* (2), 644-656.
133. Khajeh, A.; Chen, Z.; Kim, S. H.; Martini, A., Effect of Ambient Chemistry on Friction at the Basal Plane of Graphite. *ACS Applied Materials & Interfaces* **2019,** *11* (43), 40800-40807.
134. Santner, E.; Czichos, H., Tribology of polymers. *Tribology International* **1989,** *22* (2), 103-109.
135. Gosvami, N.; Bares, J.; Mangolini, F.; Konicek, A.; Yablon, D.; Carpick, R., Mechanisms of antiwear tribofilm growth revealed in situ by single-asperity sliding contacts. *Science* **2015,** *348* (6230), 102-106.
136. Bell, G. I., Models for the specific adhesion of cells to cells. *Science* **1978,** *200* (4342), 618-627.
137. Raina, A.; Anand, A., Tribological investigation of diamond nanoparticles for steel/steel contacts in boundary lubrication regime. *Applied Nanoscience* **2017,** *7* (7), 371-388.
138. Binet, M. L.; Commereuc, S.; Verney, V., Thermo-oxidation of polyterpenes: influence of the physical state. *European Polymer Journal* **2000,** *36* (10), 2133-2142.
139. Koyama, M.; Hayakawa, J.; Onodera, T.; Ito, K.; Tsuboi, H.; Endou, A.; Kubo, M.; Del Carpio, C. A.; Miyamoto, A., Tribochemical Reaction Dynamics of Phosphoric Ester Lubricant Additive by Using a Hybrid Tight-Binding Quantum Chemical Molecular Dynamics Method. *The Journal of Physical Chemistry B* **2006,** *110* (35), 17507-17511.

140. Kokalj, A.; Peljhan, S., Density Functional Theory Study of ATA, BTAH, and BTAOH as Copper Corrosion Inhibitors: Adsorption onto Cu(111) from Gas Phase. *Langmuir* **2010,** *26* (18), 14582-14593.
141. Cuppen, H. M.; Karssemeijer, L. J.; Lamberts, T., The Kinetic Monte Carlo Method as a Way To Solve the Master Equation for Interstellar Grain Chemistry. *Chemical Reviews* **2013,** *113* (12), 8840-8871.
142. Mei, D.; Sheth, P. A.; Neurock, M.; Smith, C. M., First-principles-based kinetic Monte Carlo simulation of the selective hydrogenation of acetylene over Pd(111). *Journal of Catalysis* **2006,** *242* (1), 1-15.
143. Eckert, M.; Neyts, E.; Bogaerts, A., Insights into the Growth of (Ultra)nanocrystalline Diamond by Combined Molecular Dynamics and Monte Carlo Simulations. *Crystal Growth & Design* **2010,** *10* (7), 3005-3021.
144. Yue, D.-C.; Ma, T.-B.; Hu, Y.-Z.; Yeon, J.; van Duin, A. C. T.; Wang, H.; Luo, J., Tribochemistry of Phosphoric Acid Sheared between Quartz Surfaces: A Reactive Molecular Dynamics Study. *The Journal of Physical Chemistry C* **2013,** *117* (48), 25604-25614.
145. Voter, A. F.; Montalenti, F.; Germann, T. C., Extending the Time Scale in Atomistic Simulation of Materials. *Annual Review of Materials Research* **2002,** *32* (1), 321-346.
146. Perez, D.; Uberuaga, B. P.; Voter, A. F., The parallel replica dynamics method – Coming of age. *Computational Materials Science* **2015,** *100*, 90-103.
147. Sangiovanni, D. G.; Mei, A. B.; Hultman, L.; Chirita, V.; Petrov, I.; Greene, J. E., Ab Initio Molecular Dynamics Simulations of Nitrogen/VN(001) Surface Reactions: Vacancy-Catalyzed N2 Dissociative Chemisorption, N Adatom Migration, and N2 Desorption. *The Journal of Physical Chemistry C* **2016,** *120* (23), 12503-12516.
148. Rimsza, J. M.; Du, J., Surface reactions and structural evolution of organosilicate glass under Ar plasma bombardment. *Computational Materials Science* **2015,** *110*, 287-294.
149. Cao, H.; Srivastava, P.; Choi, K.; Kim, S.; Lee, K.-R., Early stage oxynitridation process of Si(001) surface by NO gas: Reactive molecular dynamics simulation study. *Journal of Applied Physics* **2016,** *119* (12), 125305.
150. Valipa, M. S.; Sriraman, S.; Aydil, E. S.; Maroudas, D., Atomic-scale analysis of fundamental mechanisms of surface valley filling during plasma deposition of amorphous silicon thin films. *Surface Science* **2005,** *574* (2), 123-143.
151. Pamungkas, M. A.; Joe, M.; Kim, B.-H.; Lee, K.-R., Reactive molecular dynamics simulation of early stage of dry oxidation of Si (100) surface. *Journal of Applied Physics* **2011,** *110* (5), 053513.
152. Chang, J. G.; Hwang, C. C.; Ju, S. P.; Huang, S. H., A molecular dynamics simulation investigation into the structure of fullerene C60 grown on a diamond substrate. *Carbon* **2004,** *42* (12), 2609-2616.
153. Guan, B.; Pochopien, B. A.; Wright, D. S., The chemistry, mechanism and function of tricresyl phosphate (TCP) as an anti-wear lubricant additive. *Lubrication Science* **2016,** *28* (5), 257-265.
154. Irving, D. L.; Brenner, D. W., Diffusion on a Self-Assembled Monolayer: Molecular Modeling of a Bound + Mobile Lubricant. *The Journal of Physical Chemistry B* **2006,** *110* (31), 15426-15431.
155. Cui, S.; de Almeida, V. F.; Hay, B. P.; Ye, X.; Khomami, B., Molecular Dynamics Simulation of Tri-n-butyl-Phosphate Liquid: A Force Field Comparative Study. *The Journal of Physical Chemistry B* **2012,** *116* (1), 305-313.
156. Khajeh, A.; Hu, X.; Mohammadtabar, K.; Shin, Y. K.; van Duin, A. C. T.; Berkebile, S.; Martini, A., Statistical Analysis of Tri-Cresyl Phosphate Conversion on an Iron Oxide Surface

Using Reactive Molecular Dynamics Simulations. *The Journal of Physical Chemistry C* **2019,** *123* (20), 12886-12893.
157. Johnson, D. W.; Morrow, S.; Forster, N. H.; Saba, C. S., Vapor-Phase Lubrication: Reaction of Phosphate Ester Vapors with Iron and Steel. *Chemistry of Materials* **2002,** *14* (9), 3767-3775.
158. Johnson, D.; Hils, J., Phosphate Esters, Thiophosphate Esters and Metal Thiophosphates as Lubricant Additives. *Lubricants* **2013,** *1* (4), 132-148.
159. Saba, C. S.; Forster, N. H., Reactions of Aromatic Phosphate Esters with Metals and Their Oxides. *Tribology Letters* **2002,** *12* (2), 135-146.
160. Pavelko, G. F., The mechanism of iron phosphide formation during boundary friction in the presence of organic phosphates and phosphites. *Journal of Friction and Wear* **2012,** *33* (2), 115-123.
161. Khajeh, A.; Krim, J.; Martini, A., Synergistic effect of nanodiamonds on the adsorption of tricresyl phosphate on iron oxide surfaces. *Applied Physics Letters* **2019,** *114* (17), 171602.
162. Lloyd, A. L.; Zhou, Y.; Yu, M.; Scott, C.; Smith, R.; Kenny, S. D., Reaction pathways in atomistic models of thin film growth. *The Journal of Chemical Physics* **2017,** *147* (15), 152719.
163. Mohammadtabar, K.; Eder, S. J.; Bedolla, P. O.; Dörr, N.; Martini, A., Reactive Molecular Dynamics Simulations of Thermal Film Growth from Di-tert-butyl Disulfide on an Fe(100) surface. *Langmuir* **2018,** *34* (51), 15681-15688.
164. Michaelis, S. J. J. B. P. C., Contaminated aircraft cabin air. **2011,** *11*, 132-145.
165. Ramsden, J., *On the proportion of ortho isomers in the tricresyl phosphates contained in jet oil*. 2013; Vol. 13, p 69-72.
166. Dai, W.; Kheireddin, B.; Gao, H.; Liang, H., Roles of nanoparticles in oil lubrication. *Tribology International* **2016,** *102*, 88-98.
167. Ivanov, M.; Shenderova, O., Nanodiamond-based nanolubricants for motor oils. *Current Opinion in Solid State and Materials Science* **2017,** *21* (1), 17-24.
168. Ali, I.; Basheer, A. A.; Kucherova, A.; Memetov, N.; Pasko, T.; Ovchinnikov, K.; Pershin, V.; Kuznetsov, D.; Galunin, E.; Grachev, V.; Tkachev, A., Advances in carbon nanomaterials as lubricants modifiers. *Journal of Molecular Liquids* **2019,** *279*, 251-266.
169. Nunn, N.; Mahbooba, Z.; Ivanov, M. G.; Ivanov, D. M.; Brenner, D. W.; Shenderova, O., Tribological properties of polyalphaolefin oil modified with nanocarbon additives. *Diamond and Related Materials* **2015,** *54*, 97-102.
170. Shirani, A.; Nunn, N.; Shenderova, O.; Osawa, E.; Berman, D., Nanodiamonds for improving lubrication of titanium surfaces in simulated body fluid. *Carbon* **2019,** *143*, 890-896.
171. Jiao, Y.; Liu, S.; Sun, Y.; Yue, W.; Zhang, H., Bioinspired Surface Functionalization of Nanodiamonds for Enhanced Lubrication. *Langmuir* **2018,** *34* (41), 12436-12444.
172. Tong, Y.; Liu, R.; Zhang, T., The effect of a detonation nanodiamond coating on the thermal decomposition properties of RDX explosives. *Physical Chemistry Chemical Physics* **2014,** *16* (33), 17648-17657.
173. Acharya, B.; Sidheswaran, M. A.; Yungk, R.; Krim, J., Quartz crystal microbalance apparatus for study of viscous liquids at high temperatures. *Review of Scientific Instruments* **2017,** *88* (2), 025112.
174. Acharya, B.; Pardue, T. N.; Avva, K. S.; Krim, J., In situ, real time studies of thermal reaction film formation temperatures for iron and 304SS surfaces immersed in 5% tricresyl phosphate in base oil. *Tribology International* **2018,** *126*, 106-115.
175. Acharya, B.; Avva, K. S.; Thapa, B.; Pardue, T. N.; Krim, J., Synergistic Effect of Nanodiamond and Phosphate Ester Anti-Wear Additive Blends. **2018,** *6* (2), 56.
176. Hsu, J.-P., *Interfacial Forces and Fields: Theory and Applications*. CRC Press: 1999; Vol. 85.

177. Kern, G.; Hafner, J., Ab initio calculations of the atomic and electronic structure of clean and hydrogenated diamond (110) surfaces. *Physical Review B* **1997,** *56* (7), 4203-4210.
178. Ho, D., *Nanodiamonds: applications in biology and nanoscale medicine*. Springer Science & Business Media: 2009.
179. Krueger, A.; Williams, O. J. R. n.; nanotechnology, The chemistry of nanodiamond. **2014,** *2014*, 49-88.
180. Amontons, G. J. J.-J. S. O. T., De la Resistance Cause'e dans les Machines (1). **1999,** *44*, 229-235.
181. Bhushan, B.; Israelachvili, J. N.; Landman, U., Nanotribology: friction, wear and lubrication at the atomic scale. *Nature* **1995,** *374* (6523), 607-616.
182. Thompson, P. A.; Robbins, M. O., Origin of Stick-Slip Motion in Boundary Lubrication. *Science* **1990,** *250* (4982), 792.
183. Noy, A.; Frisbie, C. D.; Rozsnyai, L. F.; Wrighton, M. S.; Lieber, C. M. J. J. o. t. A. C. S., Chemical force microscopy: exploiting chemically-modified tips to quantify adhesion, friction, and functional group distributions in molecular assemblies. **1995,** *117* (30), 7943-7951.
184. Tian, K.; Gosvami, N. N.; Goldsby, D. L.; Liu, Y.; Szlufarska, I.; Carpick, R. W. J. P. r. l., Load and time dependence of interfacial chemical bond-induced friction at the nanoscale. **2017,** *118* (7), 076103.
185. Yeon, J.; van Duin, A. C. T., ReaxFF Molecular Dynamics Simulations of Hydroxylation Kinetics for Amorphous and Nano-Silica Structure, and Its Relations with Atomic Strain Energy. *The Journal of Physical Chemistry C* **2016,** *120* (1), 305-317.
186. Jia, X.; Hofmann, M.; Meunier, V.; Sumpter, B. G.; Campos-Delgado, J.; Romo-Herrera, J. M.; Son, H.; Hsieh, Y.-P.; Reina, A.; Kong, J. J. S., Controlled formation of sharp zigzag and armchair edges in graphitic nanoribbons. **2009,** *323* (5922), 1701-1705.
187. Levita, G.; Restuccia, P.; Righi, M. C. J. C., Graphene and MoS2 interacting with water: A comparison by ab initio calculations. **2016,** *107*, 878-884.
188. Jacobs, T. D. B.; Martini, A., Measuring and Understanding Contact Area at the Nanoscale: A Review. *Applied Mechanics Reviews* **2017,** *69* (6).
189. Falk, M. L.; Langer, J. S., Dynamics of viscoplastic deformation in amorphous solids. *Physical Review E* **1998,** *57* (6), 7192-7205.
190. Shimizu, F.; Ogata, S.; Li, J., Theory of Shear Banding in Metallic Glasses and Molecular Dynamics Calculations. *MATERIALS TRANSACTIONS* **2007,** *48* (11), 2923-2927.
191. Guardia, E.; Martí, J.; García-Tarrés, L.; Laria, D. J. J. o. M. L., A molecular dynamics simulation study of hydrogen bonding in aqueous ionic solutions. **2005,** *117* (1-3), 63-67.
192. Geim, A. K., Graphene: Status and Prospects. *Science* **2009,** *324* (5934), 1530.
193. Bunch, J. S.; van der Zande, A. M.; Verbridge, S. S.; Frank, I. W.; Tanenbaum, D. M.; Parpia, J. M.; Craighead, H. G.; McEuen, P. L., Electromechanical Resonators from Graphene Sheets. *Science* **2007,** *315* (5811), 490.
194. Ferrari, A. C.; Meyer, J. C.; Scardaci, V.; Casiraghi, C.; Lazzeri, M.; Mauri, F.; Piscanec, S.; Jiang, D.; Novoselov, K. S.; Roth, S.; Geim, A. K., Raman Spectrum of Graphene and Graphene Layers. *Physical Review Letters* **2006,** *97* (18), 187401.
195. Gupta, A.; Chen, G.; Joshi, P.; Tadigadapa, S.; Eklund, Raman Scattering from High-Frequency Phonons in Supported n-Graphene Layer Films. *Nano Letters* **2006,** *6* (12), 2667-2673.
196. Sazonova, V.; Yaish, Y.; Üstünel, H.; Roundy, D.; Arias, T. A.; McEuen, P. L., A tunable carbon nanotube electromechanical oscillator. *Nature* **2004,** *431* (7006), 284-287.
197. Qian, Dong; Wagner; , G. J.; Liu , W. K.; Yu , M.-F.; Ruoff , R. S., Mechanics of carbon nanotubes. *Applied Mechanics Reviews* **2002,** *55* (6), 495-533.
198. Sekaric, L.; Parpia, J. M.; Craighead, H. G.; Feygelson, T.; Houston, B. H.; Butler, J. E., Nanomechanical resonant structures in nanocrystalline diamond. **2002,** *81* (23), 4455-4457.

199. Li, X.; Ono, T.; Wang, Y.; Esashi, M., Ultrathin single-crystalline-silicon cantilever resonators: Fabrication technology and significant specimen size effect on Young's modulus. **2003,** *83* (15), 3081-3083.
200. Chen, Z.; Khajeh, A.; Martini, A.; Kim, S. H., Chemical and Physical Origins of Friction on Surfaces with Atomic Steps. *Sci Adv* **2019,** *5* (8), eaaw0513.
201. Li, H.; Wang, J.; Gao, S.; Chen, Q.; Peng, L.; Liu, K.; Wei, X., Superlubricity between MoS2 Monolayers. *Advanced Materials* **2017,** *29* (27), 1701474.
202. Song, Y.; Mandelli, D.; Hod, O.; Urbakh, M.; Ma, M.; Zheng, Q., Robust microscale superlubricity in graphite/hexagonal boron nitride layered heterojunctions. *Nature Materials* **2018,** *17* (10), 894-899.
203. Deng, Z.; Smolyanitsky, A.; Li, Q.; Feng, X.-Q.; Cannara, R. J., Adhesion-dependent negative friction coefficient on chemically modified graphite at the nanoscale. *Nature Materials* **2012,** *11* (12), 1032-1037.
204. Hirano, M.; Shinjo, K.; Kaneko, R.; Murata, Y., Observation of Superlubricity by Scanning Tunneling Microscopy. *Physical Review Letters* **1997,** *78* (8), 1448-1451.
205. Lee, C.; Li, Q.; Kalb, W.; Liu, X.-Z.; Berger, H.; Carpick, R. W.; Hone, J., Frictional Characteristics of Atomically Thin Sheets. *Science* **2010,** *328* (5974), 76.
206. Lee, H.; Lee, H.-B.-R.; Kwon, S.; Salmeron, M.; Park, J. Y., Internal and External Atomic Steps in Graphite Exhibit Dramatically Different Physical and Chemical Properties. *ACS Nano* **2015,** *9* (4), 3814-3819.
207. Blake, P.; Brimicombe, P. D.; Nair, R. R.; Booth, T. J.; Jiang, D.; Schedin, F.; Ponomarenko, L. A.; Morozov, S. V.; Gleeson, H. F.; Hill, E. W.; Geim, A. K.; Novoselov, K. S., Graphene-Based Liquid Crystal Device. *Nano Letters* **2008,** *8* (6), 1704-1708.
208. Derjaguin, B. V.; Muller, V. M.; Toporov, Y. P., Effect of contact deformations on the adhesion of particles. *Journal of Colloid and Interface Science* **1975,** *53* (2), 314-326.
209. Chen, Z.; Khajeh, A.; Martini, A.; Kim, S. H., Identifying Physical and Chemical Contributions to Friction: A Comparative Study of Chemically Inert and Active Graphene Step Edges. *ACS Applied Materials & Interfaces* **2020,** *12* (26), 30007-30015.
210. Sader, J. E.; Larson, I.; Mulvaney, P.; White, L. R., Method for the Calibration of Atomic Force Microscope Cantilevers. *Review of Scientific Instruments* **1995,** *66* (7), 3789-3798.
211. Barnette, A. L.; Ohlhausen, J. A.; Dugger, M. T.; Kim, S. H., Humidity Effects on In Situ Vapor Phase Lubrication with n-Pentanol. *Tribology Letters* **2014,** *55* (1), 177-186.
212. Asay, D. B.; Kim, S. H., Evolution of the Adsorbed Water Layer Structure on Silicon Oxide at Room Temperature. *The Journal of Physical Chemistry B* **2005,** *109* (35), 16760-16763.
213. Díez-Pérez, I.; Luna, M.; Teherán, F.; Ogletree, D. F.; Sanz, F.; Salmeron, M., Interaction of Water with Self-Assembled Monolayers of Alkylsilanes on Mica. *Langmuir* **2004,** *20* (4), 1284-1290.
214. Chipara, A. C.; Tsafack, T.; Owuor, P. S.; Yeon, J.; Junkermeier, C. E.; van Duin, A. C. T.; Bhowmick, S.; Asif, S. A. S.; Radhakrishnan, S.; Park, J. H.; Brunetto, G.; Kaipparettu, B. A.; Galvão, D. S.; Chipara, M.; Lou, J.; Tsang, H. H.; Dubey, M.; Vajtai, R.; Tiwary, C. S.; Ajayan, P. M., Underwater Adhesive Using Solid–Liquid Polymer Mixes. *Materials Today Chemistry* **2018,** *9*, 149-157.
215. Goverapet Srinivasan, S.; van Duin, A. C. T., Molecular-Dynamics-Based Study of the Collisions of Hyperthermal Atomic Oxygen with Graphene Using the ReaxFF Reactive Force Field. *The Journal of Physical Chemistry A* **2011,** *115* (46), 13269-13280.
216. Chenoweth, K.; van Duin, A. C. T.; Goddard, W. A., ReaxFF Reactive Force Field for Molecular Dynamics Simulations of Hydrocarbon Oxidation. *The Journal of Physical Chemistry A* **2008,** *112* (5), 1040-1053.

217. Chenoweth, K.; Cheung, S.; van Duin, A. C. T.; Goddard, W. A.; Kober, E. M., Simulations on the Thermal Decomposition of a Poly(dimethylsiloxane) Polymer Using the ReaxFF Reactive Force Field. *Journal of the American Chemical Society* **2005,** *127* (19), 7192-7202.
218. Rietsch, J.-C.; Brender, P.; Dentzer, J.; Gadiou, R.; Vidal, L.; Vix-Guterl, C., Evidence of water chemisorption during graphite friction under moist conditions. *Carbon* **2013,** *55*, 90-97.
219. Alazizi, A.; Barthel, A. J.; Surdyka, N. D.; Luo, J.; Kim, S. H., Vapors in the ambient—A complication in tribological studies or an engineering solution of tribological problems? *Friction* **2015,** *3* (2), 85-114.
220. Asay, D. B.; Dugger, M. T.; Ohlhausen, J. A.; Kim, S. H., Macro- to Nanoscale Wear Prevention via Molecular Adsorption. *Langmuir* **2008,** *24* (1), 155-159.
221. Chen, Z.; Kim, S. H., Measuring nanoscale friction at graphene step edges. *Friction* **2020,** *8* (4), 802-811.
222. Chen, L.; Chen, Z.; Tang, X.; Yan, W.; Zhou, Z.; Qian, L.; Kim, S. H., Friction at Single-Layer Graphene Step Edges Due to Chemical and Topographic Interactions. *Carbon* **2019,** *154*, 67-73.
223. Zhang, J.; Ewen, J. P.; Ueda, M.; Wong, J. S. S.; Spikes, H. A., Mechanochemistry of Zinc Dialkyldithiophosphate on Steel Surfaces under Elastohydrodynamic Lubrication Conditions. *ACS Applied Materials & Interfaces* **2020,** *12* (5), 6662-6676.
224. Garvey, M.; Weinert, M.; Tysoe, W. T., On the Pressure Dependence of Shear Strengths in Sliding, Boundary-Layer Friction. *Tribology Letters* **2011,** *44* (1), 67.
225. Erdemir, A., Genesis of superlow friction and wear in diamondlike carbon films. *Tribology International* **2004,** *37* (11), 1005-1012.
226. Eryilmaz, O. L.; Erdemir, A., Surface analytical investigation of nearly-frictionless carbon films after tests in dry and humid nitrogen. *Surface and Coatings Technology* **2007,** *201* (16), 7401-7407.
227. Eryilmaz, O. L.; Erdemir, A., TOF-SIMS and XPS characterization of diamond-like carbon films after tests in inert and oxidizing environments. *Wear* **2008,** *265* (1), 244-254.
228. Marino, M. J.; Hsiao, E.; Chen, Y.; Eryilmaz, O. L.; Erdemir, A.; Kim, S. H., Understanding Run-In Behavior of Diamond-Like Carbon Friction and Preventing Diamond-Like Carbon Wear in Humid Air. *Langmuir* **2011,** *27* (20), 12702-12708.
229. Al-Azizi, A. A.; Eryilmaz, O.; Erdemir, A.; Kim, S. H., Surface Structure of Hydrogenated Diamond-like Carbon: Origin of Run-In Behavior Prior to Superlubricious Interfacial Shear. *Langmuir* **2015,** *31* (5), 1711-1721.
230. Manimunda, P.; Al-Azizi, A.; Kim, S. H.; Chromik, R. R., Shear-Induced Structural Changes and Origin of Ultralow Friction of Hydrogenated Diamond-like Carbon (DLC) in Dry Environment. *ACS Applied Materials & Interfaces* **2017,** *9* (19), 16704-16714.
231. Wang, D.-S.; Chang, S.-Y.; Huang, Y.-C.; Wu, J.-B.; Lai, H.-J.; Leu, M.-S., Nanoscopic observations of stress-induced formation of graphitic nanocrystallites at amorphous carbon surfaces. *Carbon* **2014,** *74*, 302-311.
232. Chen, X.; Zhang, C.; Kato, T.; Yang, X.-a.; Wu, S.; Wang, R.; Nosaka, M.; Luo, J., Evolution of tribo-induced interfacial nanostructures governing superlubricity in a-C:H and a-C:H:Si films. *Nature Communications* **2017,** *8* (1), 1675.
233. Chen, Z.; He, X.; Xiao, C.; Kim, H. S., Effect of Humidity on Friction and Wear—A Critical Review. *Lubricants* **2018,** *6* (3).
234. Bryant, P. J.; Gutshall, P. L.; Taylor, L. H., A Study of Mechanisms of Graphite Friction and Wear. *Wear* **1964,** *7* (1), 118-126.
235. Buckley, D. H., Friction,Wear, and Lubrication in Vacuum. **1971**.

236. Gao, X.; Chen, L.; Ji, L.; Liu, X.; Li, H.; Zhou, H.; Chen, J., Humidity-Sensitive Macroscopic Lubrication Behavior of an as-Sprayed Graphene Oxide Coating. *Carbon* **2018,** *140*, 124-130.
237. Hasz, K.; Ye, Z.; Martini, A.; Carpick, R. W., Experiments and Simulations of the Humidity Dependence of Friction Between Nanoasperities and Graphite: The Role of Interfacial Contact Quality. *Physical Review Materials* **2018,** *2* (12), 126001.
238. Ye, Z.; Egberts, P.; Han, G. H.; Johnson, A. T. C.; Carpick, R. W.; Martini, A., Load-Dependent Friction Hysteresis on Graphene. *ACS Nano* **2016,** *10* (5), 5161-5168.
239. Egberts, P.; Ye, Z.; Liu, X. Z.; Dong, Y.; Martini, A.; Carpick, R. W., Environmental Dependence of Atomic-Scale Friction at Graphite Surface Steps. *J Physical Review B* **2013,** *88* (3), 035409.
240. Jradi, K.; Schmitt, M.; Bistac, S., Influence of the Surface Chemistry on the Nanotribological Behaviour of (AFM tip/graphite) Couples. *Applied Surface Science* **2012,** *258* (10), 4687-4697.
241. Stempflé, P.; Castelein, G.; Brendlé, M., Influence of Environment on the Size of the Elemental Wear Debris of Graphite. In *Boundary and Mixed Lubrication - Science and Applications, Proceedings of the 28th Leeds-Lyon Symposium on Tribology*, Dowson, D.; Priest, M.; Dalmaz, G.; Lubrecht, A. A., Eds. Elsevier: 2002; Vol. 40, pp 295-304.
242. Stempflé, P.; von Stebut, J., Nano-Mechanical Behaviour of the 3rd Body Generated in Dry Friction—Feedback Effect of the 3rd Body and Influence of the Surrounding Environment on the Tribology of Graphite. *Wear* **2006,** *260* (6), 601-614.
243. Cabrera-Sanfelix, P.; Darling, G. R., Dissociative Adsorption of Water at Vacancy Defects in Graphite. *The Journal of Physical Chemistry C* **2007,** *111* (49), 18258-18263.
244. Allouche, A.; Ferro, Y., Dissociative Adsorption of Small Molecules at Vacancies on the Graphite (0001) Surface. *Carbon* **2006,** *44* (15), 3320-3327.
245. Nevshupa, R. A.; Scherge, M.; Ahmed, S. I. U., Transitional Microfriction Behavior of Silicon Induced by Spontaneous Water Adsorption. *Surface Science* **2002,** *517* (1), 17-28.
246. Vengudusamy, B.; Mufti, R. A.; Lamb, G. D.; Green, J. H.; Spikes, H. A., Friction Properties of DLC/DLC Contacts in Base Oil. *Tribology International* **2011,** *44* (7), 922-932.
247. Kirkhorn, L.; Gutnichenko, O.; Bihagen, S.; Ståhl, J.-E., Minimum Quantity Lubrication (MQL) with Carbon Nanostructured Additives in Sheet Metal Forming. *Procedia Manufacturing* **2018,** *25*, 375-381.
248. Huang, H. D.; Tu, J. P.; Gan, L. P.; Li, C. Z., An Investigation on Tribological Properties of Graphite Nanosheets as Oil Additive. *Wear* **2006,** *261* (2), 140-144.
249. Zhang, Z.-c.; Cai, Z.-b.; Peng, J.-f.; Zhu, M.-h., Comparison of the Tribology Performance of Nano-Diesel Soot and Graphite Particles as Lubricant Additives. *Journal of Physics D: Applied Physics* **2015,** *49* (4), 045304.
250. Lancaster, J. K.; Pritchard, J. R., The Influence of Environment and Pressure on the Transition to Dusting Wear of Graphite. *Journal of Physics D: Applied Physics* **1981,** *14* (4), 747-762.
251. Buldum, A.; Lu, J. P., Atomic Scale Sliding and Rolling of Carbon Nanotubes. *Physical Review Letters* **1999,** *83* (24), 5050-5053.
252. Calvo-Almazán, I.; Bahn, E.; Koza, M. M.; Zbiri, M.; Maccarini, M.; Telling, M. T. F.; Miret-Artés, S.; Fouquet, P., Benzene Diffusion on Graphite Described by a Rough Hard Disk Model. *Carbon* **2014,** *79*, 183-191.
253. Calvo-Almazán, I.; Sacchi, M.; Tamtögl, A.; Bahn, E.; Koza, M. M.; Miret-Artés, S.; Fouquet, P., Ballistic Diffusion in Polyaromatic Hydrocarbons on Graphite. *The Journal of Physical Chemistry Letters* **2016,** *7* (24), 5285-5290.

254. Kong, X.; Thomson, E. S.; Marković, N.; Pettersson, J. B. C., Dynamics and Kinetics of Methanol-Graphite Interactions at Low Surface Coverage. *ChemPhysChem* **2019,** *0* (0).
255. Fouquet, P.; Johnson, M. R.; Hedgeland, H.; Jardine, A. P.; Ellis, J.; Allison, W., Molecular Dynamics Simulations of the Diffusion of Benzene Sub-Monolayer Films on Graphite Basal Plane Surfaces. *Carbon* **2009,** *47* (11), 2627-2639.
256. de Wijn, A. S., Internal Degrees of Freedom and Transport of Benzene on Graphite. *Physical Review E* **2011,** *84* (1), 011610.
257. Jafary-Zadeh, M.; Reddy, C. D.; Zhang, Y.-W., Effect of Rotational Degrees of Freedom on Molecular Mobility. *The Journal of Physical Chemistry C* **2013,** *117* (13), 6800-6806.
258. Barnette, A. L.; Asay, D. B.; Janik, M. J.; Kim, S. H., Adsorption Isotherm and Orientation of Alcohols on Hydrophilic SiO2 under Ambient Conditions. *The Journal of Physical Chemistry C* **2009,** *113* (24), 10632-10641.
259. Barthel, A. J.; Luo, J.; Hwang, K. S.; Lee, J.-Y.; Kim, S. H., Boundary Lubrication Effect of Organic Residue Left on Surface After Evaporation of Organic Cleaning Solvent. *Wear* **2016,** *350-351*, 21-26.
260. Senftle, T. P.; Hong, S.; Islam, M. M.; Kylasa, S. B.; Zheng, Y. X.; Shin, Y. K.; Junkermeier, C.; Engel-Herbert, R.; Janik, M. J.; Aktulga, H. M.; Verstraelen, T.; Grama, A.; van Duin, A. C. T., The ReaxFF Reactive Force-Field: Development, Applications and Future Directions. *Npj Comput Mater* **2016,** *2*, 15011.
261. Bauschlicher, C. W.; Qi, T.; Reed, E. J.; Lenfant, A.; Lawson, J. W.; Desai, T. G., Comparison of ReaxFF, DFTB, and DFT for Phenolic Pyrolysis. 2. Elementary Reaction Paths. *The Journal of Physical Chemistry A* **2013,** *117* (44), 11126-11135.
262. Qi, T.; Bauschlicher, C. W.; Lawson, J. W.; Desai, T. G.; Reed, E. J., Comparison of ReaxFF, DFTB, and DFT for Phenolic Pyrolysis. 1. Molecular Dynamics Simulations. *The Journal of Physical Chemistry A* **2013,** *117* (44), 11115-11125.
263. Qi, T.; Bauschlicher, C. W.; Lawson, J. W.; Desai, T. G.; Reed, E. J.; Lenfant, A., Addendum to "Comparison of ReaxFF, DFTB, and DFT for Phenolic Pyrolysis. 1. Molecular Dynamics Simulations" and "Comparison of ReaxFF, DFTB, and DFT for Phenolic Pyrolysis. 2. Elementary Reaction Paths". *The Journal of Physical Chemistry A* **2014,** *118* (28), 5355-5357.
264. Ghahghaei Nezam Abadee, Z.; Hekmati, M.; Ganji, M. D., Removing Phenol Contaminants from Wastewater Using Graphene Nanobuds: DFT and Reactive MD Simulation Investigations. *Journal of Molecular Liquids* **2019,** *286*, 110872.
265. Moradi, F.; Ganji, M. D.; Sarrafi, Y., Tunable Phenol Remediation from Wastewater Using SWCNT-Based, Sub-Nanometer Porous Membranes: Reactive Molecular Dynamics Simulations and DFT Calculations. *Physical Chemistry Chemical Physics* **2017,** *19* (12), 8388-8399.
266. O'Connor, T. C.; Andzelm, J.; Robbins, M. O., AIREBO-M: A Reactive Model for Hydrocarbons at Extreme Pressures. *The Journal of Chemical Physics* **2015,** *142* (2), 024903.
267. Barnette, A. L.; Asay, D. B.; Kim, D.; Guyer, B. D.; Lim, H.; Janik, M. J.; Kim, S. H., Experimental and Density Functional Theory Study of the Tribochemical Wear Behavior of SiO2 in Humid and Alcohol Vapor Environments. *Langmuir* **2009,** *25* (22), 13052-13061.
268. Yaniv, R.; Koren, E., Robust Superlubricity of Gold–Graphite Heterointerfaces. *Advanced Functional Materials* **2019,** *0* (0), 1901138.
269. Li, Q.; Dong, Y.; Perez, D.; Martini, A.; Carpick, R. W., Speed Dependence of Atomic Stick-Slip Friction in Optimally Matched Experiments and Molecular Dynamics Simulations. *Physical Review Letters* **2011,** *106* (12), 126101.
270. Liu, X.-Z.; Ye, Z.; Dong, Y.; Egberts, P.; Carpick, R. W.; Martini, A., Dynamics of Atomic Stick-Slip Friction Examined with Atomic Force Microscopy and Atomistic Simulations at Overlapping Speeds. *Physical Review Letters* **2015,** *114* (14), 146102.

271. Zaïdi, H.; Paulmier, D.; Lepage, J., The Influence of the Environment on the Friction and Wear of Graphitic Carbons: II. Gas Coverage of Wear Debris. *Applied Surface Science* **1990,** *44* (3), 221-233.
272. Zaidi, H.; Robert, F.; Paulmier, D., Influence of adsorbed gases on the surface energy of graphite: consequences on the friction behaviour. *Thin Solid Films* **1995,** *264* (1), 46-51.
273. Gao, G.; Mikulski, P. T.; Harrison, J. A., Molecular-Scale Tribology of Amorphous Carbon Coatings: Effects of Film Thickness, Adhesion, and Long-Range Interactions. *J Journal of the American Chemical Society* **2002,** *124* (24), 7202-7209.
274. Marom, N.; Bernstein, J.; Garel, J.; Tkatchenko, A.; Joselevich, E.; Kronik, L.; Hod, O., Stacking and Registry Effects in Layered Materials: the Case of Hexagonal Boron Nitride. *J Physical review letters* **2010,** *105* (4), 046801.
275. Hod, O., The Registry Index: a Quantitative Measure of Materials' Interfacial Commensurability. *Chemphyschem* **2013,** *14* (11), 2376-91.
276. Muraki, M., Molecular Structure of Synthetic Hydrocarbon Oils and Their Rheological Properties Governing Traction Characteristics. *Tribology International* **1987,** *20* (6), 347-354.
277. Toshiyuki, T.; Hitoshi, H., The Fundamental Molecular Structures of Synthetic Traction Fluids. *Tribology International* **1994,** *27* (3), 183-187.
278. Tsubouchi, T.; Hata, H., Study on the Fundamental Molecular Structures of Synthetic Traction Fluids: Part 2. *Tribology International* **1995,** *28* (5), 335-340.
279. Tamura, H.; Yoshida, M.; Kusakabe, K.; Chung; Miura, R.; Kubo, M.; Teraishi, K.; Chatterjee, A.; Miyamoto, A., Molecular Dynamics Simulation of Friction of Hydrocarbon Thin Films. *Langmuir* **1999,** *15* (22), 7816-7821.
280. Ewen, J. P.; Gattinoni, C.; Zhang, J.; Heyes, D. M.; Spikes, H. A.; Dini, D., On the Effect of Confined Fluid Molecular Structure on Nonequilibrium Phase Behaviour and Friction. *Physical Chemistry Chemical Physics* **2017,** *19* (27), 17883-17894.
281. Molinari, R.; Poerio, T.; Argurio, P., One-Step Production of Phenol by Selective Oxidation of Benzene in a Biphasic System. *Catalysis Today* **2006,** *118* (1), 52-56.
282. Tomás-Pejó, E.; Alvira, P.; Ballesteros, M.; Negro, M. J., Chapter 7 - Pretreatment Technologies for Lignocellulose-to-Bioethanol Conversion. In *Biofuels*, Pandey, A.; Larroche, C.; Ricke, S. C.; Dussap, C.-G.; Gnansounou, E., Eds. Academic Press: Amsterdam, 2011; pp 149-176.
283. Levitas, V. I.; Nesterenko, V. F.; Meyers, M. A., Strain-Induced Structural Changes and Chemical Reactions—I. Thermomechanical and Kinetic Models. *Acta Materialia* **1998,** *46* (16), 5929-5945.
284. Barthel, A. J.; Combs, D. R.; Kim, S. H., Synthesis of Polymeric Lubricating Films Directly at the Sliding Interface via Mechanochemical Reactions of Allyl Alcohols Adsorbed from the Vapor Phase. *RSC Advances* **2014,** *4* (50), 26081-26086.
285. Salinas Ruiz, V. R.; Kuwahara, T.; Galipaud, J.; Masenelli-Varlot, K.; Hassine, M. B.; Héau, C.; Stoll, M.; Mayrhofer, L.; Moras, G.; Martin, J. M.; Moseler, M.; de Barros Bouchet, M.-I., Interplay of mechanics and chemistry governs wear of diamond-like carbon coatings interacting with ZDDP-additivated lubricants. *Nature Communications* **2021,** *12* (1), 4550.
286. Ta, H. T. T.; Tran, N. V.; Tieu, A. K.; Zhu, H.; Yu, H.; Ta, T. D., Computational Tribochemistry: A Review from Classical and Quantum Mechanics Studies. *The Journal of Physical Chemistry C* **2021,** *125* (31), 16875-16891.